FLUID-LOADED VIBRATION OF THIN STRUCTURES DUE TO TURBULENT EXCITATION

A Dissertation

Submitted to the Graduate School
of the University of Notre Dame
in Partial Fulfillment of the Requirements
for the Degree of

Doctor of Philosophy

by

Jason Robert Tomko

Scott C. Morris, Director

Graduate Program in Aerospace and Mechanical Engineering

Notre Dame, Indiana

April 2014

UMI Number: 3583070

UMI 3583070

Published by ProQuest LLC (2014). Copyright in the Dissertation held by the Author.

ProQuest LLC.
789 East Eisenhower Parkway
P.O. Box 1346
Ann Arbor, MI 48106 - 1346

FLUID-LOADED VIBRATION OF THIN STRUCTURES DUE TO TURBULENT EXCITATION

Abstract

by

Jason Robert Tomko

Flow-induced structural acoustics involves the study of the vibration of a structure induced by a fluid flow as well as the resulting sound generated and radiated by the motion of the system. The thesis examines several aspects of flow-induced structural vibration for fluid-loaded systems. A new method, termed Magnitude-Phase Identification, is derived to experimentally obtain a modal decomposition of the vibration of a structure using two-point measurements. MPI was used to measure the auto-spectral density of various modes for a non-fluid-loaded, rectangular, clamped plate excited by a spatially-homogeneous turbulent boundary layer. These results agreed well with theory. Using MPI, it was shown that when both fluid-loading and a spatially non-homogeneous wall pressure field is applied to a structure that the mode shapes become dependent on the forcing field, an effect which does not occur when either characteristic is applied individually. Furthermore, the resulting mode shapes are potentially highly asymmetric. It was shown through a discretized string model that these results can be attributed to the

increased damping induced by fluid loading. Internal acoustic wall pressure fields due to a ducted rotor were measured, and it was shown that the acoustic effects of the rotor can be approximated by replacing the rotor with a continuous ring of dipoles located at the blade tip. The finite length of the duct was accounted for through use of a method of images. The theoretical results from this model match well with the measured values. Lastly, the vibration of a fluid-loaded duct excited by an internal rotor is measured through use of MPI. The resulting vibration field appears similar to the field examined earlier due to fluid loading, with a decrease in the coherent vibration magnitude for increasing spatial separation from the reference location.

CONTENTS

FIGURES

TABLES

SYMBOLS

A_f	Magnitude of the normalized streamwise cross-spectral density
A_p	Surface area of structure
a	Duct radius
a_n	Constant coefficient for vibration of mode n
B_f	Magnitude of the normalized spanwise cross-spectral density
B_1	Streamwise separable component for Corcos prediction of cross-spectral density of wall pressure
B_2	Spanwise separable component for Corcos prediction of cross-spectral density of wall pressure
c	Structural wave speed
c_0	Acoustic wave speed in fluid medium
C_d	Viscous damping
c_0	Speed of sound in the fluid medium
D_s	Flexural stiffness
E	Modulus of elasticity
$F(r_0)$	Unsteady dipole force
f	Frequency (Hz)
$f_{cut\text{-}on}$	Duct acoustic cut-on frequency

$G^*_{pp,m}(f)$	Non-dimensional auto-spectral density of dipole force
$g(\vec{r},\vec{r_0})$	Duct acoustics Green's function
$g_n(t)$	Time-dependent coefficient function for vibration of mode n
h	Structural thickness
J_m	Bessel function of the first kind
k	Wave number, defined as 2π divided by wavelength or separation distance, pending the context
k_c	Convective wave number, defined as ω/U_c
k_x	Wave number in streamwise direction
k_y	Wave number in spanwise direction
L	Streamwise structure length
$L(\xi)$	Linear operator representing the restorative force of the structure
$\boldsymbol{M}_{b\text{x}1}$	Vector of magnitude of vibration for each mode at a single frequency
m	Integer representing mode of vibration. For rectangular structures this corresponds to a streamwise component, for ducts this corresponds to a circumferential component.
m_L	Mass per unit length
m_{mn}	Accession (i.e. added mass) due to fluid loading for structural vibration mode $<m,n>$
m_S	Mass per unit area

n	Integer representing mode of vibration. For rectangular structures this corresponds to a spanwise component, for ducts this corresponds to a radial component.
$\hat{n}$	Unit vector in direction of dipole force
P_{ab}	Pressure cross-spectral density between points *a* and *b*
$P_n(t)$	Projection of wall pressure onto mode *n*
$p(\mathbf{y},t)$	Fluctuating component of surface pressure (for 2-dimensional structure) or force per unit length (for 1-dimensional structure)
$p_a(\mathbf{y},t)$	Radiated acoustic pressure due to structural vibration
$p_{a,mn}(y_2,t)$	Radiated acoustic pressure induced by structural vibration with an acoustic wavenumber corresponding to the structural vibration mode $<m,n>$
$p_{bl}(\mathbf{y},t)$	Pressure due to boundary layer
r	Radial location of observer in duct
r_0	Radial location of source in duct
r_{mn}	Radiation resistance per unit area due to fluid loading for structural vibration mode $<m,n>$
$S_n(k)$	Shape function for mode *n*
T	Magnitude of uniform string or membrane tension
T_{dipole}	Dipole transfer function, ratio of acoustic pressure to dipole force
$T_{rotor,m}$	Rotor transfer function for circumferential mode *m*
U_c	Convection velocity
U_0	Free stream velocity

V	Fourier transform of velocity
$\mathbf{V}_{px1}$	Real component of MPI at each point for a single frequency
W	Spanwise structure length
$\boldsymbol{W}_{pxp}$	Weighting matrix
x	Axial location of observer in duct
x_0	Axial location of source in duct
Δx	Separation distance in the streamwise direction
Δy	Separation distance in the spanwise direction
α_{mn}	Mode-dependent frequency parameter for ducted acoustics, as calculated by Equation (6.8)
β	Fluid loading factor
δ_{mn}	Dirac delta function
ε_d	Equal to ½ for m=0 and equal to 1
$\mathcal{F}^*$	Non dimensional forcing function $\left(\mathcal{F}^* = \frac{[\Phi_{ff}(f)]_{rotor}}{8{\rho_0}^2 {U_{tip}}^3 {r_{tip}}^5}\right)$
$\frac{d\mathcal{F}_{M0}(x_0, r_0, \theta_0, \omega)}{d\theta_0}$	Dipole force concentration of dipole ring
$\mathbf{\Psi}_{pxb}$	Matrix of mode shapes
$\psi_n(\boldsymbol{y})$	Spatial-dependent eigenfunction of vibration for mode n
λ	Wavelength
η_n	Damping ratio for mode n
η_s	Structural component of the damping ratio
η_{rad}	Acoustic-induced damping ratio due to fluid loading
$\Phi_{pp}(\omega)$	Auto-spectral density of pressure

$\Phi_{p,n}(\omega)$	Auto-spectral density of projected wall pressure for mode *n*
$\Phi_{v,n}(\omega)$	Auto-spectral density of velocity for mode *n*
Ω	Non-dimensional frequency for calculation of duct structural dispersion curve
ρ	Density of structure
ρ_0	Density of fluid medium
φ	Rotor blade stagger angle
$\xi(\boldsymbol{y},t)$	Flexural displacement of structure normal to surface
θ	Circumferential location of observer in duct
θ_0	Circumferential location of source in duct
μ_{mn}	The *n*-th zero of derivative of Bessel function, defined such that $J'_m(\mu_{mn})=0$
σ_{mn}	Modal radiation efficiency for structural vibration mode <*m*,*n*>
σ'_{mn}	Mode-dependent parameter which determines the broadband magnitude for ducted dipole acoustics, as calculated by Equation (6.9)
ν	Poisson's ratio
ω	Angular frequency
ω_n	Undamped natural frequency
ψ_M	Time phase of oscillation for mode *M* of a ring of dipoles
ψ_{M0}	Arbitrary shift to ψ_M based on reference time and location chosen
γ_1	Experimentally-determined spatial coherence decay constant for Corcos model

γ_2	Experimentally-determined spatial coherence decay constant for Corcos model

CHAPTER 1

INTRODUCTION

Flow-induced structural acoustics involves the study of the vibration of a structure induced by a fluid flow as well as the resulting sound generated and radiated by the motion of the structure. This thesis will examine statistically stationary structural vibration which is induced solely by low Mach number flow over the surface of the structure. The analysis will be restricted to thin structures with small magnitudes of motion which do not alter the flow field.

Flow-induced structural acoustics under these conditions are relevant in numerous applications. For example, the noise pollution generated by ventilation systems and aircraft engines often places practical limitations on the design of such systems. As another example, the fuselage of an aircraft experiences an external flow which induces structural vibration; this can in turn radiate acoustics internal to the fuselage. Another practical application involves rockets utilized to transport cargo such as satellites into space, formally known as carrier rockets. These carrier rockets are structurally similar to a sealed duct, and the pressures generated within can cause damage to expensive, sensitive cargo within the carrier rocket.

1.1 Background and Focus of Current Research

Blake [1] divides the method of solving a flow-induced structural acoustics problem into three general steps. First, a model is developed for the stochastic wall pressure of the flow field. Second, the wall pressure model is used in conjunction with the structural response model to predict the structural vibration. This is often accomplished by decomposing the structure into its modes of vibration and then treating each mode as an independent single degree of freedom system. The final step involves predicting the acoustic radiation due to the vibration of the structure. These three steps are applicable to any flow-induced structural acoustics system. This thesis will examine two specific systems: a thin, rectangular structure excited by a turbulent boundary layer and a thin-walled duct excited by an internal rotor.

1.1.1 Solution Steps For Flow Over An Elastic Flat Plate

Turbulent flow over a flat plate is a commonly-encountered problem. Figure 1.1 shows the flow chart of the various steps required in modeling the acoustic radiation due to turbulent flow over a flat plate and is separated into the three previously outlined steps. Orange blocks correspond to substeps involving modeling the fluid flow and corresponding excitation pressure. Blue blocks correspond to substeps involving modeling the structural vibration. Red blocks correspond to modeling the acoustic radiation.

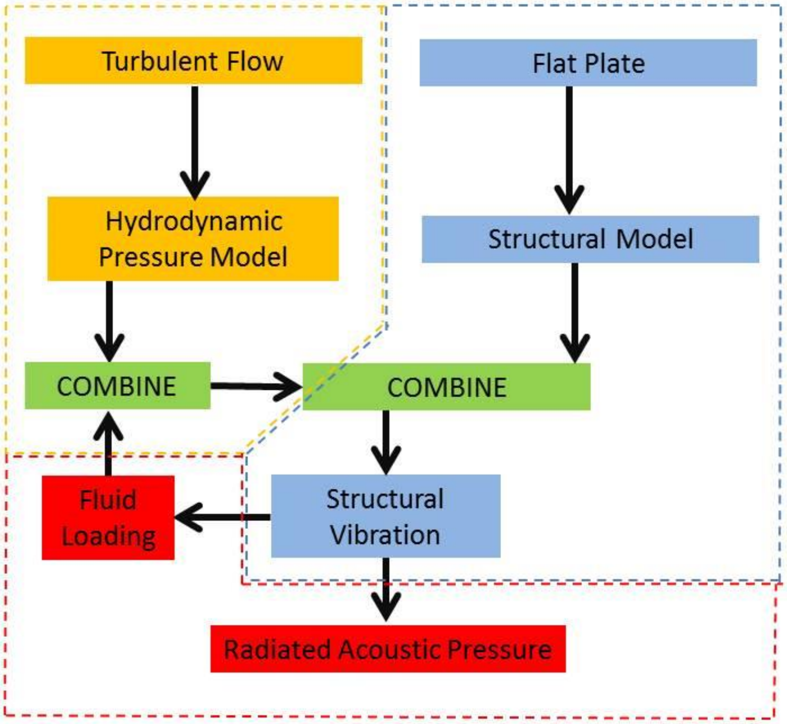

Figure 1.1. Flowchart of solution procedure for turbulent flow over a flat plate.

The solution requires modeling the stochastic and spatial properties of the wall pressure of the flow field. A simple and well-studied case is that of a fully-developed turbulent boundary layer over a smooth, flat plate with zero pressure gradient. For this situation, the most common models used are those of Corcos [2,3], Chase[4,5], and Smol'yakov-Tkachenko [6]. A limited number of more complex flows have been studied by various authors. Schloemer [7] studied the convection speed and spatial characteristics of the wall pressure of a turbulent boundary layer subjected to favorable or adverse pressure gradients. Fricke [8] studied separated flows due to a fence in the flow. Farabee and Casarella [9,10] studied the flow due to forward and backward facing steps.

The step of solving the structural vibration requires modeling the response of the structure to an arbitrary wall pressure excitation. Blake [1] discusses a method for modeling an in vacuo finite-length structure subjected to stochastic forcing by decomposing the vibration into a series of spatial mode shapes and assuming each shape vibrates independently. The wall pressure model and the structural model are then combined to predict the structural vibration.

The vibration of a structure can be utilized to predict the corresponding acoustic radiation, as is extensively discussed by Blake [1]. For the in vacuo case of a structure in an unbounded fluid medium, the acoustic radiation generated by the structural vibration has no effect on the vibration of the structure. In the case of heavy fluid loading, where the mass of the fluid medium is large relative to that of the structure, the acoustic pressure generated by the structural vibration can itself contribute substantially to the wall pressure, creating a feedback which excites structural vibration. In such cases, the acoustic pressure can be modeled as adding mass and damping to the structure. Furthermore, because the speed of sound in general is not the same as the wave bending speed within the structure, the feedback pressure generated by a specific mode of vibration can induce a wall pressure of a different mode, causing the modes of vibration to become coupled. These factors induced by the fluid loading must be combined with the turbulence model in order to predict the wall pressure model that must then be combined with the structural vibration model.

1.1.2 Solution Steps For a Ducted Rotor

Part of the objectives of this thesis was to apply the results of the relatively simple system of turbulent flow over a flat plate to a more complicated system. A rotor within a duct was selected because it has analytically tractable boundary conditions and is a frequently encountered system in practice. Despite the added complexity, the solution process follows a similar set of steps to that of a canonical flat plate excited by a turbulent boundary layer. Figure 1.2 shows the flow chart of the various steps required in modeling the acoustic radiation due to ducted rotor generating flow within a duct. As with Figure 1.1, in Figure 1.2 the flowchart is separated into the steps of modeling the flow/excitation, modeling the structure, and modeling the acoustics.

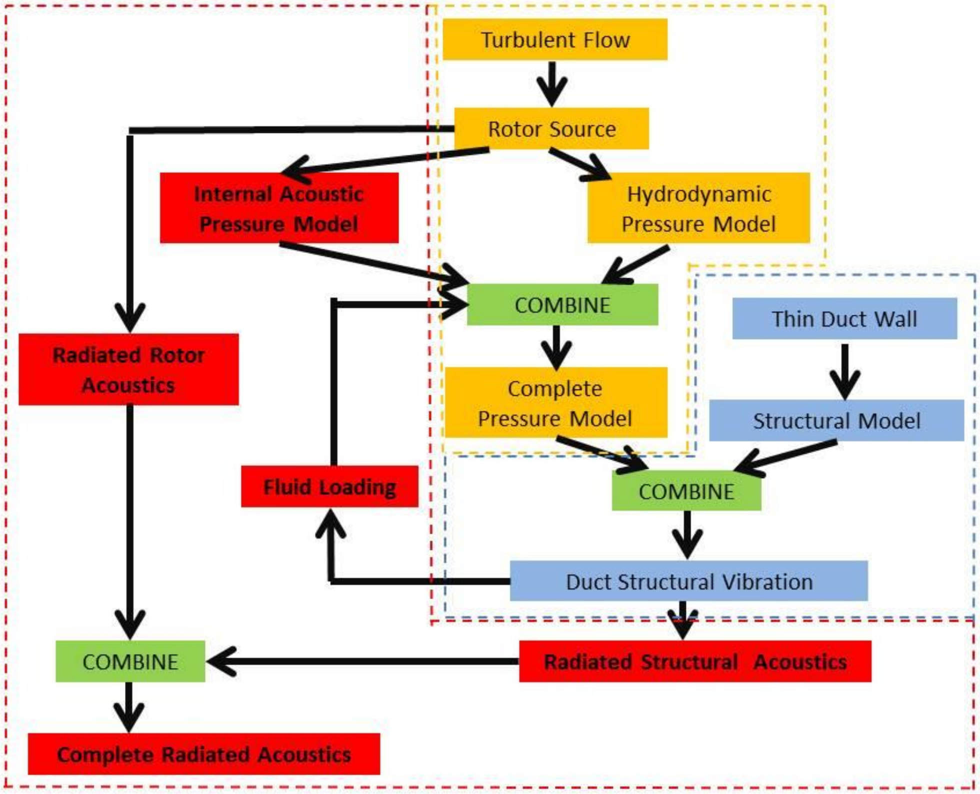

Figure 1.2. Flowchart of solution procedure for a ducted rotor.

When turbulent flow passes through the rotor, three pressure fields are generated: the acoustics radiated external to the duct, the acoustics internal to the duct, and the hydrodynamic pressure field. Investigation of the acoustics radiated externally from the duct due to the rotor was performed by Stephens [11], Stephens and Morris [12], and Stephens et al. [13]. The predominant source of these acoustics was found to be turbulence ingestion noise, which corresponds to the acoustics generated when turbulent eddies in the incoming flow interact with the rotor. The second pressure field generated is the internal duct acoustics, which is generated by a similar mechanism to the ingested turbulence noise and will be discussed in Chapter 6. The hydrodynamic pressure field has similar characteristics to that of turbulent boundary layer flow. The complete wall pressure model for the internal pressure field is obtained by combining the latter two pressure fields.

The structural aspects of the solution procedure for a ducted rotor are identical to those of a flat plate. A structural model must be developed to predict the vibration of the thin duct due to an arbitrary pressure field. This model is then combined with the complete wall pressure model to determine the vibration of the shell. As with the case of a flat plate, the structural vibration can induce a wall pressure feedback if the surrounding fluid medium is heavy enough.

Like in the case of a flat plate, the structural vibration induces acoustic radiation external to the duct. Prediction of this radiation is believed to be well understood in the literature. The acoustic radiation due to the structural vibration must then be combined with the acoustic radiation from the rotor itself in order to determine the complete radiated acoustic pressure field.

1.2 Summary of Research Questions

The final goal of this research was to examine the vibration of a fluid-loaded duct due to flow induced by an internal rotor. In order to do so, several other research questions were first encountered.

In Chapter 4, a measurement technique termed Magnitude Phase Identification (MPI) is developed to measure the modal vibration of a structure. Accelerometers could not be used as structures which are thin enough to be fluid loaded in air would have their mass substantially altered by the application of accelerometers. Laser Doppler velocimetry (LDV) was used to measure the vibration of the structure, but it is impractical to simultaneously measure the vibration of all points of a structure using LDV's due to the size and cost of these devices. MPI was developed to provide a method of experimentally determining the auto-spectral density of vibration of each mode using two-points measurements. In order to validate the technique, MPI was applied to the vibration of a non-fluid-loaded, rectangular structure excited by canonical turbulent boundary layer flow, and the results were compared to theoretical predictions of the vibration of each mode.

Chapter 5 will investigate structural vibration under the simultaneous effects of non-homogeneous forcing and fluid loading. These simultaneous effects are common in systems such as those involving underwater propulsion, where the mass of water often results in a fluid loaded structure. When both effects were present simultaneously, it was shown that the mode shapes become dependent on the forcing function, with the mode shapes skewing towards the locations where forcing is greater. It was shown experimentally that this did not occur when these effects were applied individually. A discretized string model was created to demonstrate that this effect can be attributed to the high damping caused by fluid loading.

Chapter 6 examines the internal acoustic wall pressure field of a ducted rotor. It was shown that the acoustics of the rotor could be modeled by replacing the rotor with a continuous ring of dipoles located at the blade tip. The finite length of the duct is accounted for by applying a method of images to the ring of dipoles relative to the duct inlet and exit.

Chapter 7 examines the final case of a fluid-loaded duct excited by an internal rotor. This case utilizes the answers of the previous research questions. The duct wall is sufficiently thin that accelerometers would alter the vibration of the duct, so the MPI derived in Chapter 4 is required for the LDV's to obtain measurements of the modal content of the vibration of the duct. The duct is fluid-loaded, so the conclusions of Chapter 5 are required to explain the duct vibration. The internal wall pressure examined in Chapter 6 excites the duct wall.

The layout of this thesis will be as follows. Chapter 2 will review important literature for the topics of this thesis. Chapter 3 will discuss the experimental setups used in this research, which involves the measurement of the wall pressure and the structural vibration of a thin steel plate and a ducted rotor. Chapter 4 will outline use of the magnitude-phase identification (MPI) method for experimentally determining the auto-spectral density of the vibration of each mode of a structure. Chapter 4 also uses MPI to compare the experimental and theoretical auto-spectral densities of vibration of various modes for the canonical case of a non-fluid-loaded plate excited by a spatially-homogeneous turbulent boundary layer. Chapter 5 expands upon the work detailed in Chapter 4 by examining the effects of fluid loading and non-homogeneous forcing in order to show that a fundamental change occurs in the vibration of a structure when both of these effects are present simultaneously, but not when they are present individually. Chapter 6 will discuss the method for solving the internal acoustic pressure field of a ducted rotor as well as measurements validating these predictions based on previous work by Stephens [11], Stephens and Morris [12], and Stephens et al [13]. Such predictions have not been published in the literature with the exception of papers by the author of this thesis [14]. Chapter 7 will detail the final case, that of a fluid-loaded duct wall excited by an internal ducted rotor. Chapter 8 will describe conclusions of the paper.

CHAPTER 2

BACKGROUND AND LITERATURE REVIEW

This chapter focuses on reviewing literature related to this thesis, which is divided into two topics. Section 2.1 focuses on literature related to predicting the vibration of thin structures. Section 2.2 focuses on literature related to modeling wall pressure spectra.

2.1 Structural Vibration

This review will focus primarily on literature which provides a basis for the analytical and experimental prediction of the response of a thin rectangular plate or duct wall subjected to stochastic, potentially non-homogeneous forcing under both in vacuo and fluid loaded conditions.

Blake [1] provides an extensive review of the fundamental equations of structural vibration. In his analysis, the initial assumption is that any differential element of the structure can be modeled as a mass-spring-damper, where the standard spring force is replaced by a linear restorative force that is dependent on the type of structure involved. The governing equation for a structural element then takes the form

$$m_s\ddot{\xi} + C_d\dot{\xi} + L(\xi) = -p(\vec{y},t) \qquad (2.1)$$

where C_d is the viscous damping, $p(\boldsymbol{y},t)$ is the fluctuating load per unit area on the surface of the structure, and $L(\xi)$ is a linear operator representing the restorative force of the structure. For the cases of a one-dimensional structure, m_s and $p(\boldsymbol{y},t)$ should be replaced by their one-dimensional analogs of m_L and fluctuating loads per unit length, respectively. The linear operator $L(\xi)$ is the only significant difference between different types of structures and is given by

$L(\xi) = T\nabla^2\xi$ for a membrane subjected to uniform tension T , (2.2a)

$L(\xi) = D_s\nabla^4\xi$ for a thin plate of uniform stiffness D_s , (2.2b)

$L(\xi) = T\frac{d^2\xi}{dx^2}$ for a string of uniform tension T , (2.2c)

$L(\xi) = D_s\frac{d^4\xi}{dx^4}$ for a beam of uniform stiffness D_s . (2.2d)

Here, the stiffness term D_s is defined as

$D_s = \frac{Eh^3}{12}$ for a beam, (2.3a)

$D_s = \frac{Eh^3}{12(1-\nu^2)}$ for a plate. (2.3b)

Note that the form of $L(\xi)$ can potentially be used to model structures other than the ones listed. For example, if one were to set $L(\xi)=k_{spring}\,\xi$, where k_{spring} is the spring constant of a linear spring, Equation (2.1) becomes the familiar equation for a mass-spring-damper. Because the restorative force in Equation (2.2) is based on the spatial gradient of the deflection, the deflection of all points on the structure are coupled.

To solve a bounded system, the response of the structure is separated into orthogonal eigenfunctions, each of which has a unique and in general independent resonant frequency. As detailed by Blake [1], one can assume that the solution to the equations of motion for a plate takes the form

$$\xi = \sum_{n=1}^{\infty} a_n \psi_n(\vec{y}) g_n(t) \quad , \qquad (2.4)$$

where n is an integer representing the mode number, a_n is a constant coefficient for mode n, $\psi_n(\boldsymbol{y})$ is a spatial-dependent eigenfunction for mode n, and $g_n(t)$ is a time-dependent coefficient function for mode n.

The eigenfunctions $\psi_n(\boldsymbol{y})$ must be orthogonal to one another, must satisfy Equation (2.1) for the case of p=0, and must satisfy the boundary conditions of the problem. In many two-dimensional systems the eigenfunctions demonstrate the property of separability based on the two independent coordinates. In such cases, it is common to write Equation (2.4) in a form similar to

$$\xi = \sum_{m=1}^{\infty} \sum_{n=1}^{\infty} a_{mn} \psi_m^{(1)}(y_1) \psi_n^{(2)}(y_2) g_{mn}(t) = \sum_{m=1}^{\infty} \sum_{n=1}^{\infty} a_{mn} \psi_{mn}(\vec{y}) g_{mn}(t) \ . \quad (2.5)$$

Note that for separable eigenfunctions, Equation (2.4) and both forms of Equation (2.5) are simply different methods of writing an identical expression and amount to little more than a different method of indexing the summation.

The eigenfunctions of the structure have no inherent magnitude to them. Blake [1] chooses to normalize the magnitude of the eigenfunctions as per

$$\iint_{A_p} \psi_m(\vec{y}) \psi_n(\vec{y}) dA = A_p \delta_{mn} \quad , \qquad (2.6)$$

where A_p is the area over which the eigenfunctions are defined (i.e. the area of the structure) and δ_{mn} is defined as being equal to 1 for $m=n$ and equal to zero otherwise. Equation (2.6) both expresses the magnitude of the eigenfunctions and enforces the orthogonality condition. Unless otherwise noted, this is the normalization for the eigenfunctions that will be utilized in this thesis.

The expression of a function as an infinite series of orthogonal basis functions will be termed a "modal expansion"; similarly, the calculation of the magnitudes of each of these basis functions will be referred to as "modal decomposition". The term "Fourier series" will be reserved for the special case of a modal expansion using sine/cosine functions.

Using Equation (2.4), the linear stiffness operator can be rewritten as

$$L\big(\psi_n(\vec{y})\big) = D_s {k_n}^4 \psi_n(\vec{y}) g_n(t) \qquad \text{for bars and plates ,} \qquad (2.7a)$$

$$L\big(\psi_n(\vec{y})\big) = T {k_n}^2 \psi_n(\vec{y}) g_n(t) \qquad \text{for strings and membranes .} \qquad (2.7b)$$

where k_n is the wavenumber associated with the eigenfunction $\psi_n(\boldsymbol{y})$. The wavenumber is defined as

$$k = \frac{\omega}{c} = \frac{2\pi}{\lambda} \qquad , \qquad (2.8)$$

where ω is the angular frequency of vibration, c is the speed of the wave, and λ is the wavelength of the wave. For structural vibration, c represents the bending speed of the wave and λ is the wavelength associated with this eigenfunction.

By substituting Equation (2.4) into Equation (2.1) and making use of the orthogonality condition, Equation (2.1) can be recast as a series of second order equations corresponding to one spatial mode each, given by

$$\left[m_s \ddot{g}_n(t) + C\dot{g}_n(t) + D_s k_n{}^4 g_n(t)\right] a_n = -\frac{1}{A_p}\iint_{A_p} p(\vec{y},t)\psi_n(\vec{y})dA = -P_n(t) \quad . \qquad (2.9)$$

Here, $P_n(t)$ can be interpreted as the wall pressure field projected onto the shape of the eigenfunction. One will note that the equation for each mode is identical to that of a mass-spring-damper, where the damping is a "loss factor" unique to each mode. The undamped natural frequency for mode n is then readily found to be

$$\omega_n{}^2 = k_n{}^4 \frac{D_s}{m_s} \qquad \text{for a plate} \quad , \qquad (2.10a)$$

$$\omega_n{}^2 = k_n{}^2 \frac{T}{m_s} \qquad \text{for a membrane} \quad . \qquad (2.10b)$$

Equation (2.9) can be viewed as the governing equation for bounded structural dynamics. However, it is designed for use with deterministic functions, while turbulent boundary layers are inherently stochastic in nature. Thus, Equation (2.9) must be converted into a stochastic form.

As defined by Blake [1], let the temporal Fourier transform pair of velocity be defined as

$$V(t,\boldsymbol{y}) = \int_{-\infty}^{\infty} V(\omega,\boldsymbol{y}) e^{-i\omega t} d\omega \quad , \qquad (2.11a)$$

$$V(\omega,\boldsymbol{y}) = \frac{1}{2\pi}\int_{-\infty}^{\infty} V(t,\boldsymbol{y}) e^{i\omega t} dt \quad . \qquad (2.11b)$$

where V(ω,***y***) represents the velocity at a specific frequency and can be expressed by a spatial modal expansion of

$$V(\omega, \boldsymbol{y}) = \sum_n V_n(\omega)\psi_n(\vec{y}) \qquad . \tag{2.12}$$

While Equation (2.11) is explicitly a temporal expansion of sine and cosine basis functions, no assumptions should be made as to the basis functions used in the spatial modal expansion of Equation (2.12). Combined, these provide a modal expansion of the velocity in terms of both space and time.

As long as the fluid loading on the structure is light (to be further detailed later), then one can assume that the modes are uncoupled. In this case, Equation (2.9) can be re-written in terms of the Fourier quantities as

$$\frac{V_n(\omega)}{P_n(\omega)} = \frac{i\omega}{m_s[(\omega_n{}^2-\omega^2)-i\eta_n\omega_n\omega]} \qquad , \tag{2.13}$$

where $P_n(\omega)$ is the Fourier transform for $P_n(t)$ as defined in Equation (2.9); one can envision this as the temporal-spatial modal expansion of the pressure field on the structure, much like Equation (2.11) is the temporal-spatial modal expansion of the velocity field. η_n is a mode-dependent damping ratio that replaces the viscous damping term C_d used earlier. For lightly fluid loaded cases η_n is caused by structural damping η_s, but for heavily fluid-loaded cases an acoustic radiation damping factor η_r should be added to this. The transfer function based on auto-spectral density can be written as

$$\frac{\Phi_{v,n}}{\Phi_{p,n}} = \frac{\omega^2}{m_s{}^2[(\omega_n{}^2-\omega^2)^2+(\eta_n\omega_n\omega)^2]} \qquad , \tag{2.14}$$

where $\Phi_{v,n}$ and $\Phi_{p,n}$ are the coefficients associated with mode n of the spatial modal decomposition of velocity and pressure, respectively; these also correspond to the auto-spectral density of mode n of the vibration and pressure, respectively. Equation (2.14) is the governing equation of structural dynamics for a single mode in the spectral domain, and is identical to the spectral transfer function for a mass-spring-damper.

The response of the structure is can be split into two frequency regimes. For low frequencies over which the resonant frequencies of excited modes are separated by large differences in frequency, each mode can be analyzed as an individual mass-spring-damper, and the total response is obtained by simply adding these responses. For higher frequencies, the differences in resonant frequencies tend to become so small that for any given frequency multiple modes will be resonating. In such cases, one utilizes the modal density, defined as the number of resonant frequencies present within a change in frequency. The forcing function acting on the structure is then integrated across these modes, where for low damping the resonant peak dominates the structural response function. This thesis will primarily focus on the former regime, where modal density is low.

Blake discusses that, as the structure vibrates, acoustic waves are generated which contribute to the wall pressure exciting the structure, creating a feedback loop. The effect is negligible if the structure is not fluid loaded. The fluid loading factor is defined by Blake[1] as

$$\beta = \frac{\rho_0 c_0}{m_s \omega} \quad , \qquad (2.15)$$

where c_0 is the speed of sound in the fluid medium, ρ_0 is the density of the fluid, m_s is the mass per unit area of the structure, and ω is the angular frequency of vibration. Noting that c_0/ω is proportional to the wavelength of the acoustic wave, one can interpret Equation (2.15) as being the ratio of the mass per unit area of a wavelength of the fluid to the mass per unit area of the structure; hence, high values of β correspond to systems where the mass of the fluid is large compared to the mass of the structure. In particular, structures are considered to be fluid loaded for values of $\beta >> 1$. Blake assumes that the total pressure on the structure can be written as

$$p(\boldsymbol{y}, t) = -p_a(\boldsymbol{y}, t) + p_{bl}(\boldsymbol{y}, t) \quad , \qquad (2.16)$$

where p_{bl} is the pressure induced by the boundary layer and p_a is the pressure induced by the acoustic radiation, such that when fluid loading is small, p_a will be negligible. It is still assumed that the vibration of the structure does not change the flow field of the fluid, such that p_{bl} is unaffected by the structural vibration. Utilizing the shape functions of the structure, Blake derives that p_a for mode $<m,n>$ of vibration is given by

$$p_{a,mn}(y_2, \omega) = \frac{1}{(2\pi)^2} \rho_0 c_0 \sum_{op} V_{op}(\omega) \iint_{-\infty}^{\infty} \frac{S_{mn}(\boldsymbol{k}) S_{op}(\boldsymbol{k})}{\sqrt{1-\left(\frac{k}{k_0}\right)^2}} e^{iy_2\sqrt{{k_0}^2-k^2}} d\boldsymbol{k} \quad , \qquad (2.17)$$

where the summation is carried out for all modes $<o,p>$, the integration is carried out for all wavenumbers, and the resulting pressure is for mode $<m,n>$. k_0 is the acoustic wavenumber (equal to ω/c_0). y_2 is the location perpendicular to the surface of the structure, such that $y_2=0$ represents the location of the surface of the structure. The modal shape function is defined as

$$S_n(\boldsymbol{k}) = \iint_{A_p} e^{-i\boldsymbol{k}\cdot\boldsymbol{y}}\,\psi_n(\boldsymbol{y})\,d\boldsymbol{y} \qquad . \qquad (2.18)$$

Even though the eigenfunctions are orthogonal, there exists no orthogonality condition for the modal shape functions, and as such, the integral in Equation (2.17) is not necessarily zero for <*m*,*n*>≠<*o*,*p*>. Thus, it is possible for the <*m*,*n*> modes of vibration of the structure to induce an acoustic pressure field at the <*o*,*p*> mode of vibration, creating modal coupling.

Even for a fluid loaded structure, if the fluid loading is not too large, the effects of the modal coupling can be neglected. In such cases, the integration of Equation (2.17) is only non-zero for $mn=op$. Combining this with $y_2=0$ (i.e. along the wall) yields

$$p_{a,mn}(y_2 \to 0, \omega) = \frac{1}{(2\pi)^2}\rho_0 c_0 V_{mn}(\omega) \iint_{-\infty}^{\infty} \frac{|S_{mn}(\boldsymbol{k})|^2}{\sqrt{1-\left(\frac{k}{k_0}\right)^2}}\,d\boldsymbol{k} \qquad . \qquad (2.19)$$

The primary acceptance region of Equation (2.19) corresponds to values of the variable of integration **k** which are close to the $\boldsymbol{k}_{mn}$, the wavenumber associated with the eigenfunction of that mode, because the shape function of a given mode is largest for wavenumbers that correspond to this mode.

Two important cases of Equation (2.19) emerge. If the magnitude of k_{mn} is significantly less than k_0 (corresponding to cases where the wavelength of vibration in the structure is greater than the wavelength of sound), then the denominator and thus the overall integration in Equation (2.19) is predominantly real. In this case, p_a can be thought of as a real impedance on the structure, which results in the acoustic backpressure appearing as a resistance or damping terms. If the magnitude of k_{mn} is significantly larger than k_0 (corresponding to cases where the wavelength of vibration in the structure is less than the wavelength of sound), then the denominator and thus the overall integration in Equation (2.19) is predominantly imaginary. In this case, p_a can be thought of as an imaginary impedance on the structure, which appears as an inertial term or added mass to the structure. As there are an infinite number of wavenumbers and eigenfunctions present in the structure, it is possible that both effects can be present at the same time. Thus, even in the case of negligible modal coupling, heavy fluid loading has the effect of increasing the apparent mass and/or damping of the structure.

Recognizing these two effects, the acoustic pressure can be written in the form

$$p_{a,mn}(0,\omega) = (r_{mn} - i\omega m_{mn})V_{mn}(\omega) \quad . \qquad (2.20)$$

Here, m_{mn} is the accession to inertia per unit area (i.e. the added mass) and corresponds to the imaginary portion of Equation (2.19). For rectangular plates in the low frequency region this is given by

$$m_{mn} = \frac{\rho_0}{k_{mn}} \qquad (2.21)$$

for values of $k_{mn}>k_0$; for more complex situations the integration in Equation (2.19) must be carried out for the specific geometry. r_{mn} is the radiation resistance per unit area and is given by

$$r_{mn} = \rho_0 c_0 \sigma_{mn} \quad , \qquad (2.22)$$

where σ_{mn} is the modal radiation efficiency, defined by

$$\sigma_{mn} = \frac{1}{A_p(2\pi)^2} \iint_{k<k_0} \frac{|S_{mn}(\boldsymbol{k})|^2}{\sqrt{1-\left(\frac{k}{k_0}\right)^2}} d\boldsymbol{k} \qquad , \qquad (2.23)$$

which is the real portion of Equation (2.19). For wavenumbers such that $k_0 >> k_{mn}$, σ_{mn} is roughly equal to one.

With these values, Blake [1] rewrites the governing equation of motion for a single mode of a plate as

$$[(-m_s - m_{mn})\omega^2 - i\omega(m_s\eta_s\omega_{mn} + \rho_0 c_0 \sigma_{mn}) + {\omega_{mn}}^2 m_s]V_{mn}(\omega) = i\omega p_{bl,mn}(\omega) \, , \quad (2.24)$$

where η_s is the structural component of the damping ratio and ω_{mn} is the in-vacuo resonance frequency of the plate for mode $<m,n>$. The natural frequency of the each mode of the fluid-loaded system is given by

$$({\omega_{mn}}^2)_{fluid-loaded} = ({\omega_{mn}}^2)_{in-vacuo} \left(\frac{m_s}{m_s+m_{mn}}\right) \quad . \qquad (2.25)$$

The acoustic radiation component to the system's damping ratio is given by

$$\eta_{rad} = \beta\sigma_{mn} \qquad , \qquad (2.26)$$

with the damping ratio of the system being the sum of the structural and radiation damping. For plates which are not fluid loaded, the fluid loading factor of a plate at its first natural frequency will roughly quadruple when its thickness is cut in half. This is due to both the mass per unit area being reduced by half and the natural frequency roughly doubling, both of which influence the fluid loading factor. As the natural frequency is dependent on the fluid loading factor, as shown by Equation (2.25), the fluid loading factor will be slightly larger than this relationship implies when fluid loading is significant.

Skelton and James [15] performed an analysis of a fluid-loaded infinite plate based on the equation of motion developed by Sophie Germain for a thin plate in pure bending. Because the analysis is completed for an infinite plate rather than a bounded plate, the quantities of the system are converted to spectral field quantities rather than the discrete mode numbers and eigenfunctions present in a bounded system. Like Blake, Skelton and James conclude that the fluid loading terms appear as a resistance for cases where the structural wave number is less than the acoustic wave number and that the fluid loading terms appear as a mass for cases where the structural wave number is greater than the acoustic wave number. Unlike Blake, Skelton and James make no mention of the possibility of modal coupling, likely because the analysis of Skelton and James makes no mention of modes.

Leissa [16,17] analyzed the response of specific shell (referring to a structure which is too thin support bending moments) and plate geometries as derived from the fundamental equations of motion for these structures. In the case of shells, Leissa presented various simplifications as proposed by previous authors and evaluated the results of these simplifications, usually through use of the principle of virtual work. In the case of plates, Leissa directly solved the fourth order equation of motion for a plate. Leissa's shell analysis focused primarily on thin cylindrical ducts, though certain non-cylindrical geometries received a small amount of attention. The plate analysis primarily focused on circular and rectangular plates. In each of these cases, Leissa examined the characteristics of the structure under a plethora of boundary conditions. Most of the results focused on the natural frequencies and mode shapes of the lowest-frequency modes of the structures.

Morse and Ingard [18] provided a derivation and then analysis of the equations of motion for strings, rigid bars, membranes, and plates. While there are some differences between the one- and two-dimensional cases of structural vibration, the string functions much like a one-dimensional version of a membrane, and the rigid bar functions much like the one-dimensional version of a plate. Morse and Ingard highlight many of the phenomenona seen in membranes and plates by explaining them in the context of the simpler one-dimensional cases. Most notably analyzed is the concept of dispersive vs. non-dispersive waves, with dispersive waves showing unique characteristics due to their bending speed being frequency-dependent.

Filippi [19] analyzed the response of plates and membranes through use of energy methods such as the principle of virtual work. For simple homogeneous systems such analysis is simply a different method to reach the same conclusion as is obtained from application of Newton's Second Law. Filippi demonstrated how such methods can be utilized to solve non-homogenous structures, such as plates of varying thickness. In particular, Filippi analyzed the excitation and acoustic radiation of a thin baffled cylindrical shell by an internal turbulent flow.

Dyer [20] performed early work on the response of a thin plate due to random excitation which was later experimentally validated by Maestrello [21]. The correlations of the pressure field were assumed to have properties that are common in turbulent flows: exponential decay, small scales compared to the size of the plate, and constant convection speed over the plate. Dyer concluded that for excitation convection speeds much less than the bending wave speed of the plate that the convection speed has little effect on the plate response. However, when the convection and bending speeds are similar, the response can be considerably increased. Both Dyer and Maestrello found that the main energy of the vibrating structure was centered around the convection velocity, with the highest energy at the lowest frequency and wave number. Leibowitz [22] obtained similar results to Maestrello but expanded the work to account for additional effects such as both the added mass and acoustical damping effects imposed by fluid loading.

Davies [23] provided an early analysis on a thin plate adjacent to an infinite fluid-filled half space by beginning with the coupled fluid-structure equations, including damping effects in the structure, and solving these equations through use of spectral methods. Davies analyzed the effects of fluid loading as well as the relative importance of the structural damping, radiation damping, and modal coupling in the structure.

Han et al. [24] predicted the vibration of a thin plate using a method known as energy flow analysis. The premise of this analysis is that the energy of the system can be broken into stored energy, dissipated energy, and energy transferred between the structure and fluid, which must balance. Using a laser vibrometer, the vibration of a thin steel plate was measured when subjected to two different excitation flows: a developed turbulent boundary layer and a separated flow re-attaching partway along the plate. Using the Corcos and Smol'yakov models for the wall pressure spectra, Han was able to relatively accurately predict the vibratory response of the plate at various frequencies as measured in the experiment. Han [25] showed that energy flow analysis could be used in conjunction with computational fluid dynamics to determine the structural vibration in cases where little is known a priori about the flow field exciting the structure. In an extension to the studies by Han, Park et al. [26] utilized energy flow analysis to predict the response of a thin plate subject to non-canonical boundary conditions, such as boundary conditions which dissipated energy; the predictions were validated against experiments run during the course of the study.

Maury et al. [27] developed an extensive analytical method for utilizing spectral methods to predict the vibration of a thin plate subjected to a spatially and temporally stochastic pressure field. As examples of the application of this method, Maury et al. compared the structural response induced by a turbulent boundary layer to those of a diffuse acoustic field and a spatially uncorrelated pressure field. In the second portion of this paper, Maury et al. [28] were able to successfully predict aircraft panel vibration in high subsonic flow as measured in previous experiments through use of the Corcos model.

Ciappi et al. [29] performed an experimental simulation of flow over a ship hull by towing a model ship in a large water tank. The experimental method allowed for a heavily fluid loaded structural vibration problem without the background noise associated with circulatory systems such as pumps. A portion of the ship's hull was replaced with a thin Plexiglas plate and accelerometers were used to measure the response at eight random locations on the plate. The study of Ciappi et al. concluded that the Corcos model provided unsatisfactory prediction of the structural vibration, particularly at low frequencies. Meanwhile, the Chase model provided relatively accurate predictions of the structural vibration but tended to become inaccurate for higher frequencies, albeit an improvement over the Corcos model; however, the authors conceded that the mismatch between the prediction and experimental results at high frequencies may be caused by poor spatial resolution amongst the sensors in the experiment.

Several authors have developed methods other than classical solution methods for use in specific situations. Filippi et al. [30] demonstrated how the response of a fluid-loaded system can be solved based on any excitation, such as period, stochastic, or transient excitations, by expanding the resonance modes in the harmonic regime. Collery and Guyader [31] predicted plate vibration through a minimization of error technique. By using the mode shapes of the in-vacuo solution as a basis for the method, the analysis was able to predict the response of a fluid loaded plate with fewer calculations than required from the classical solution methods. Mazzoni [32] developed a method of predicting panel response from stochastic pressure field by approximating the field as a deterministic forcing function.

Finnveden [33] conducted a study on the structural vibration of a duct subjected to an internal turbulent boundary layer utilizing a modified version of the Corcos and Chase models. The study concluded that both models provided for reasonably accurate predictions of the structural vibration for low frequencies, but only the modified Chase model provided for accurate vibrational predictions at high frequencies. Grant [34] calculated the response for a fluid-loaded thin plate with smoothly varying elastic properties along the wall of a rectangular duct as well as the acoustic radiation of the plate, a first step in calculating the response for non-homogeneous structures.

2.2 Pressure Field Models

Prediction of the structural vibration of the system requires knowledge of the pressure field which is exciting it. Various models already exist in the literature to predict pressure fields under common flow conditions. The limitation here is that one cannot have a simple, comprehensive model for all possible flows and geometries. In this thesis the focus will be on the pressure fields of a turbulent boundary layer over a flat plate and the pressure inside of a duct induced by a rotor. Both of these systems receive at least some attention in the literature, and thus the focus of the research will be on how to effectively apply these models rather than development of completely new models.

All turbulent boundary layers are inherently stochastic in nature. To perform any analysis one must determine statistical parameters that allow the system to be solved in a deterministic fashion. Blake [1] provides an extensive outline on the use of correlations and spectra to define the stochastic pressure field in a deterministic form. Graham [35] and Han [36] provide summaries of some of the various wavenumber frequency pressure spectra models available.

2.2.1 Pressure Field for a Flat Plate Turbulent Boundary Layer

There are three common pre-existing choices for the wall pressure model of a fully developed turbulent boundary layer over a flat plate: the Corcos model [2,3], the Smol’yakov-Tkachenko model [6], and the Chase model [4,5]. Corcos provides a relatively simple formulation that utilizes the most basic statistics of a turbulent boundary layer over a flat plate to predict the wave number – frequency content of the pressure field. The Corcos model tends to drastically over-predict the pressure spectra for low wave numbers.

As summarized by Borisyuk and Grinchenko [37] and Han et al. [36], the Corcos model assumes that for a spatially and temporally homogenous pressure field, the pressure cross-spectral density between points *a* and *b* in rectilinear coordinates can be written as a separable function of the form

$$P_{ab}(\Delta y_1, \Delta y_2, \omega) = \Phi_{pp}(\omega) B_1(\omega \Delta x / U_c) B_2(\omega \Delta y / U_c) e^{-\omega \Delta x / U_c} \quad , \qquad (2.27)$$

where

- Δx is the separation distance between points *a* and *b* in the streamwise direction
- Δy is the separation distance between points *a* and *b* in the spanwise direction
- ω is the angular frequency of the pressure
- U_c is the convection velocity of the flow, often approximated as 70% of the free stream velocity
- $\Phi_{pp}(\omega)$ is the auto-spectral density of the pressure at point *a*; this will be the same at every point because of the assumption of spatial homogeneity.
- B_1 and B_2 are the separated portions of the function which determine the spatial relationship of the pressure model

B_1 and B_2 are often approximated as exponential decay functions, in which case the Corcos model becomes

$$P_{ab}(\Delta y_1, \Delta y_2, \omega) = \Phi_{pp}(\omega) e^{-\gamma_1 |\omega \Delta x / U_c|} e^{-\gamma_2 |\omega \Delta y / U_c|} e^{-\omega \Delta x / U_c} \quad , \qquad (2.28)$$

where γ1 and γ2 are chosen to obtain agreement with experimental results, with $\gamma_1 = \gamma_2 = 0.7$ being a common choice. For structural dynamics, it is generally more useful to use a pressure model with dependence on the wave number. This can be found by taking a Fourier transform of Equation (2.28), in which case one finds the wavenumber-frequency pressure spectra model to be

$$\Phi_p(k_x, k_y, \omega) = \Phi_{pp}(\omega) \frac{\gamma_1}{\pi\left[\left(\frac{k_x\omega}{U_c}-1\right)^2+{\gamma_1}^2\right]} \frac{\gamma_2}{\pi\left[\left(\frac{k_y\omega}{U_c}\right)^2+{\gamma_2}^2\right]} \quad , \qquad (2.29)$$

where k_x and k_y are the streamwise and spanwise wavenumbers, respectively, between points *a* and *b*; here, the wave number is defined as 2π divided by separation distance.

Efimtsov [38] followed the same philosophy as Corcos but developed new models for the correlation lengths based on an extensive series of measurements on aircraft. Following Efimstov, Smol'yakov and Tkachenko [6] based their model on the boundary layer thickness and separation distance. However, instead of assuming that the pressure spectra was a product of a streamwise contribution and a spanwise contribution (a characteristic known as separability), Smol'yakov and Tkachenko utilized a single coherence function combining both terms in a non-separable fashion. The resultant function was an improvement over Corcos for low wavenumbers but still over-predicted the pressure spectra for low wave numbers. To compensate, a series of correction factors was added in the low wave number regime.

Attempting to correct for the low wavenumber errors of the Corcos model, Ffowcs Williams [39] developed a model for the wave-number pressure spectra based on Lighthill's acoustic analogy, but the resultant expression contained several constants and functions which would have to be obtained experimentally; to the best knowledge of the author of this thesis, these still remain unknown. Chase [4,5] followed the same premise as the Ffowcs Williams but based on experience applied various assumptions which resulted in a new form which also contained several constants which must but also can be determined experimentally. Chase provided suggestions as to the values these constants should be set to, though these constants can be flow-dependent.

A generic comparison of these models was made by Borisyuk and Grinchenko [37], who concluded that Chase and Smol'yakov-Tkachenko provided the best agreement with experimental data as per Martin and Leehey [40]. Graham [35] also compared these models specifically with the intention of determining which models were most accurate for predicting structural vibration and acoustic radiation, particularly for cases pertaining to transport aircraft. Graham concluded that the best model to use was situationally dependent and that any of the three models were viable under certain conditions. Graham suggested that the Smol'yakov-Tkachenko model gave the most accurate results but that in some cases the additional accuracy may be too small to justify the substantially increased complexity of the model.

None of these choices receives exclusive praise as the best model to use in the literature, with various authors praising the merits of each of these models. Graham [35] provided a comparison of these models that is worth briefly reviewing. Graham's comparison is shown in Figure 2.1, showing the magnitude of the cross-spectral density for fixed spanwise locations. The horizontal axis is defined such that a value of one corresponds to the convective wave number. The convective wave number is defined as

$$k_c = \frac{\omega}{U_c} \quad , \tag{2.30}$$

where ω is the angular frequency and U_c is the convective velocity. The convective velocity is defined as the speed at which structures in the flow convect downstream and is often estimated to be roughly 70% of the free stream velocity.

Figure 2.1 shows that the models tend to be relatively close near the convective wave number (and even for this point there is disagreement amongst the models) but tend to diverge drastically for values not near the convective wave number. Chase and Smol'yakov-Tkachenko tend to show the closest agreement to one another. Note that Chase I was the original model developed by Chase whereas Chase II corresponds to a model that relaxes some of the analytical restrictions in the low wave number regime; the difference is generally negligible outside of the subconvective regime (corresponding to wave numbers less than the convective wave number). Corcos substantially over predicts both Chase and Smol'yakov- Tkachenko, with the predictions seeming worse in the subconvective regime than the superconvective regime.

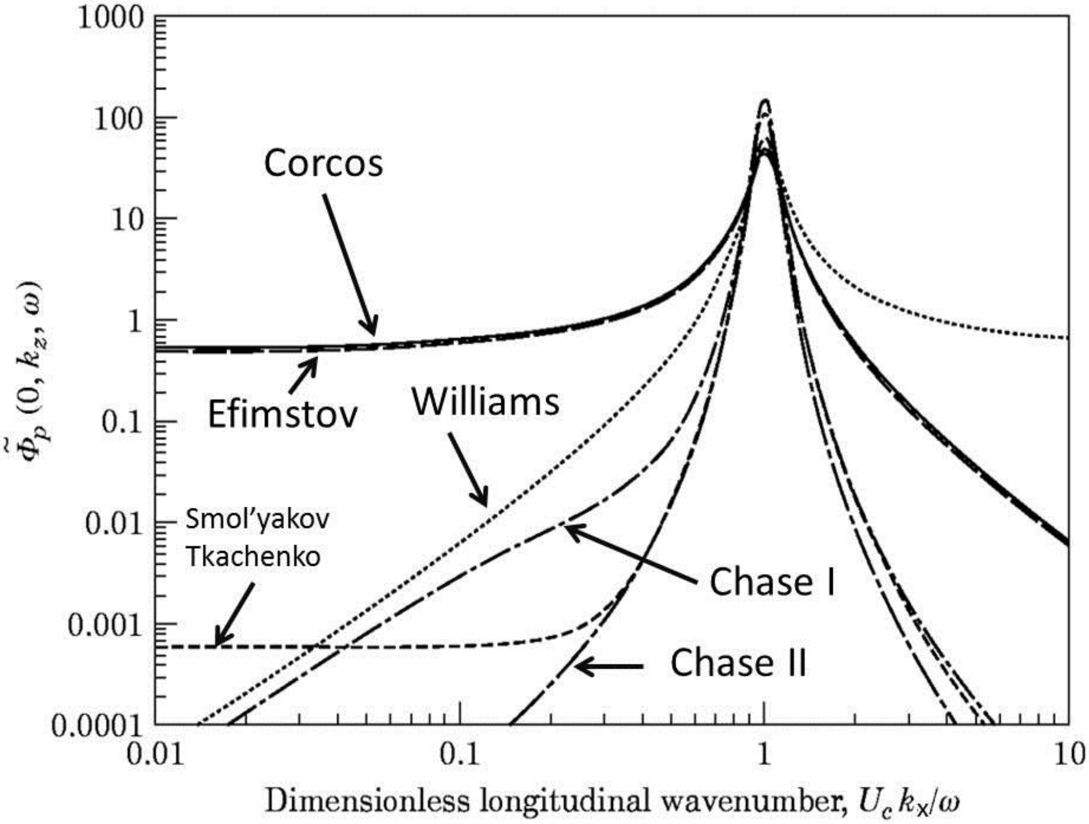

Figure 2.1. Comparison of the Corcos, Efimstov, Williams, Smol'yakov-Tkachenko, and Chase models. A horizontal axis value of one corresponds to the convective wavenumber.

A limited number of more complex turbulent boundary layer flows have been studied by various authors. Schloemer [7] experimentally measured the convection speed and spatial characteristics of the wall pressure of a turbulent boundary layer subjected to favorable or adverse pressure gradients. Schloemer concluded that, all else equal, the differences between the spatial characteristics in turbulent boundary layers subjected to adverse, zero, and favorable pressure gradients were primarily due to the difference in the convection velocity, with favorable pressure gradients having faster convection velocities and adverse pressure gradients having slower convection velocities. Fricke [8] studied the single-point root-mean-square pressure of separated flows due to a fence in the flow. Farabee and Casarella [9,10] studied the flow due to forward and backward facing steps.

As detailed previously, for a bounded structure, the wall pressure field enters the solution through the calculation of the projection of the pressure field onto the mode shapes of the structure, $P_n(t)$. The calculation of $P_n(t)$ is shown in Equation (2.9) and has no requirement for the wall pressure to be spatially homogeneous. In this regard the procedure for calculating the vibration of a structure subjected to non-homogeneous forcing should be identical to that of a structure subjected to homogeneous forcing as long as the non-homogeneous wall pressure can be modeled.

Use of the Corcos, Chase, or Smol'yakov-Tkachenko model requires a spatially statistically homogeneous wall pressure field. These models calculate the cross-spectral density of wall pressure between two points as being the product of the wall pressure auto-spectral density multiplied by a coherence-based factor dependent on separation distance. Following upon the work of Corcos, Schloemer [7] experimentally measured this coherence-based factor for adverse, zero, favorable pressure gradients and found that the difference in this factor between the three cases was primarily due to the change in convection velocity caused by the pressure gradient. Schloemer labels these factors the magnitude of the normalized longitudinal and lateral cross-spectral densities, which in this paper shall be denoted as A_f and B_f, respectively. These are defined as

$$A_f = \frac{|P_{ab}(\Delta x,0,\omega)|}{\Phi_{pp}(\omega)} \quad , \qquad \text{and} \tag{2.31}$$

$$B_f = \frac{|P_{ab}(0,\Delta y,\omega)|}{\Phi_{pp}(\omega)} \quad , \tag{2.32}$$

where Schloemer assumes that the auto-spectral density of pressure is spatially homogeneous. Schloemer experimentally determined A_f and B_f. As the convection velocity only affects the streamwise direction, Schloemer found that B_f was nearly identical for adverse and favorable pressure gradients. Schloemer's work implies that the Corcos, Chase, and Smol'yakov-Tkachenko models may be applicable to turbulent boundary layers where the pressure smoothly varies as long as the equations are modified to account for the change in convection velocity over the surface.

In the context of energy flow analysis, Han et al. [24] calculated the non-homogeneous spatial pressure properties of flow due to a fence upstream of the flow based on the work of Farabee and Casarella [9,10]. Farabee and Casarella experimentally measured flow over a forward and backward facing step, which produces unattached, re-attaching, and re-attached zones similar to the zones created by the fence used by Han et al. It was assumed that the three zones were completely uncorrelated. Han et al.'s calculation of the wall pressure field involved a combination of wall pressure measurements and computational fluid dynamics.

2.2.2 Pressure Field Due to a Ducted Rotor

The pressure spectra present in a duct can be separated into hydrodynamic and acoustic components. The radiated acoustic components were studied extensively by Stephens [11]; Stephens and Morris [12]; and Stephens et al [13]. In an extension of these works, the internal duct acoustics were studied by the author of this thesis and will be discussed in Chapter 5. The acoustic pressure spectra was assumed to be generated by the rotor interacting with a turbulent flow which acts as an unsteady pressure on the surface and thus generates sound. The previous authors found two turbulent sources which resulted in sound radiation from the rotor. The first source is known as "self noise", which arises when the flow passing over a rotor blade generates its own turbulent boundary layer along the blade, like flow over a flat plate would. The second source is known as "approach noise" and occurs when the rotor interacts with unsteady turbulent pressures in the incoming flow. The approach flow can be broken further into two components as categorized by Blake [1]: small scale turbulence, which interacts with only one rotor blade as it passes through, and large scale turbulence, which interacts with multiple blades. It was found that approach noise tends to dominate the radiated acoustics from a rotor, and thus in general self noise can be neglected when modeling the acoustics of a ducted rotor.

Hanson [41] studied turbulence ingestion noise generated by both periodic inflow disturbances and large scale anisotropic turbulence and identified sharp peaks in the resultant acoustic spectra from both sources, whereas previously these peaks had only been attributed to the former. Moiseev et al. [42] studied a ducted rotor with various inflow conditions and number of rotor blades, concluding that most of the sound was generated due to the interaction of the hub and tip regions of the rotor with the ingested boundary layer. Ganz et al. [43] performed an experiment which involved the capability to remove the boundary layer from the ingested flow. The study concluded that the boundary layer was a significant source of sound in a ducted rotor and was the cause of spikes in the sound spectra at multiples of the blade passing frequency.

Following the results of Ganz et al., many researchers have investigated the relationship between turbulent structures stretched in the axial direction and pressure spectra generated by the rotor with broad peaks at multiples of the blade passing frequency. Glegg and Walker [44] incorporated anisotropy into the wavenumber frequency pressure spectra based on three turbulent length scales, concluding that "long thin eddies stretched in the direction of the flow are more likely to cause blade tones or spectral humps than isotropic eddies". However, Joseph and Perry [45] found that the turbulent length scales reported by Ganz et al. were an order of magnitude too small to account for the broad humps at multiples of the blade passing frequency. Martinez [46] developed a model for determining the thrust and ultimately acoustic radiation of a rotor subjected to anisotropic turbulence. The analysis provided a physical explanation for the broad humps in the pressure-frequency spectra, deemed the "haystacks", around multiples of the blade passing frequency. Atassi and Logue [47] predicted broad humps at multiples of the blade passing frequencies by using by using rapid distortion theory to develop a wavenumber spectra model that can account for anisotropic turbulence. Furthermore, Golubev and Atassi [9] examined the effects on the internal acoustic field of a duct due to the presence of a swirling flow, which causes a refraction effect in the acoustic waves.

The aforementioned literature indicates that the primary source of acoustics radiated by a ducted rotor arises from the rotor tip interacting with long eddies contained within the ingested casing turbulent boundary layer flow, which corresponds to the previously-mentioned large scale turbulence. Such eddies are not necessarily correlated.

CHAPTER 3

EXPERIMENTAL SETUP

This chapter describes the two experimental models that were used to support the current research: one to study the structural vibration of a flat plate excited by a turbulent boundary layer, and one to study the structural vibration of a duct excited by an internal rotor. While these two experimental setups are largely independent of one another, each was designed to allow for measureable structural vibration, measureable wall pressure, and controllable structural and acoustic boundary conditions.

3.1 Thin Plate Excited by a Turbulent Boundary Layer

The goal of this portion of the experiment was to measure the response of a thin flat plate excited by a turbulent boundary layer. In the simplest case, the flow was a standard fully developed boundary layer but can be extended to different flow conditions as the intent is to study flow conditions which create spatially non-homogenous pressure fields. This setup was used to support the experimental data obtained for Chapters 4 and 5.

A schematic of the experimental setup is shown in Figures 3.1 and 3.2. A support structure was designed consisting of two S4x7.7 steel I-beams which were welded perpendicular to a 1.27 cm thick steel plate. This 1.27 cm thick steel plate was then bolted to an optical table such that the I-beams ran perpendicular to the surface of the table. Two interchangeable backpieces were then designed which could be attached to the I-beams to measure either surface pressures or structural vibration. The test structure was placed adjacent to a wind tunnel with a 30.5 cm by 30.5 cm exit such that the exit flow of the wind tunnel created a jet which was parallel to the surface of the test piece. The wind tunnel was capable of reaching speeds up to approximately 60 m/s, and the exit flow of the wind tunnel was tripped utilizing a sand trip roughly 43 cm upstream of the beginning of the test piece.

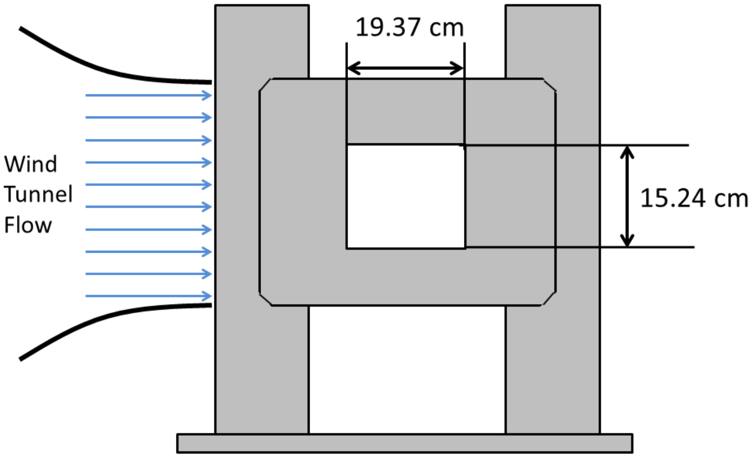

Figure 3.1. Front view of flat plate structural setup.

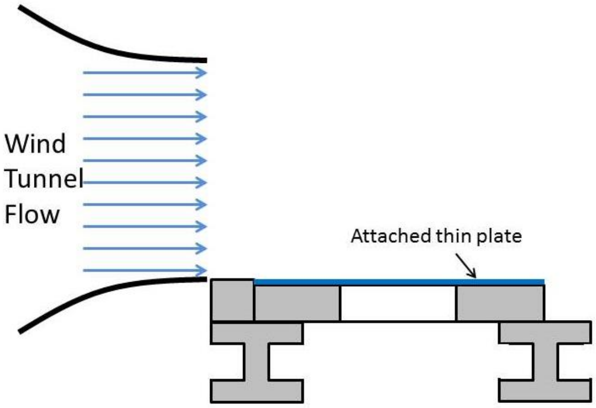

Figure 3.2. Top view of flat plate structural setup.

Using a 3-axis traverse, the boundary layer profile was measured at a flow speed of 30 m/s at the midpoint of the test setup, as shown in Figures 3.3 and 3.4. The boundary layer thickness at 30 m/s was found to be 20 mm. The resulting plots appear to be consistent with a fully developed canonical turbulent boundary layer.

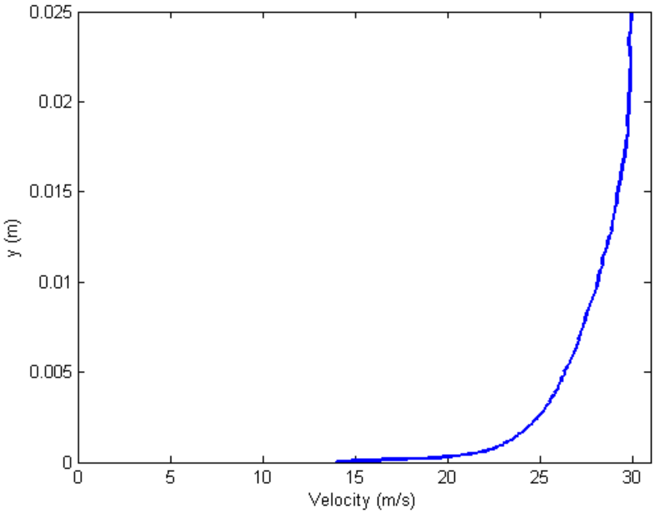

Figure 3.3. Measured boundary layer profile at 30 m/s.

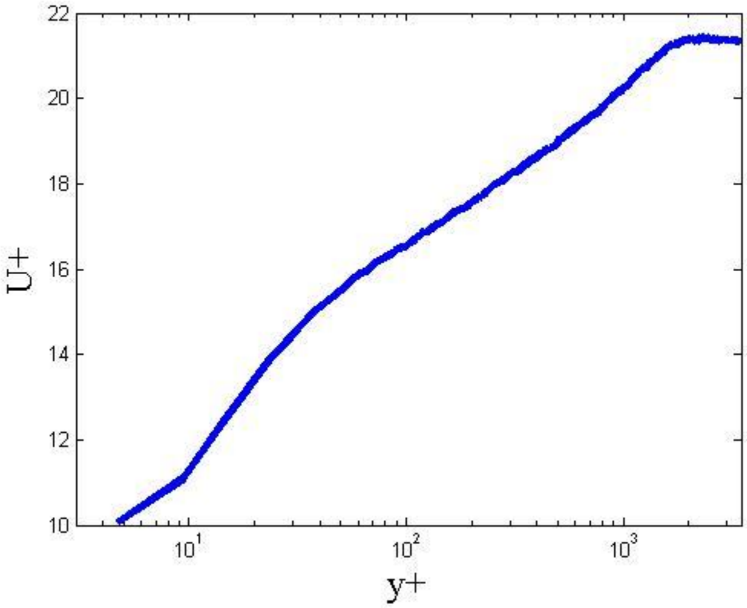

Figure 3.4. Measured boundary layer profile at 30 m/s normalized by inner scaling parameters.

3.1.1 Structural Setup

The first backpiece was designed to measure structural vibration. This backpiece consisted of a 34.3 cm by 30.5 cm by 2.54 cm thick piece of steel affixed to the support structure through ten countersunk bolts on both the left and right sides. A hole of size 19.37 cm in the streamwise direction and 15.24 cm in the spawnise direction was removed from the backpiece such that it was centered on the backpiece. The corners of this hole were milled to a 0.32 cm radius, while the corners were further milled 0.25 cm deep from the front side of the plate to have a radius of 0.16 inches.

The structural backpiece was used to examine both fluid-loaded and non-fluid-loaded vibration. For the non-fluid-loaded vibration, a 0.51 mm thick steel plate was affixed to this backpiece through use of the epoxy Vibra-tite 121 (comparable to Loctite

242). This epoxy cures under pressure, separates in heat, and forms an extremely stiff bond when cured. To affix the thin steel plate to the backpiece, the epoxy was spread evenly over the surface of the backpiece, the thin steel piece was placed ontop, and then thin plate was heavily weighted down to allow the epoxy to cure. This resulted in a setup that mimics the conditions of a 19.37 cm by 15.24 cm plate with clamped boundary conditions along all edges; measurements were performed to verify that the vibration of the backpiece was negligible in comparison to that of the thin steel plate. Figures 3.1 and 3.2 show front and top views of this setup, respectively. For this setup, the fluid loading factor was approximately β=0.14 at the first natural frequency of 112 Hz. This fluid loading factor was much less than 1 and thus fluid loading effects on this structure should be negligible.

When examining fluid-loaded vibration, a 0.051 mm thick piece of aluminum foil was affixed to the structural backpiece instead of the 0.51 mm thick steel plate. The foil was placed in homogeneous tension by attaching weights to the foil at equally spaced locations along the perimeter then adhering the foil to the surface of the structural backpiece with adhesives. Under the case of a canonical turbulent boundary layer excitation, the fluid loading factor was approximately β=7.76 at the first natural frequency of 60 Hz. This fluid loading factor was much greater than one, such that the structure is heavily fluid loaded.

Structural vibration data of the active region of the structural backpiece were taken using two simultaneous laser Doppler vibrometers (LDV). The Polytec OFV-503 Sensor Head was used to measure the vibration of a fixed point (from here on out known as the single point laser) while the Polytec PSV-400 Scanning Head scans a specified series of points (from here on out known as the scanning laser). The Polytec LDV's can measure vibrations up to a frequency of 80 kHz and can measure vibrations between 0.01 μm/s and 10 m/s; these ranges are more than sufficient for the structures of interest to this experiment. In order to promote stronger signal strength to the lasers, the 0.51 mm thick steel plate was coated with a thin layer of glass microspheres. These glass microspheres improve the laser's signal strength by promoting scattering of the laser from the surface. The microspheres are small and light enough to have negligible effects on the plate's vibration. The 0.051 mm thick aluminum foil did not require the use of glass microspheres to obtain sufficient signal strength.

The use of the two lasers does not allow for simultaneous vibration information of all points of the plate as would be the case with accelerometers, which adds a complication to the measurements. However, the simultaneous measurements of these two lasers allow for determination of the cross-spectral density of the vibration at various pairs of points across the structure. Chapter 4 details a method by which these two-point measurements and their corresponding cross-spectral densities can be used to decompose the vibration into a series of mode shapes as long as one of the scanned points remains unchanged.

3.1.2 Wall Pressure Measurement Setup

The second backpiece utilized was the surface pressure backpiece. This backpiece consisted of a series of pressure taps to measure surface pressure and was interchangeable with the structural backpiece. The pressure taps were fitted with wall-mounted Knowles microphones, model FG-23629-C36, with a 2.59 mm sensing diameter and a reported maximum frequency of 10 kHz. The microphones were placed at increments of 15.24 mm apart spanning a region greater than the bounds of the active vibration area for the structural backpiece. A schematic of the surface pressure backpiece is shown in Figure 3.5. The flow boundary conditions were identical for both the cases of the structural backpiece and the surface pressure backpiece. The purpose of the surface pressure backpiece was to determine the spatial-dependent wall pressure field which is exciting the active region of the structural backpiece.

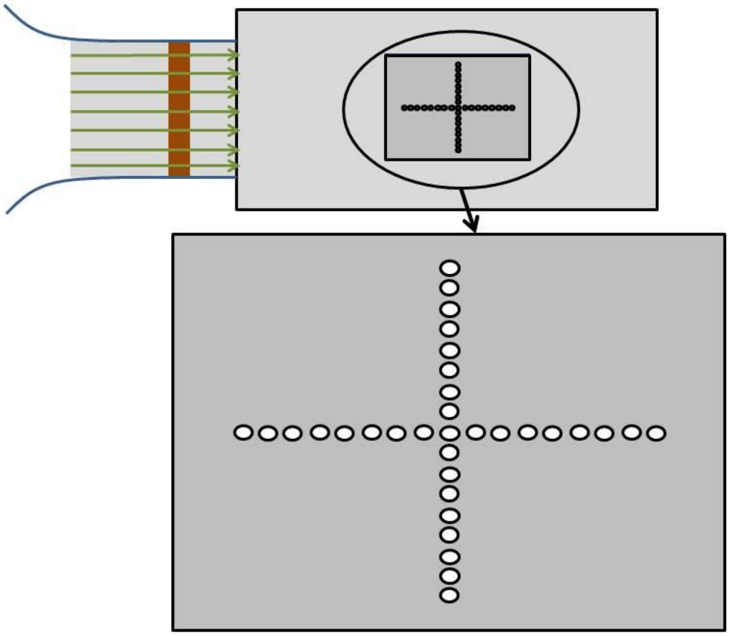

Figure 3.5. Schematic of surface pressure backpiece.

Figure 3.6 shows the auto-spectral density of the wall pressure for a microphone at the leading edge, trailing edge, and center of the active vibration region. All three of these measurements were taken along a streamwise line running along the center of the active vibration region. One should note very little streamwise variation of the wall pressure auto-spectral density, which shows that the flow is relatively spatially homogeneous. Figure 3.6 shows the auto-spectral density of the wall pressure at frequencies up to 10 kHz so that the reader can see at what frequencies the pressure spectra has reduced magnitudes. However, the structural analysis will only involve frequencies up to approximately 1 kHz. Over this range of frequencies, the amplitude of the unsteady surface pressure spectra was found to be essentially constant.

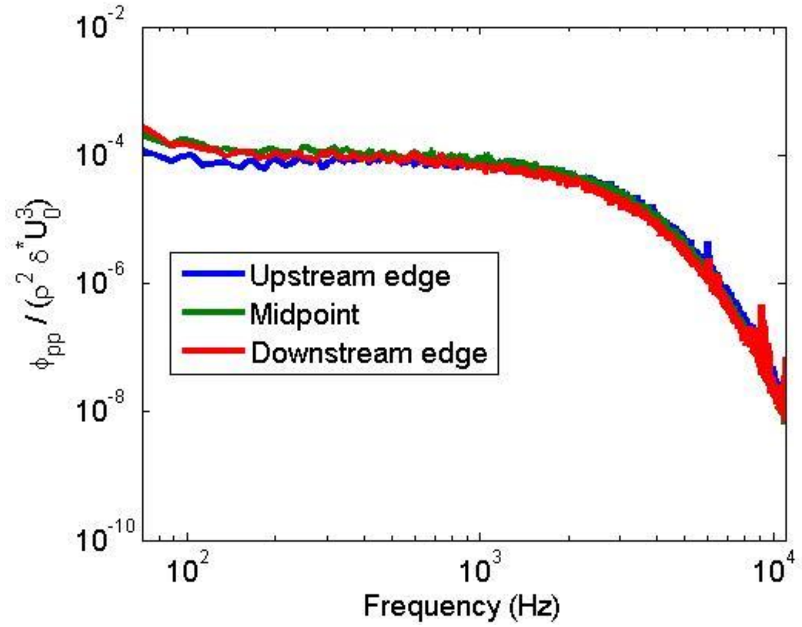

Figure 3.6. Measured wall pressure at three locations of the active vibration region.

As detailed in Chapter 2, prediction of the vibration of a structure requires knowledge of both the magnitude of the exciting wall pressure and its spatial characteristics. Figures 3.7 and 3.8 show the pressure spectra for various wave numbers in the streamwise and spanwise directions, respectively. The legend in this plot corresponds to $2\pi/k_xL$ for the streamwise plot and $2\pi/k_yW$ for the spanwise plot (i.e. the ratio of the wavelength of the wall pressure spectra to the length of the plate in the corresponding direction). Thus, for example, the legend entry of 3.9688 corresponds to the wall pressure at a spatial scale roughly corresponding to that of mode 4 of the plate. One will note little variation wall pressure spectra as a function of wavelength, with the exception of legend value of zero, which has a slightly higher magnitude than the other spectra.

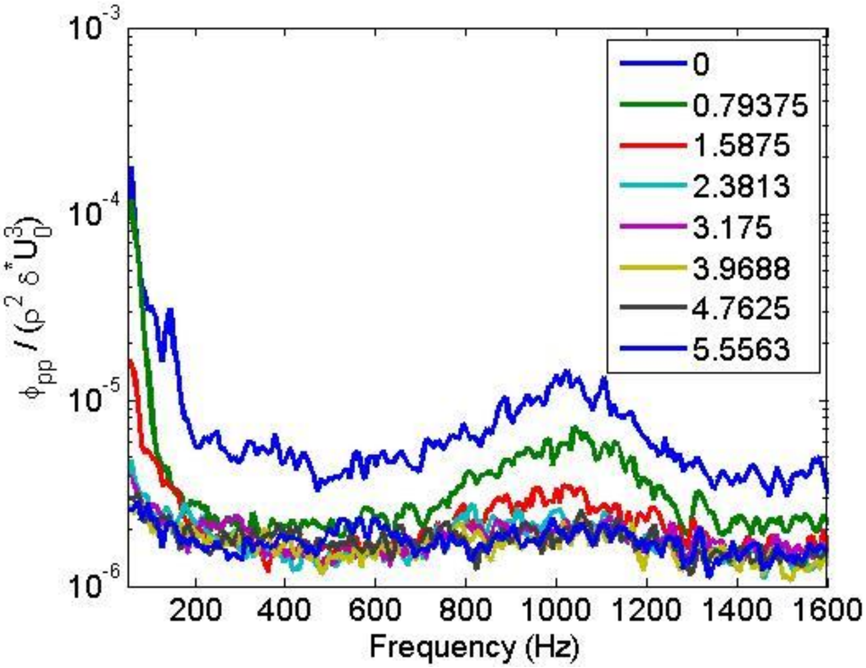

Figure 3.7. Wall pressure spectra for various wavelengths in the streamwise direction. Legend corresponds to $2\pi/k_xL$.

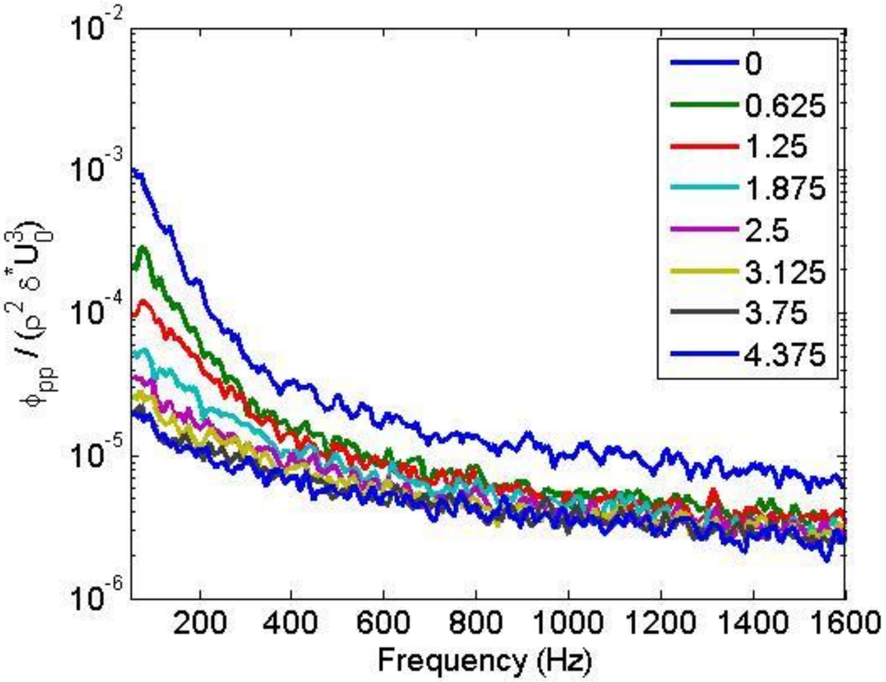

Figure 3.8. Wall pressure spectra for various wavelengths in the spanwise direction. Legend corresponds to $2\pi/k_yW$.

3.1.3 Generation of Spatially Nonhomogeneous Wall Pressure Fields

In order to generate spatially non-homogeneous wall pressure fields, a device called a splitter was attached to the flow side of the structure. The splitters were designed so that they would not make contact with the structure. Two splitters were used to create different spatial non-homogeneities of the wall pressure field. The "vertical splitter", intended to create a spanwise non-homogeneity in the wall pressure field, was composed of a wooden board aligned in the streamwise direction and a ramp on one side of this board which causes the flow field to be separated over the active region of the structural backpiece on that side of the wooden board. This created a blocked off region of flow spanning approximately 2/3 of the span of the plate. The wall pressure was experimentally determined to be at least one order of magnitude lower in all regions of the blocked off portion than in the unblocked portion. This created a pressure field with wall pressure magnitudes comparable to that of a step function in the spanwise direction, creating a strong spanwise non-homogeneity of the pressure field. Figure 3.9 shows a schematic of the vertical splitter, while Figure 3.10 shows a picture of the splitter in place in the setup.

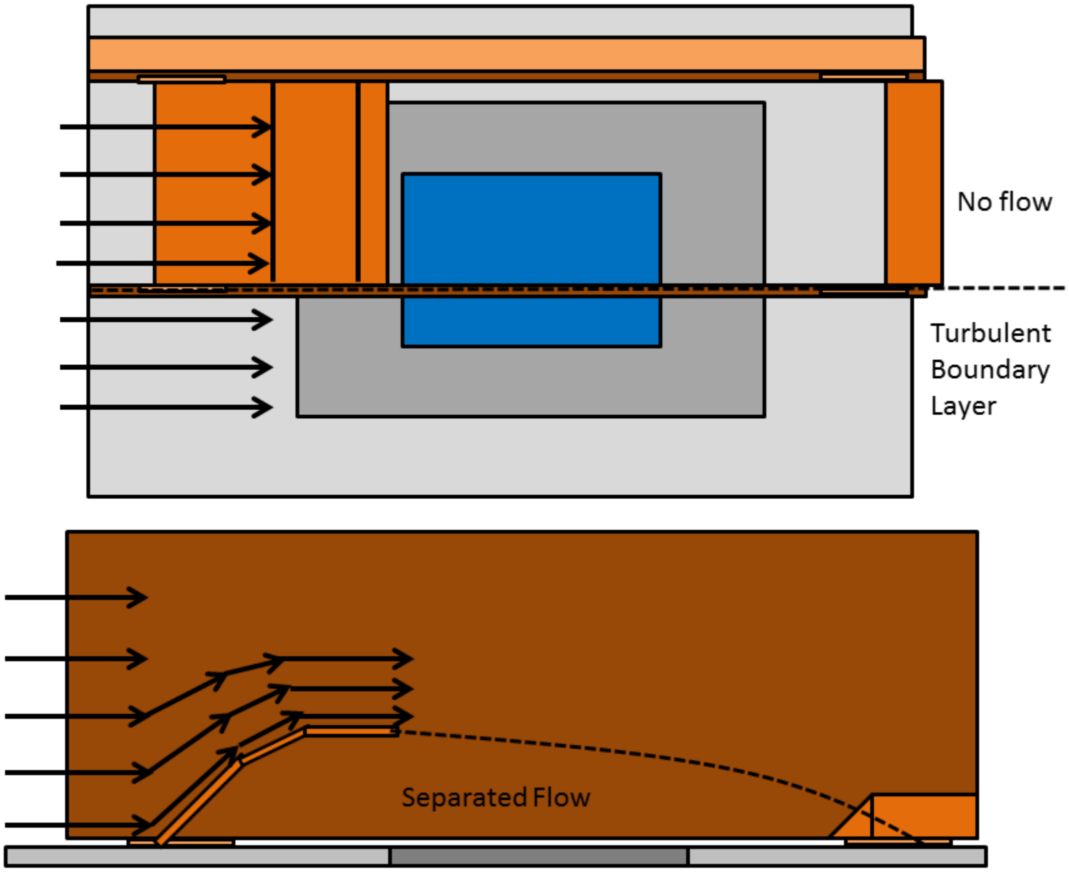

Figure 3.9. Schematic of vertical splitter.

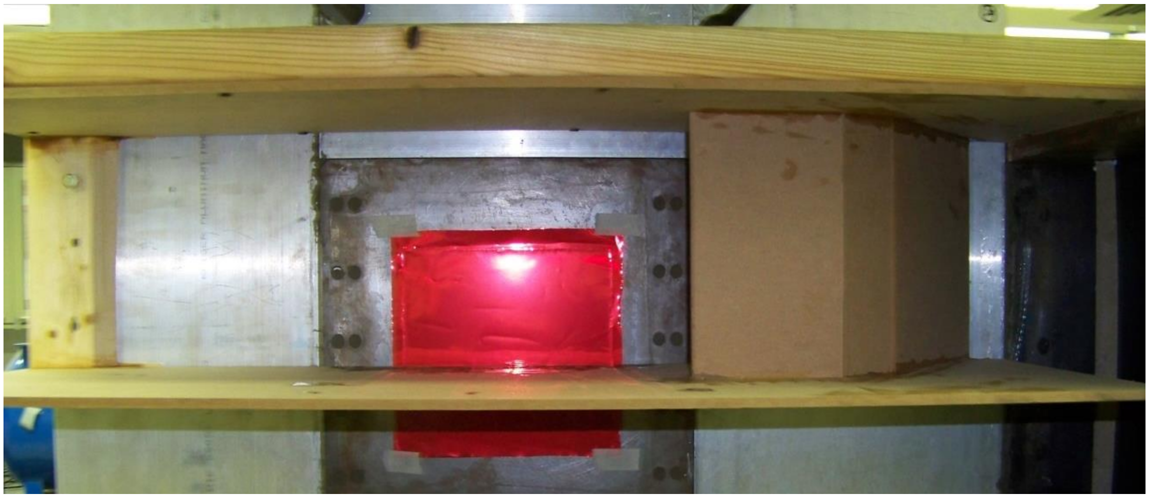

Figure 3.10. Picture of vertical splitter in place.

The second splitter was the “horizontal splitter”, which is primarily composed of a ramp placed to create a region of separated flow over approximately 2/3 of the structure on the downstream end. The purpose of the horizontal splitter was to create a streamwise non-homogeneity in the wall pressure field. A picture of this is shown in Figure 3.11.

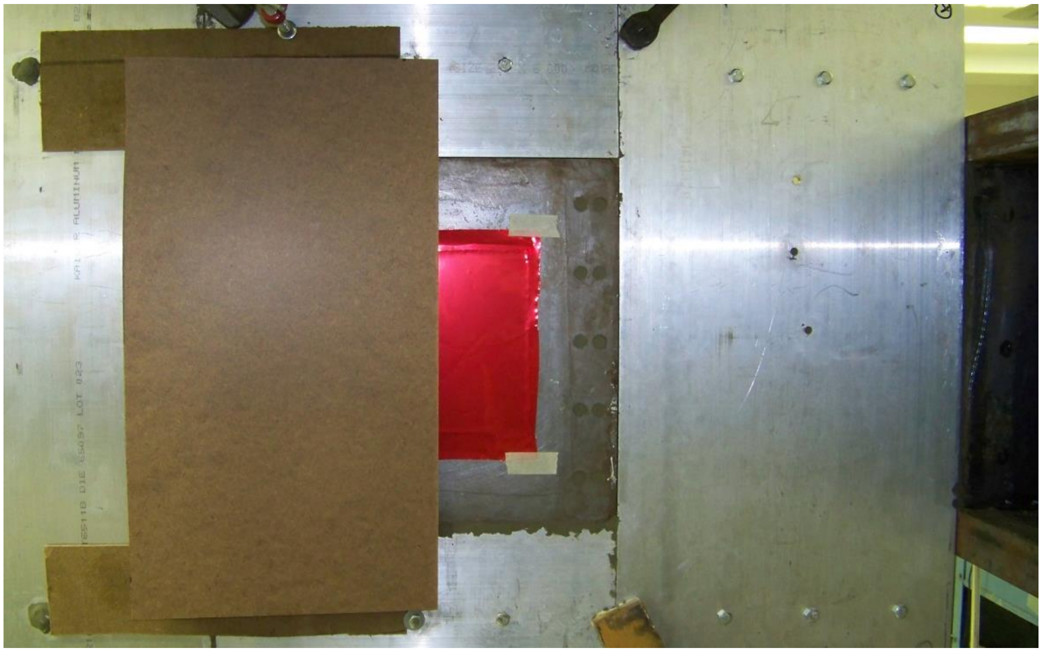

Figure 3.11. Picture of the vertical splitter.

3.2 Ducted Rotor Experiment

3.2.1 General setup

The ducted rotor experiment follows a similar setup to that previously used by Stevens [11]. The duct for the present experiment was machined from eight inch diameter PVC to an inner diameter of 206 mm and a wall thickness of 6.7 mm. The final duct was cut into pieces of varying length (usually approximately 20.3 cm) and was designed with a connection system so that pieces of the duct could be interchanged, the locations of important features of the duct altered, and the length of the duct altered.

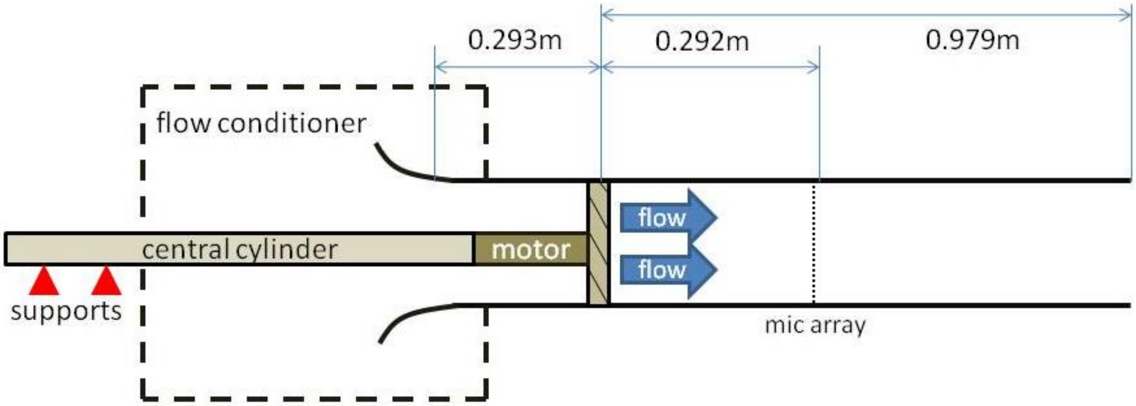

Figure 3.12. Schematic of ducted rotor experiment

The duct was supported in two different fashions. For acoustical experiments, the duct was mounted to a steel unistrut structure supported on a vibration isolation pad. This setup was placed within an anechoic chamber with a low frequency limit of 100 Hz. The unistrut was covered with split-seam pipe insulation to reduce acoustic scattering.

For structural experiments, the duct was mounted on a unistrut structure which was affixed to a heavy optical table with mounting taps at 2.54 cm intervals. Because the environment was not anechoic, foam wedges were placed at specific locations around the duct to minimize reflections within the room, particularly from the optical table which was located relatively close to the duct. This setup provided for a more stable foundation for the duct when attempting to measure vibration but limited the range of acoustical experiments that could be run. Figure 3.13 shows an image of the duct setup for structural experiments.

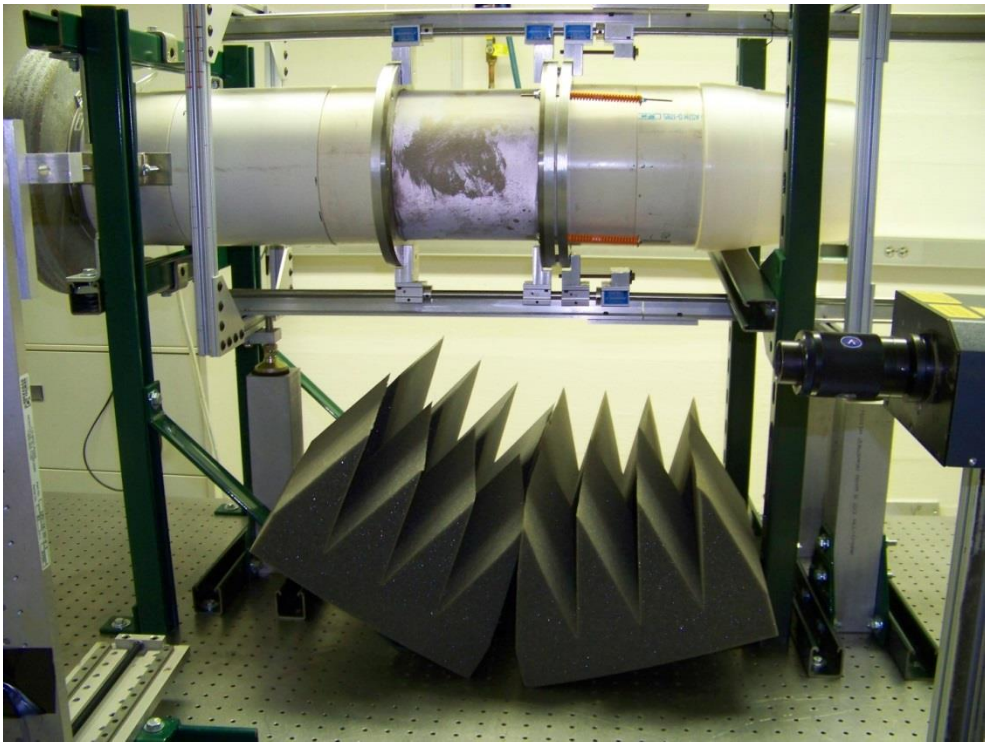

Figure 3.13. Picture of structural setup on the optical table of the duct experiment with nickel portion attached.

All further explanation of the duct setup should be assumed to apply to both the cases of the acoustic setup and the structural setup unless otherwise noted. A special rounded inlet was machined from particle board and designed to mate with the plastic duct sections in order to provide a smoother transition from the external flow to the internal duct flow, a picture of which is shown in Figure 3.14. The inlet flow was conditioned using a single thin layer of a "cheesecloth" type fabric stretched over a wire frame which surrounded the duct inlet and was particularly effective in reducing large-scale turbulent structures approaching the duct inlet.

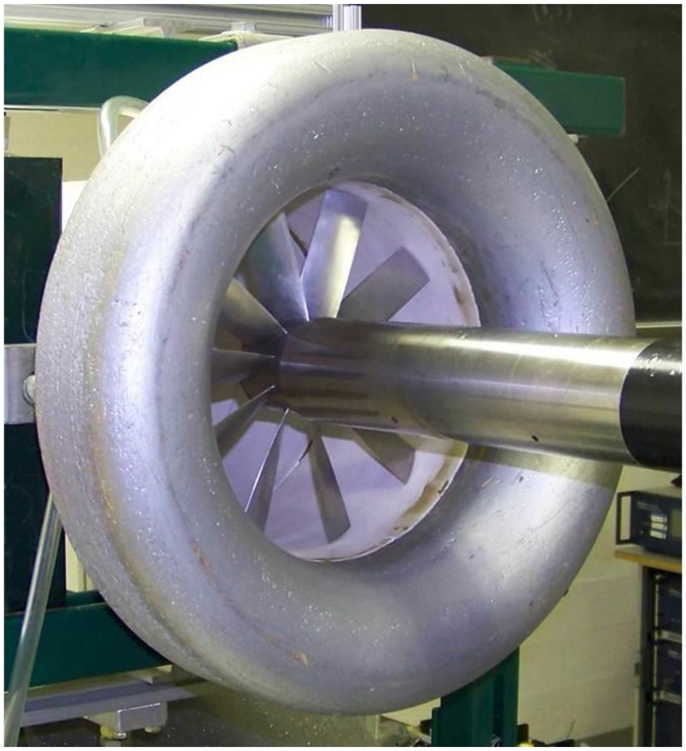

Figure 3.14. Picture of rounded duct inlet and rotor.

In order to support the rotor within the duct, a stainless steel cylinder running along the central axis of the duct was cantilevered from two clamped supports several diameters upstream of the inlet. This cylinder contained a compact servo motor to drive the rotor at the desired speed and was supported by a unistrut structure separate from that which supported the duct.

The rotor was a ten-bladed rotor as previously used by Sevik [48], with a diameter of 0.203 m, a constant blade chord of 0.025 m, and a maximum thickness of 2.4 mm. The blades are straight blades incorporating twist only, and are thin air foils with rounded leading and trailing edges. The rotor operated with a tip clearance of 5% blade chord. A pictures of this rotor within the duct can be seen in Figure 3.14. Table 3.1 shows a more comprehensive list of relevant parameters of the rotor

TABLE 3.1

BASIC DIMENSIONS OF THE DUCTED ROTOR EXPERIMENT

Parameter	Symbol	Value
Duct Diameter	D	0.206 m
Length	L	Usually 1.272 m, but variable
Rotor Tip Radius	R_{tip}	0.1016 m
Rotor Hub Radius	$R_{tip}/4$	0.0254 m
Rotor Location	L_1	0.293 m
Number of Blades	B	10
Chord	C	0.254 m
Tip Gap	-	0.05C
Rotor Rotation Rate	RPM	2500 → 5000
Rotor Tip Speed	V_{tip}	26.6 → 53.2 m/s
Mean Axial Fluid Velocity in Duct	$\bar{U}$	4.0 → 22.4 m/s
Tip Relative Mach Number	M_{tip}	<0.16
Speed of Sound	c_0	343 m/s

3.2.2 Measurement Sections

The overall duct experiment was designed with interchangeability in mind. The location of the rotor was variable, and because of the interchangeable PVC pieces that compose the duct, the measurement sections (i.e. the microphone array and the nickel shell) could be moved to almost any location. It was decided to place the rotor 0.293 m downstream of the inlet of the duct.

Experiments were performed by replacing one of the interchangeable PVC duct pieces with a "measurement section", which was either a section containing a microphone array for wall pressure measurements or a thin nickel duct for structural vibration measurements. These duct sections are analogous to the wall pressure and structural backpieces outlined in Section 3.1. Axially, the center of the interchangeable section was located 0.292 m downstream of the rotor. This corresponds to the axial center of the nickel shell and the location of the circumferential microphone array, pending the particular experiment being run.

The wall pressure measurement section was 8 inches in length and consisted of a series of pressure taps along the wall to allow for surface mounted microphones. The section contained 9 taps at 1.9 cm intervals along the axis and 32 taps equally spaced along the circumference (one of these taps is shared by both directions). A picture of this is shown in Figure 3.15. The circumferential array of microphone taps were fitted with Knowles microphones, model FG-23629-C36, with a 2.59 mm sensing diameter and a reported maximum frequency of 10 kHz (though testing has indicated that with calibration they are effective at frequencies of at least 40 kHz). Data was taken at 51 rotor speeds from 2500 rpm to 5000 rpm at 50 rpm increments with 16 ensembles per speed. For each ensemble, approximately 1.6 seconds of data was simultaneously acquired from each microphone at a sampling rate of 40 kHz.

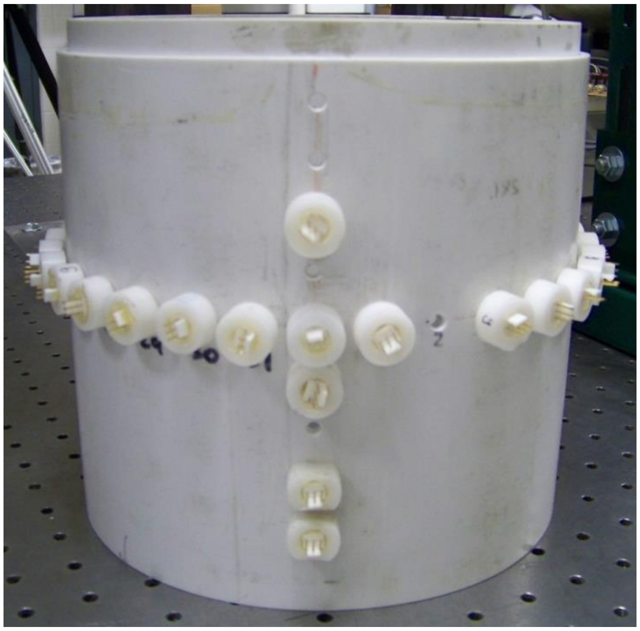

Figure 3.15. Picture of the ducted microphone array with several microphones removed.

For structural experiments, the test section was replaced with a nickel duct. The nickel duct piece was a 20.3 cm long nickel shell with a thickness of roughly 68 μm. The nickel shell was thin enough that when excited by an air flow within the duct that the nickel shell vibrated sufficiently for the scanning and reference laser to be able to measure the vibration. The duct was circumferentially symmetric, containing no seam. The first natural frequency occurs at roughly 267 Hz. This corresponds to a fluid loading factor of 1.05, which indicates that the nickel duct was lightly fluid loaded. A spring-tension mechanism was implemented to subject the shell to a specific, uniform tension in the axial direction. When utilizing the nickel duct, a conical nozzle 20.3 cm in length with ends of 17.8 cm and 20.3 cm inner diameter was attached to the exit of the duct. This created a slight backpressure within the duct, creating circumferential tension in the nickel shell. Figure 3.16 shows a picture of the nickel shell and its support structure.

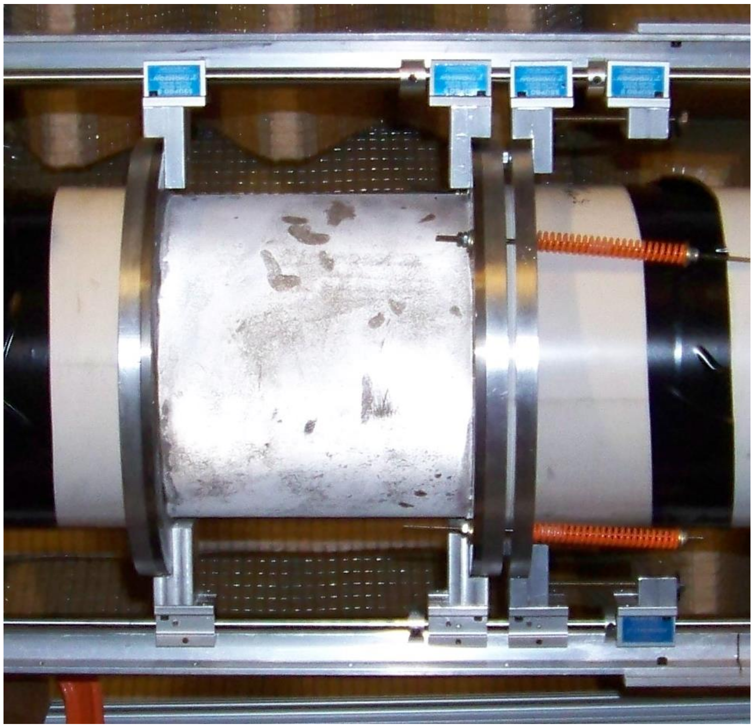

Figure 3.16. Nickel shell and its support structure.

Structural vibration data was taken using the scanning and reference laser, similar to the case outlined in Section 3.1. The nickel shell was coated with a thin layer of class microspheres in order to promote LDV signal strength, similar to the case of the steel plate noted in Section 3.1. Structural vibration data was taken in an axial and circumferential sweep with a fixed reference location. Utilizing a mirror, a circumferential sweep of approximately 270° was obtained.

CHAPTER 4

PREDICTION AND EXPERIMENTAL DETERMINATION OF THE MODAL VIBRATION SPECTRA OF A THIN ELASTIC PLATE

One must first validate that the structural vibration can be measured under the most basic conditions in order to measure structural vibration under the effects of non-homogeneous forcing and fluid-loading. Two models are required to predict the structural vibration of a thin plate: a model of the wall pressure spectra and a model of the structural vibration transfer function. In this chapter, experimental wall pressure data, the Corcos wall pressure model, and the structural transfer function as outlined by Blake [1] and Leissa [17] will be combined in order to predict the structural vibration of each mode. Structural vibration data were taken using the experimental setup detailed in Section 3.1. The two-point information of vibration was decomposed using a procedure termed magnitude-phase identification (MPI), which will be derived in this chapter. MPI was validated by comparing the auto-spectral density of vibration for a single mode determined through MPI to the values predicted by vibration theory.

4.1 Theoretical Transfer Function for a Structural Vibration

This analysis assumes statistically stationary structural vibration which is induced solely by a statistically stationary, spatially homogeneous, low Mach number flow over the surface of the structure. The analysis will be restricted to thin structures with small magnitudes of motion, where the motion of the structure does not alter the flow field. Blake [1] details a method by which the vibration of such a structure can be predicted through modal analysis. While the proof will not be detailed here, it assumes that the displacement of the structure can be expressed in the form

$$\xi = \sum_{m=1}^{\infty}\sum_{n=1}^{\infty} a_{mn}\psi_m^{(1)}(y_1)\psi_n^{(2)}(y_2)g_{mn}(t) = \sum_{m=1}^{\infty}\sum_{n=1}^{\infty} a_{mn}\psi_{mn}(\vec{y})g_{mn}(t)\ , \quad (4.1)$$

where ξ is the structural displacement and a_{mn} is the coefficient which represents the amplitude of mode <*m*,*n*>. $\psi_{mn}(\boldsymbol{y})$ is the two-dimensional eigenfunction (also known as the mode shape) for mode <*m*,*n*>, and $g_{mn}(t)$ is a function which determines the time-dependence of the mode's displacement. For analysis related to rectangular structures, *m* will represent the streamwise mode number and *n* will represent the spanwise mode number, though such a distinction is not a requirement of the analysis. Furthermore, eigenfunctions in this documents will use the same normalization used by Blake[1], which is defined as

$$\iint_{A_{plate}} \psi_{mn}(\boldsymbol{y})d\boldsymbol{y} = A_{plate}\delta_{mn} \qquad , \qquad (4.2)$$

where A_{plate} is the surface area of one side of the structure and δ_{mn} is the standard Dirac delta function.

The analysis assumes that the structure is excited by a wall pressure field $p(\boldsymbol{y},t)$, defined for all points in space over the area of the structure and for all points in time. For each mode <m,n>, the projected pressure is the result of projecting the wall pressure field at a fixed moment in time onto the corresponding mode shape. Assuming the mode shape normalization defined in Equation (4.2), the projected pressure is

$$P_{mn}(t) = \frac{1}{A_{plate}} \iint_{A_{plate}} p(\boldsymbol{y},t)\psi_{mn}(\boldsymbol{y})d\boldsymbol{y} \qquad . \qquad (4.3)$$

Then, the transfer function for the vibration of the structure can be written as

$$\Phi_{v,mn} = \frac{\omega}{m_s{}^2[(\omega_{mn}{}^2-\omega^2)^2+(\eta_{mn}\omega_{mn}\omega)^2]}\Phi_{p,mn} \qquad . \qquad (4.4)$$

Here, $\Phi_{v,mn}$ is the auto-spectral density of the vibration for mode <m,n>, $\Phi_{p,mn}$ is the auto-spectral density of the projected pressure defined in Equation (4.3), ω is the frequency of vibration, ω_{mn} is the natural frequency of mode <m,n>, m_s is the mass per unit area of the structure, and η_{mn} is the damping ratio for mode <m,n>.

4.2 Derivation of Magnitude-Phase Identification

Experimental validation using Equation (4.4) requires experimental determination of the frequency-dependent vibration of each mode <m,n>. A modal decomposition is required to convert vibration data from each point into modal data, but such modal decomposition requires the relative phase of vibration between each point measured to be known. In the experimental setup detailed in Section 3, vibration information is only acquired for two points at a time rather than simultaneously across the entire structure. Thus, a method must be developed to determine the phase information of all points using only two-point measurements. This method, which will be derived in this section, will be called Magnitude-Phase Identification (MPI).

The cross-spectral density of a function is defined as

$$P_{v_1v_2}(\omega) = lim_{T\to\infty}\frac{1}{2T}\int_{-T}^{T} E_t[v_1(t)v_2{}^*(t+\tau)]\, e^{-i\omega\tau}d\tau \quad , \tag{4.5}$$

where E_t is an operator that indicates the expected value over time; for large values of time this is simply the mean. τ represents a time difference between the two signals and is primarily used as a dummy variable of integration. While in practice v_1 and v_2 are often measurements of the same variable (such as velocity) at different locations, Equation (4.5) is valid for any signals v_1 and v_2.

Next, assume that v_1 and v_2 can be expressed as a Fourier series such that

$$v_1(\boldsymbol{t}) = \sum_m V_1\left(\frac{2\pi m}{T}\right) e^{-i2\pi m\frac{t}{T}} \tag{4.6a}$$

and

$$v_2(\boldsymbol{t}) = \sum_n V_2\left(\frac{2\pi n}{T}\right) e^{-i2\pi n\frac{t}{T}} \quad , \tag{4.6b}$$

where T is the time over which v_1 and v_2 are defined (or measured). v_1 will be known as the reference signal. $V_1(2\pi m/T)$ and $V_2(2\pi n/T)$ are the Fourier series coefficients and are complex values. These coefficients are generally written as being dependent on m and n, but they are written here as being dependent on $2\pi m/T$ and $2\pi n/T$ without loss of generality in order to simplify later steps in the derivation. For a stationary system the reference phase of $v_1(t)$ and $v_2(t)$ is arbitrary; only the *difference* in phase between v_1 and *v2* can be uniquely defined. Choose v_1 to be defined such that it has a reference phase of zero, and thus the phase of v_2 is defined relative to the phase of v_1. Substitution of Equation (4.6a) and (4.6b) into Equation (4.5) yields

$$P_{v_1 v_2}(\omega) = lim_{T\to\infty} \frac{1}{2T} \int_{-T}^{T} E_t \left[\left(\sum_m V_1 \left(\frac{2\pi m}{T} \right) e^{-i2\pi m \frac{t}{T}} \right) \left(\sum_n V_2 \left(\frac{2\pi n}{T} \right) e^{-i2\pi n \frac{(t+\tau)}{T}} \right)^* \right] e^{-i\omega\tau} d\tau \quad ,$$

or

$$P_{v_1 v_2}(\omega) = lim_{T\to\infty} \frac{1}{2T} \int_{-T}^{T} E_t \left[\left(\sum_m V_1 \left(\frac{2\pi m}{T} \right) e^{-i2\pi m \frac{t}{T}} \right) \left(\sum_n V^*{}_2 \left(\frac{2\pi n}{T} \right) e^{i2\pi n \frac{(t+\tau)}{T}} \right) \right] e^{-i\omega\tau} d\tau \quad .$$

(4.7)

The orthogonality of the sine and cosine ensures that the value within the integral will only be non-zero for values of $m=n$, resulting in

$$P_{v_1 v_2}(\omega) = lim_{T\to\infty} \frac{1}{2T} \int_{-T}^{T} E_t \left[\left(\sum_n V_1 \left(\frac{2\pi n}{T} \right) e^{-i2\pi n \frac{t}{T}} V^*{}_2 \left(\frac{2\pi n}{T} \right) e^{i2\pi n \frac{(t+\tau)}{T}} \right) \right] e^{-i\omega\tau} d\tau \quad , \quad \text{or}$$

$$P_{v_1 v_2}(\omega) = lim_{T\to\infty} \frac{1}{2T} \int_{-T}^{T} E_t \left[\left(\sum_n V_1 \left(\frac{2\pi n}{T} \right) V^*{}_2 \left(\frac{2\pi n}{T} \right) e^{i2\pi n \frac{\tau}{T}} \right) \right] e^{-i\omega\tau} d\tau \quad . \qquad (4.8)$$

As τ is not a function of n, the integral of the summation can be changed into the summation of the integrals, yielding

$$P_{v_1 v_2}(\omega) = \sum_n \left(lim_{T\to\infty} \frac{1}{2T} \int_{-T}^{T} E_t \left[V_1 \left(\frac{2\pi n}{T} \right) V^*{}_2 \left(\frac{2\pi n}{T} \right) e^{i2\pi n \frac{\tau}{T}} e^{-i\omega\tau} \right] d\tau \right) \quad . \qquad (4.9)$$

Due to the orthogonality of the sine and cosine functions, the integration of Equation (4.9) is only non-zero for $2\pi n/T = \omega$. Thus, Equation (4.9) simplifies to

$$P_{v_1 v_2}(\omega) = V_1(\omega) V^*{}_2(\omega) = |V_1(\omega)||V_2(\omega)| e^{-i\phi_v(\omega)} \quad , \qquad (4.10)$$

where ϕ_v is the phase of v_2 relative to v_1 at the given frequency. The derivation of (4.10) never specified that v_1 and v_2 were unique signals, so if one applies this result for $v_1=v_2$, then Equation (4.10) becomes

$$P_{v_1 v_1}(\omega) = V_1(\omega)V^*{}_1(\omega) = |V_1(\omega)||V_1(\omega)|e^{-i0} = |V_1(\omega)|^2 \qquad (4.11)$$

Dividing (4.10) by (4.11) yields

$$|V_2(\omega)|e^{-i\emptyset_v(\omega)} = \frac{P_{v_1 v_2}(\omega)}{\sqrt{P_{v_1 v_1}(\omega)}} \qquad . \qquad (4.12)$$

Equation (4.12) demonstrates how one can obtain magnitude and phase information everywhere along a structure using only two-point measurements. Equation (4.12) is the final form of the MPI. The reference signal v_1 need not be measured at any specific location in general. However, the primary requirement for use of MPI is that v_1 and v_2 must be coherent. The phase difference ϕ_v is undefined for components of v_1 and v_2 which are incoherent, and thus, any incoherent portions of the two signals will be removed through use of MPI. In the experimental setup shown in Section 2, the coherence of the structure was extremely high, allowing for use of the MPI.

The coherence requirement of the MPI has several secondary effects. First, the coherence between a point along a node line and any other point of a structure will be undefined because the node line point is not vibrating. Thus, while in general the reference location can be anywhere, placing the reference signal along a node line of a mode will cause all information related to that mode to be removed when the MPI is applied. This holds true even if v_2 is not located on a node line. Second, random noise in the measurement data tends to be removed through use of MPI because truly random signals are inherently incoherent; this causes the MPI to act as a type of noise filter. Finally, v_1 and v_2 need not both be vibration signals, they need only be coherent. For example, MPI would function even if v_1 were a vibration signal and v_2 were a pressure signal as long as the two signals have a large coherence.

4.3 Modal Decomposition

The MPI provides information on the magnitude and relative phase of the vibration of all locations scanned on the structure. To compare to predictions in Equation (4.4), the vibration must be calculated for each mode. If the modes of vibration were sines and cosines, this would usually be called a Fourier decomposition, but because the modes are not restricted to sines and cosines, the more generic term "modal decomposition" is used. Two methods of performing the modal decomposition will be presented: minimization of error and projection. While the methods are similar, each contains different benefits and flaws, which is why both methods will be examined.

4.3.1 Modal Decomposition Through Minimization of Error

The minimization of error method of modal decomposition utilizes linear algebra for non-square matrices. The analysis begins by stating that the vibration of a single frequency can be expressed as

$$\boldsymbol{\Psi}_{pxb}\boldsymbol{M}_{bx1} = \boldsymbol{V}_{px1} \quad . \qquad (4.13)$$

Here, p equals the number of points scanned on the structure, and b equals the number of modes being utilized in the decomposition. $\boldsymbol{\Psi}_{pxb}$ is a matrix composed of the mode shapes of the structure, where each column is equal to the values of a single mode shape at each point scanned on the structure. $\boldsymbol{M}_{bx1}$ represents the magnitude of the vibration for each mode at that frequency; each index of this array equals the square root of $\Phi_{v,mn}$ for b corresponding to mode $<m,n>$. $\mathbf{V}_{px1}$ is the real component of the MPI at this frequency and represents the structure's vibration at this frequency. $\boldsymbol{\Psi}_{pxb}$ is not a square matrix; rather, $p>b$, meaning that there are more scanned points than modes present in the decomposition. Thus, Equation (4.13) in general cannot be solved exactly. Rather, the system can only be solved for minimum error.

When minimizing the error, a weighting function can be used to cause the error of certain points to contribute more or less than the error of other points. This causes Equation (4.13) to take the form

$$\boldsymbol{W}_{pxp}\boldsymbol{\Psi}_{pxb}\boldsymbol{M}_{bx1} = \boldsymbol{W}_{pxp}\boldsymbol{V}_{px1} \quad , \qquad (4.14)$$

where $\boldsymbol{W}_{pxp}$ is the weighting matrix. For this analysis, $\boldsymbol{W}_{pxp}$ was set such that $\boldsymbol{W}_{pxp} = \boldsymbol{I}_{pxp} |\boldsymbol{V}_{px1}|$, where $\boldsymbol{I}_{pxp}$ is the identity matrix and $|\boldsymbol{V}_{px1}|$ has elements equal to the absolute value of the elements of $\boldsymbol{V}_{px1}$. This causes the minimization of error to be more heavily weighted towards points with relatively large magnitudes of vibration and weighted against points of small vibration, such as those along nodal lines. This is advantageous as points of small vibration tend to be more susceptible to noise. Such a weighting scheme was found to reduce noise in the vibration spectra which resulted from the modal decomposition. While other forms of $\boldsymbol{W}_{pxp}$ could produce similar results, this scheme provides a simple method for creating a weighting matrix with large values at the points of greatest vibration without prior knowledge of the vibration of the structure.

Equation (4.14) can be solved by using the method of ordinary least squares, which results in

$$\left(\boldsymbol{W}_{pxp}\boldsymbol{\Psi}_{pxb}\right)^T\boldsymbol{W}_{pxp}\boldsymbol{\Psi}_{pxb}\sqrt{\boldsymbol{\Phi}_{v,mn}} = \left(\boldsymbol{W}_{pxp}\boldsymbol{\Psi}_{pxb}\right)^T\boldsymbol{W}_{pxp}\boldsymbol{V}_{px1} \quad . \tag{4.15}$$

Equation (4.15) contains square matrices on either side of the equation and thus is solvable through standard linear algebra techniques. The solution obtained from this was termed the minimization of error method for modal decomposition.

4.3.2 Modal Decomposition Through Modal Projection

The second method of modal decomposition used in this thesis was the projection method. Based on Equation (4.1), start by assuming that the vibration of all points at a single frequency can be written as

$$\boldsymbol{V} = \sum_b M_b \psi_b \quad , \tag{4.16}$$

where $\boldsymbol{V}$ is a vector with elements equal to the vibration at each point, b is an index representing each mode utilized in the decomposition, ψ_b is the mode shape for mode b, and M_b is the magnitude of the vibration for mode b. Specifically, for a fixed frequency, $\boldsymbol{V}$ is the vector of the real components of the MPI at each point, and M_b is equal to the square root of $\Phi_{v,mn}$ for b corresponding to mode $<m,n>$. Using the orthogonality condition for the eigenfunctions, Equation (4.16) can be recast as

$$\iint_{A_{plate}} \psi_b \boldsymbol{V} dA = \iint_{A_{plate}} M_b \psi_b \psi_b dA \qquad , \qquad (4.17)$$

Where the integration is carried over the surface area of the plate A_{plate}.

Using the normalization condition presented in Equation (4.2), Equation (4.17) becomes

$$\sqrt{\Phi(f)_{v,mn}} = \frac{1}{A_{plate}} \iint_{A_{plate}} \psi_{mn} \boldsymbol{V}(f) dA \qquad . \qquad (4.18)$$

Assuming that the scanned points are equally spaced, then the integration can be more easily discretized by recognizing that $dA_{discretized} = A_{plate}/p$, where p is the number of points scanned, because each discrete area block has an equal area. This leads to the final form of the discretized projection,

$$\sqrt{\Phi(f)_{v,mn}} = \frac{1}{p} \boldsymbol{\Psi}_{mnxp} \boldsymbol{V}_{\mathrm{px1}}(f) \qquad , \qquad (4.19)$$

where Ψ_{mnxp} is a matrix of the mode shapes, with columns corresponding to the values of a single mode shape at each point. Equation (4.19) was termed the projection method of modal decomposition.

4.4 Experimental Determination of the Wall Pressure Spectra

Calculation of Equation (4.4) requires knowledge of $\Phi_{p,mn}$, the projection of the wall pressure spectra onto the eigenfunction of mode $<m,n>$. Equation (4.3) can be directly used to calculate $\Phi_{p,mn}$ if simultaneous wall pressure information is known at all locations of the plate. As outlined in Chapter 3, experimental information was only acquired in the streamwise or spawnise direction, but not both simultaneously. Thus, the wall pressure projection must be calculated in the wave number domain. Blake [1] details that the projected wall pressure spectra can be calculated by

$$\Phi_{p,mn} = \frac{1}{A_{plate}{}^{2}} \iint_{-\infty}^{+\infty} \Phi_p(\boldsymbol{k},\omega)|S_{mn}(\boldsymbol{k})|^2 d\boldsymbol{k} \qquad , \qquad (4.20)$$

where $S_{mn}(\boldsymbol{k})$ is the shape function for mode <m,n>, defined as

$$S_{mn}(\boldsymbol{k}) = \iint_{A_{plate}} e^{-i\boldsymbol{k}\cdot\boldsymbol{y}} \psi_{mn}(\boldsymbol{y}) d\boldsymbol{y} \qquad . \qquad (4.21)$$

The shape function represents the degree to which a wave number projects onto the eigenfunction for mode <m,n>.

One of the simplest models for the spatial characteristics of the wall pressure of a turbulent boundary layer is the Corcos model. In the wavenumber domain, the Corcos model of wall pressure takes the form [36]

$$\Phi_p(k_x, k_y, \omega) = \Phi_{pp}(\omega) g(k_x, \omega) h(k_y, \omega) \qquad . \qquad (4.22)$$

Here, $\Phi_{pp}(\omega)$ is the auto-spectral density of the wall pressure. Because the basic Corcos model assumes a spatially homogeneous wall pressure field, this is not a function of position. This assumption was shown to be valid in Figure 3.6 for the experimental setup outlined in Chapter 3, where the auto-spectral density of the wall pressure does not change appreciably with streamwise position. $g(k_x,\omega)$ and $h(k_y,\omega)$ are functions representing the streamwise and spanwise spatial characteristics of the wall pressure, respectively.

For wall pressures obtained along a line of fixed spanwise location (i.e. a streamwise array), the Corcos model can be expressed as

$$\Phi_{p,streamwise}(k_x,\omega) = \Phi_{pp}(\omega)g(k_x,\omega) \quad , \tag{4.23}$$

and a spanwise array can be expressed as

$$\Phi_{p,spanwise}\left(k_y,\omega\right) = \Phi_{pp}(\omega)h\left(k_y,\omega\right) \quad . \tag{4.24}$$

Direct substitution of these equations into Equation (4.22) yields

$$\Phi_p\left(k_x,k_y,\omega\right) = \frac{\Phi_{p,streamwise}(k_x,\omega)\Phi_{p,spanwise}\left(k_y,\omega\right)}{\Phi_{pp}(\omega)} \quad . \tag{4.25}$$

All values on the right side of Equation (4.25) are directly determinable from the experimental data obtained in Chapter 3. $\Phi_{p,streamwise}(k_x,\omega)$ and $\Phi_{p,spanwise}(k_x,\omega)$ correspond to Figures 3.7 and 3.8, respectively.

4.5 Determinations of the Mode Shapes and Natural Frequencies

Calculation of Equation (4.4) requires decomposing the structural vibration into the vibration of each mode and projecting the pressure field onto the mode shapes. The methods of performing these calculations were detailed in Sections 4.3 and 4.4. Both require knowledge of the mode shapes for each mode of interest. Also, Equation (4.4) requires the natural frequency of each mode of interest as an input. The section will detail how to experimentally determine the mode shapes and natural frequencies through use of MPI.

4.5.1 Theoretical Mode Shapes for a Non-Fluid-Loaded Plate

While experimental mode shapes will be used in the calculations, it was advantageous to compare the experimentally-derived mode shapes to theoretical mode shapes to determine if the experimentally-derived mode shapes appear reasonable. Leissa [17] derives expressions for the theoretical mode shapes and natural frequencies of a clamped rectangular plate. A detailed summary of the calculation of these quantities requires more time than is worth presenting in this paper; however, the results will be summarized here. The theoretical natural frequencies of various modes are given in Table 4.1.

TABLE 4.1

PREDICTED NATURAL FREQUENCIES OF EXPERIMENTAL PLATE

		Streamwise mode number (*m*)				
		1	**2**	**3**	**4**	**5**
Spanwise mode number (*n*)	**1**	151.7	273.2	462.3	719.3	1042.3
	2	362.8	470	649.5	900.2	1219.6
	3	676	779.9	952	1195.2	1508.5
	4	1094.2	1197.3	1365.7	1603.4	1910.7
	5	1616.9	1720	1886.8	2121.1	2423.9

Because the mode shapes for a rectangular clamped plate are separable, it is often simpler to plot the one-dimensional eigenfunctions for a single direction, corresponding to $\psi_m^{(1)}$ or $\psi_n^{(2)}$ in Equation (2.5); Figure 4.1 shows such a plot. The eigenfunctions here have not been normalized as per Equation (2.6) because Equation (2.6) is only defined for the full two-dimensional eigenfunction. Note that the mode shapes look increasingly similar to pure sine waves (the mode shape for a simply supported plate or a foil) for increasing mode, though due to the clamped condition the mode shapes can never truly be pure sine waves.

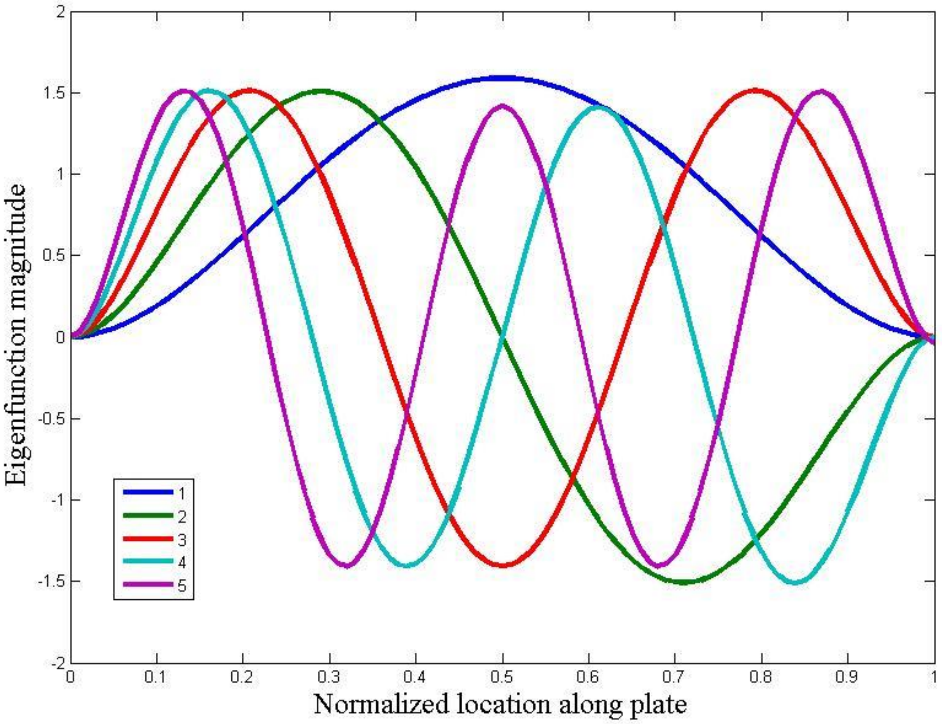

Figure 4.1. One-dimensional eigenfunction for a clamped plate at various modes.

4.5.2 Experimental Determination of the Mode Shapes

Experimentally determining the mode shapes through MPI requires first identifying possible natural frequencies of the structure, which usually correspond to peaks in the auto-spectral density of the vibration. Figure 4.2 shows the auto-spectral density of the vibration of the reference location for the experimental setup detailed in Chapter 3. The measured natural frequencies for various modes are marked in Figure 4.2. The natural frequency for mode <1,1> was measured to be 112 Hz and is the lowest natural frequency for the structure. It should be noted that the observation of a resonant peak on the reference laser's auto-spectral density validates that the reference laser is not located on a nodal line for the mode associated with that natural frequency.

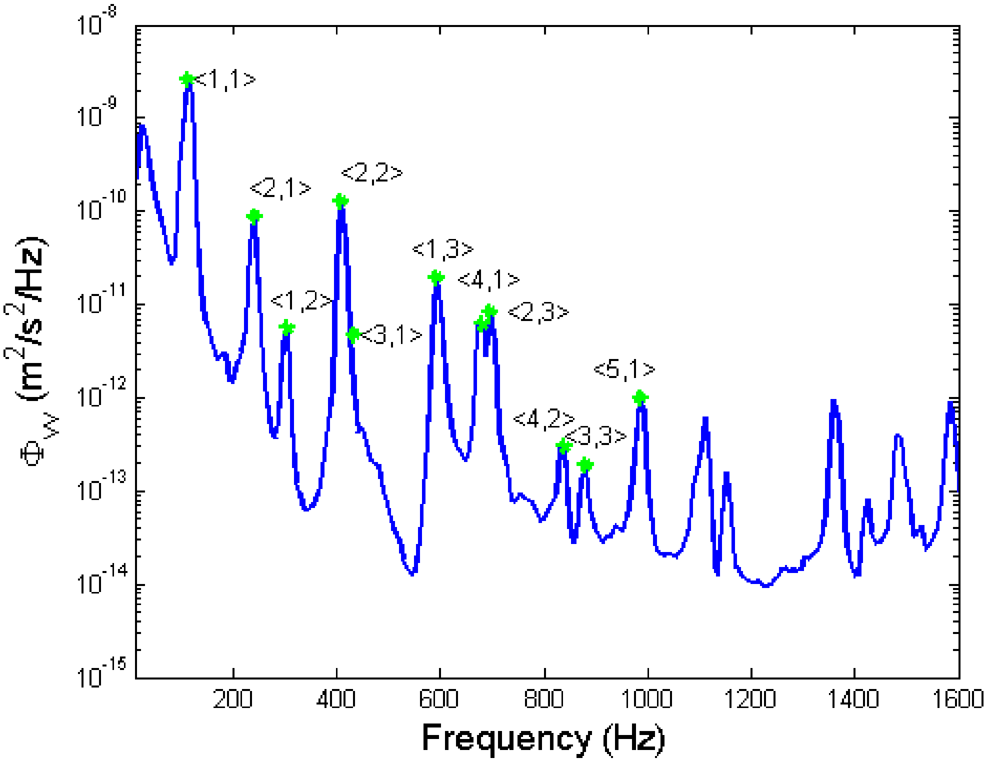

Figure 4.2. Auto-spectral density of the vibration of the reference location with natural frequencies marked for various modes.

The vibration of the plate detailed in Chapter 3 subjected to roughly 17 m/s free stream velocity flow was measured with a series of simultaneous two-point measurements from the single-point LDV and scanning LDV. 1015 equally-spaced points across the area of the plate (forming a grid of 35 locations in the streamwise direction and 29 in the spanwise direction) were measured using the scanning LDV. Simultaneously, a point in the bottom-right quadrant of the plate was scanned using the single point LDV. The point was verified to not lie on a node of the first 5 modes of vibration as doing so would result in no correlation between the single-point LDV and the scanning LDV at such a mode; otherwise, the point was simply chosen based on strong signal strength. The point did not directly coincide with any point scanned by the scanning LDV. Each pair of points was scanned simultaneously for 128 seconds at a sampling rate of 8192 Hz. These factors resulted in a strong enough correlation between the measurements single-point and scanning LDV to allow for use of MPI. Furthermore, a sufficient number of points were scanned with the scanning LDV to identify the spatial profiles of the first several modes.

The MPI was used with each two-point measurement to generate a magnitude and phase of vibration for the scanning laser location relative to the reference laser location. Examining the real component of the MPI for each location results in the shape of the vibration of the plate for that frequency, which was termed "surface shape" for that frequency. The surface shape is the superposition of the contributions of each mode active at that frequency. In Figure 4.2, one will note that there is no resonant peak to identify mode <3,1>. However, mode <3,1> is still identifiable by examining the surface shape of that frequency. This demonstrates one potential advantage of MPI over methods which rely solely on a single-point auto-spectral density, as such method would not be able to identify mode <3,1> in this situation.

If one assumes that a resonating mode has an amplitude that is orders of magnitude larger than all other modes as its natural frequency, then the superposition of all modes will be almost equal to solely the resonating mode at that frequency. Thus, the mode shape of a given mode can be approximated as being equal to the surface shape at that mode's natural frequency. This allows for experimental determination of mode shapes in structures whose mode shapes are not theoretically known. In this document, the measured surface shape for a frequency corresponding to the natural frequency of a mode was termed the "measured mode shape". Surface shapes for frequencies other than natural frequencies in general will not be dominated by single mode, so the superposition will in general contain substantial contributions from multiple modes.

The measured mode shapes for several modes are shown in Figures 4.3 - 4.6. Recall that these measured mode shapes were generated with turbulent boundary layer excitation. A ping test cannot be used with MPI because MPI requires statistically stationary vibration, and a ping test results in transient vibration. In each figure, the theoretical mode shapes predicted by Leissa[17] are also shown for purposes of comparison. In these figures, the axes have been linearly normalized to a maximum value of 1. One notes that the measured mode shapes through use of the MPI closely match the modes shapes predicted by Leissa. It is important to note that the measured mode shapes are those directly predicted by MPI and are not generated based on any assumptions as to the theoretical mode shape. Thus, the same measured mode shapes could be generated without knowledge of the theoretical mode shapes. For higher modes such as <5,1>, one notices a small amount of noise in the measured mode shape. However, the noise in the measured mode shape is relatively small given that the vibration of higher order modes are multiple orders of magnitude lower than the dominant mode <1,1>, which can be seen in Figure 4.2. The relatively low amount of noise observed is at least partially attributable to the MPI's tendency to remove random noise due to truly random noise being incoherent.

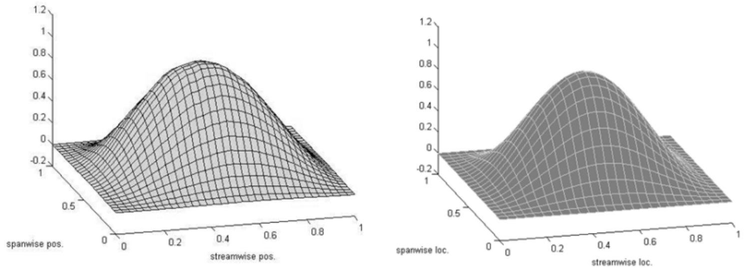

Measured Surface Shape

Theoretical Mode Shape

Figure 4.3. Measured mode shape (left) and theoretical mode shape (right) for mode <1,1>. Axes are normalized for a maximum value of 1.

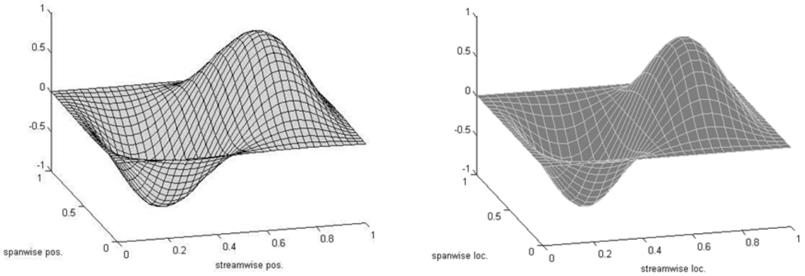

Measured Surface Shape

Theoretical Mode Shape

Figure 4.4. Measured mode shape (left) and theoretical mode shape (right) for mode <2,1>. Axes are normalized for a maximum value of 1.

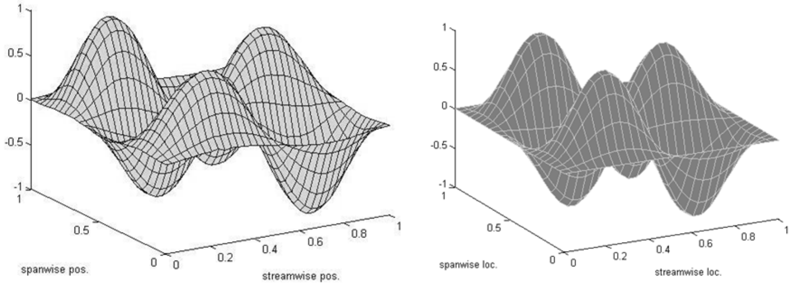

Measured Surface Shape

Theoretical Mode Shape

Figure 4.5. Measured mode shape (left) and theoretical mode shape (right) for mode <2,3>. Axes are normalized for a maximum value of 1.

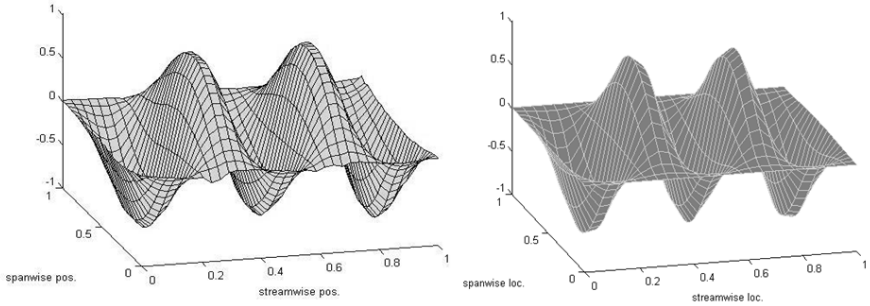

Measured Surface Shape

Theoretical Mode Shape

Figure 4.6. Measured mode shape (left) and theoretical mode shape (right) for mode <5,1>. Axes are normalized for a maximum value of 1.

The coherence for the first four modes is shown in Figures 4.7-4.10. The reference location is marked with an asterisk. As expected, the coherence is not a constant value of unity along the node lines. However, the coherence off the node lines appears to be relatively consistent both near and far from the reference location, indicating little loss in coherence as a function of spatial separation. The primary possible exception to this is mode <1,2>, where the coherence appears either low or subject to noise. It is not certain why this occurs, but examining Figure 4.2, one will note that the amplitude of vibration at the reference location at the natural frequency for mode <1,2> is substantially lower than the amplitude for most other modes. Thus, it is possible that the noise in the coherence at the natural frequency of mode <1,2> is a result of experimental error associated with a weaker signal-to-noise ratio due to the low amplitude of vibration of this mode. While such noise would affect coherence, the measured mode shape would be far less affected by such noise because MPI would tend to filter out the effects of such noise.

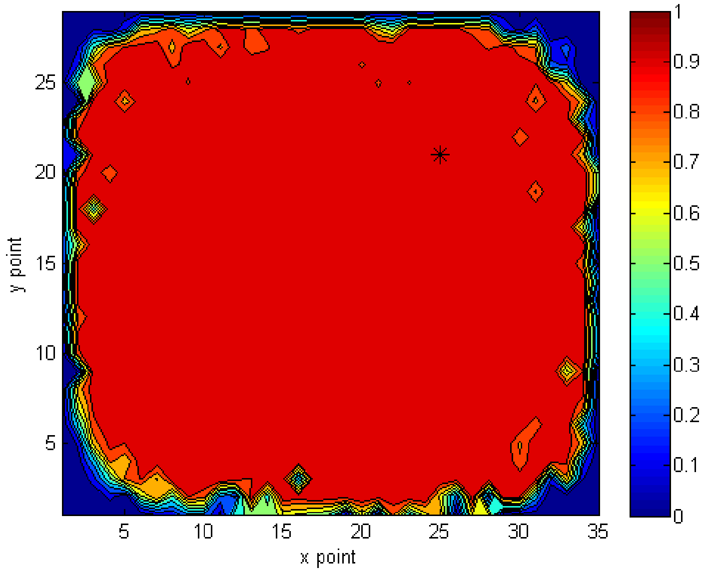

Figure 4.7. Coherence at the natural frequency for mode <1,1> for the non-fluid-loaded plate excited by a spatially homogeneous turbulent boundary layer.

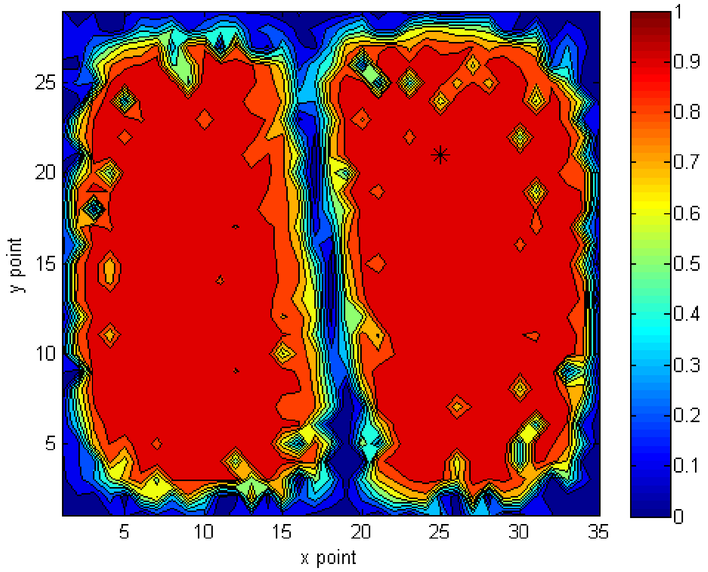

Figure 4.8. Coherence at the natural frequency for mode <2,1> for the non-fluid-loaded plate excited by a spatially homogeneous turbulent boundary layer.

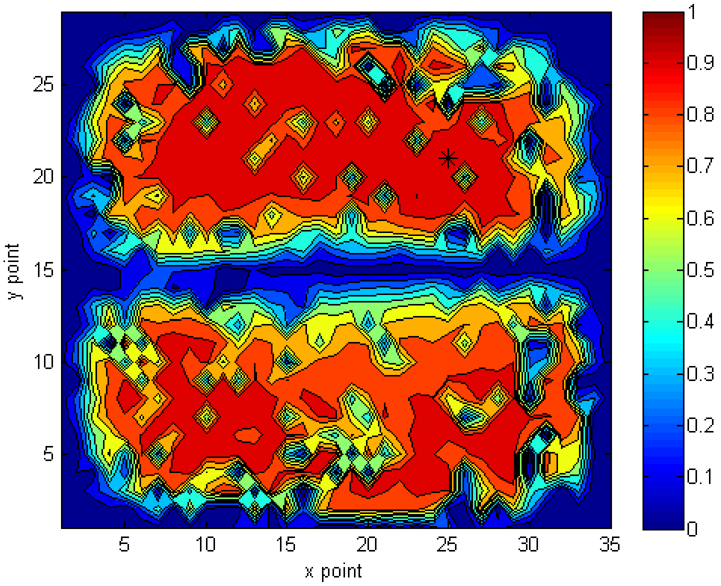

Figure 4.9. Coherence at the natural frequency for mode <1,2> for the non-fluid-loaded plate excited by a spatially homogeneous turbulent boundary layer.

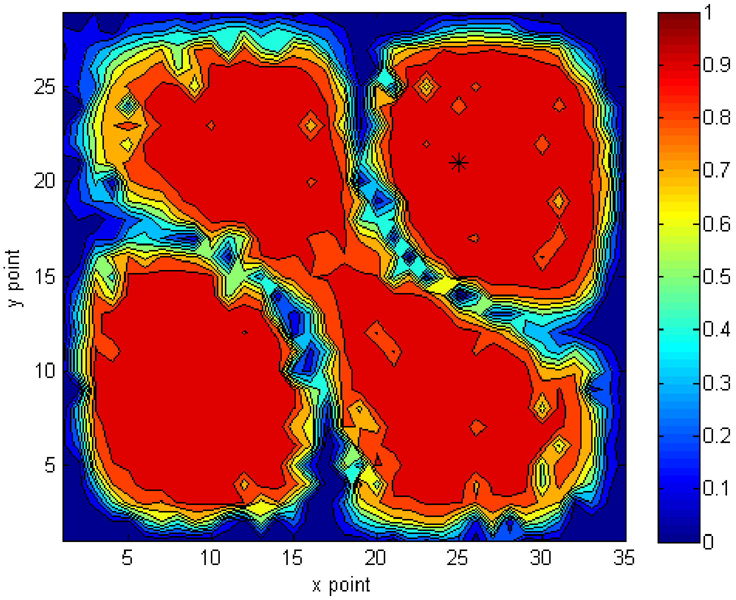

Figure 4.10. Coherence at the natural frequency for mode <1,1> for the non-fluid-loaded plate excited by a spatially homogeneous turbulent boundary layer.

4.6 Auto-spectral Density of the Vibration of Each Mode

Experimentally-determined vibration spectra for each mode were acquired by performing each of the modal decomposition methods outlined in Section 4.3. For either decomposition method, the mode shapes utilized were the measured mode shapes (acquired as outlined in Section 4.5) with natural frequencies below 1000 Hz. The frequency-dependent auto-spectral densities of vibration for several modes derived through both of these methods are shown in Figures 4.11-4.21. In these figures, the "experimental" vibration corresponds to the left side of Equation (4.4) and the "theoretical" vibration corresponds to the right side of Equation (4.4). For the theoretical portions of the plot, ω_{mn} was set equal to the natural frequencies measured in the experiments. $\Phi_{p,mn}$ was obtained by projecting the measured pressure spectra onto the mode shapes through Equations (4.20), (4.21), and (4.25), as outlined in Section 4.4. One should note that while these are plotted up to 1600 Hz that only mode shapes with natural frequencies below 1000 Hz were utilized in the modal composition. This was done to allow for better contrast between the two decomposition methods, which will be done later in this section.

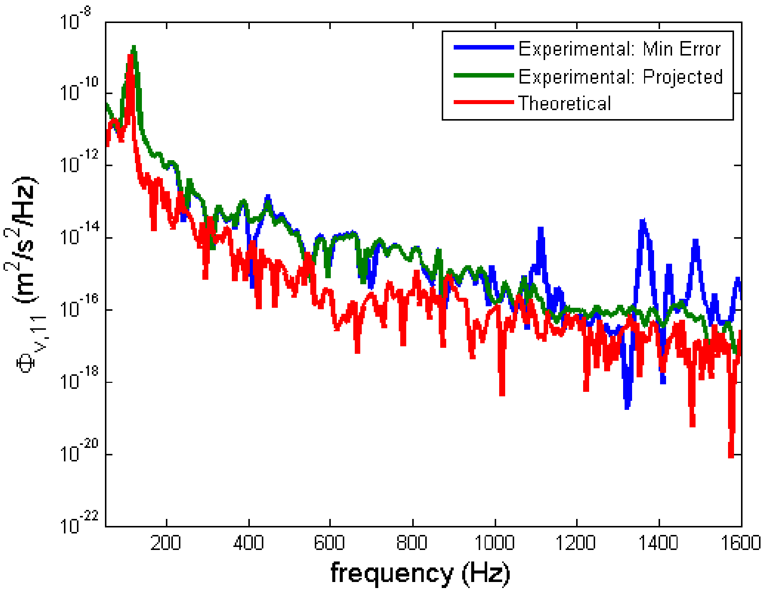

Figure 4.11. Experimentally measured and theoretical auto-spectral density of vibration for mode <1,1>. Measured spectra derived from both minimization of error and projected modal decomposition methods.

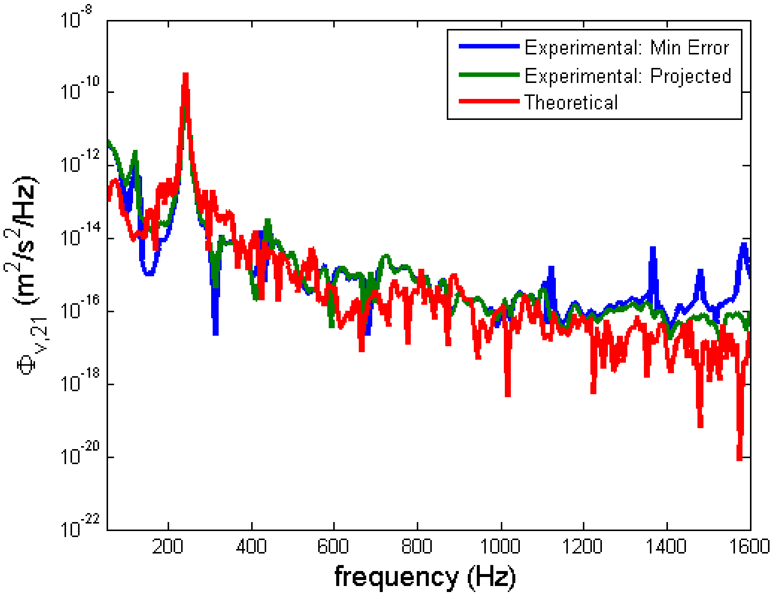

Figure 4.12. Experimentally measured and theoretical auto-spectral density of vibration for mode <2,1>. Measured spectra derived from both minimization of error and projected modal decomposition methods.

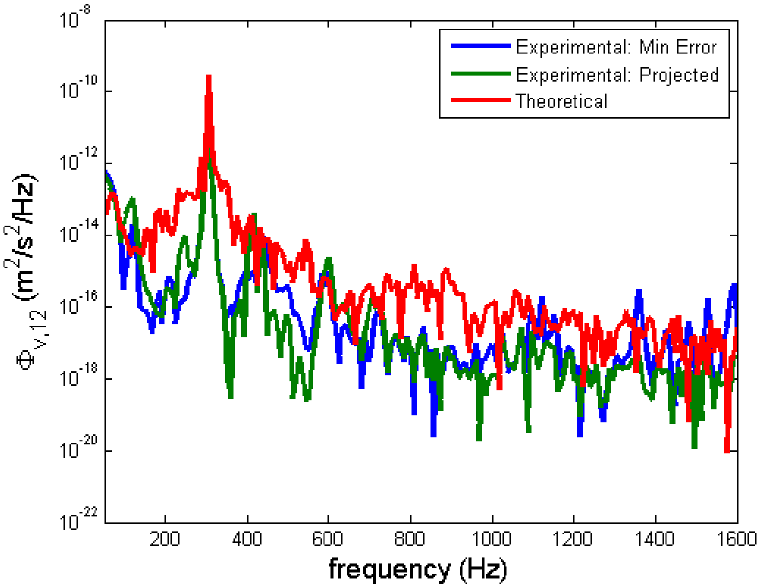

Figure 4.13. Experimentally measured and theoretical auto-spectral density of vibration for mode <1,2>. Measured spectra derived from both minimization of error and projected modal decomposition methods.

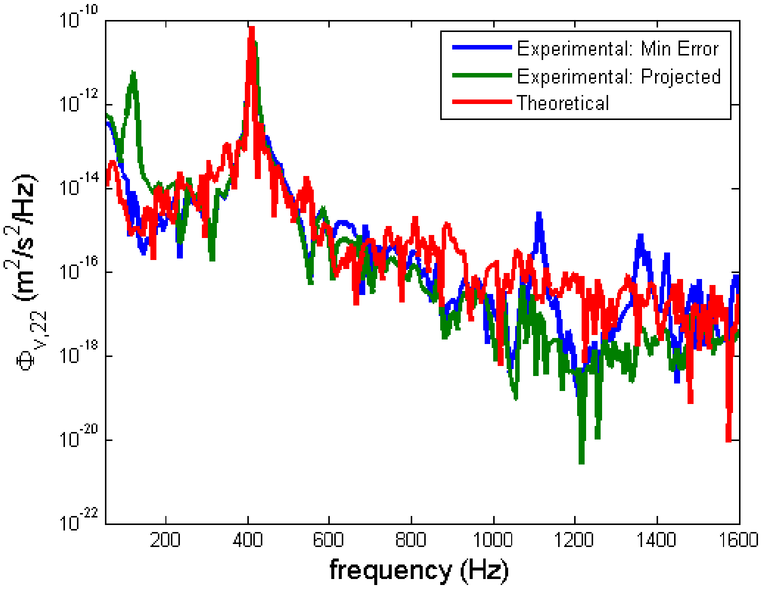

Figure 4.14. Experimentally measured and theoretical auto-spectral density of vibration for mode <2,2>. Measured spectra derived from both minimization of error and projected modal decomposition methods.

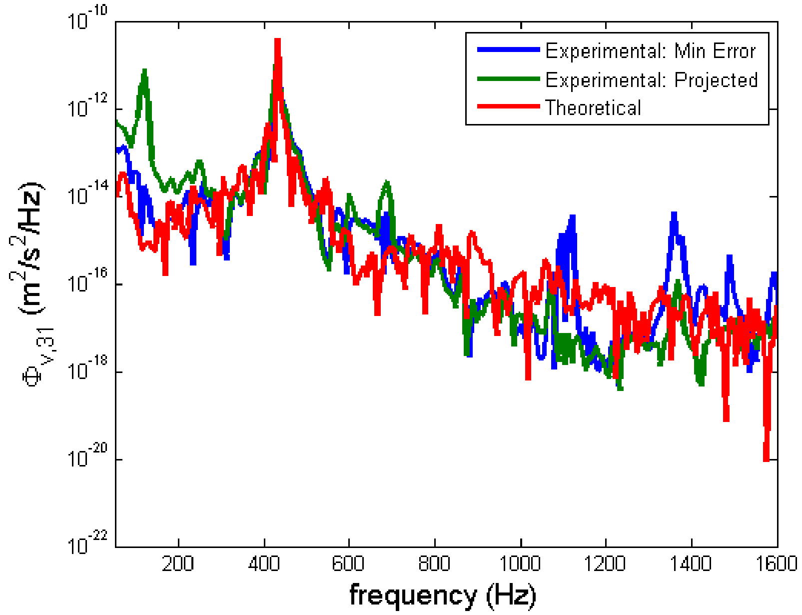

Figure 4.15. Experimentally measured and theoretical auto-spectral density of vibration for mode <3,1>. Measured spectra derived from both minimization of error and projected modal decomposition methods.

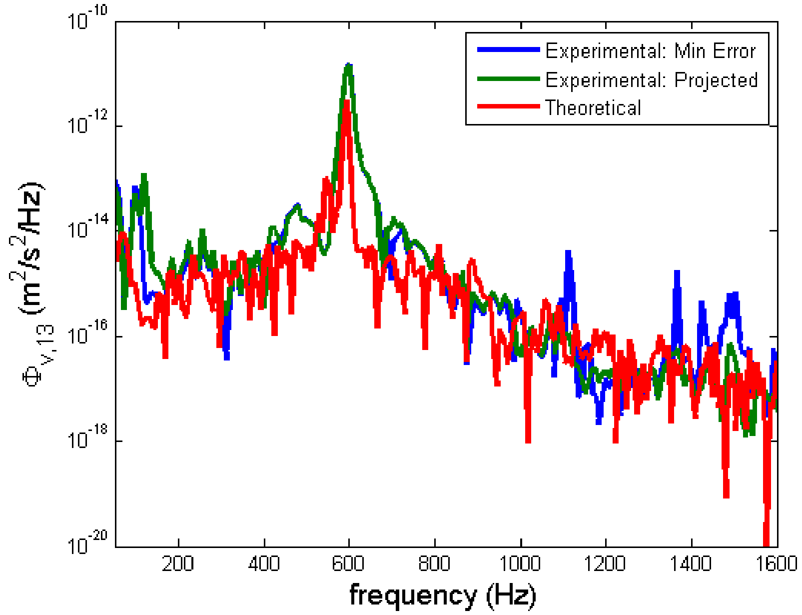

Figure 4.16. Experimentally measured and theoretical auto-spectral density of vibration for mode <1,3>. Measured spectra derived from both minimization of error and projected modal decomposition methods.

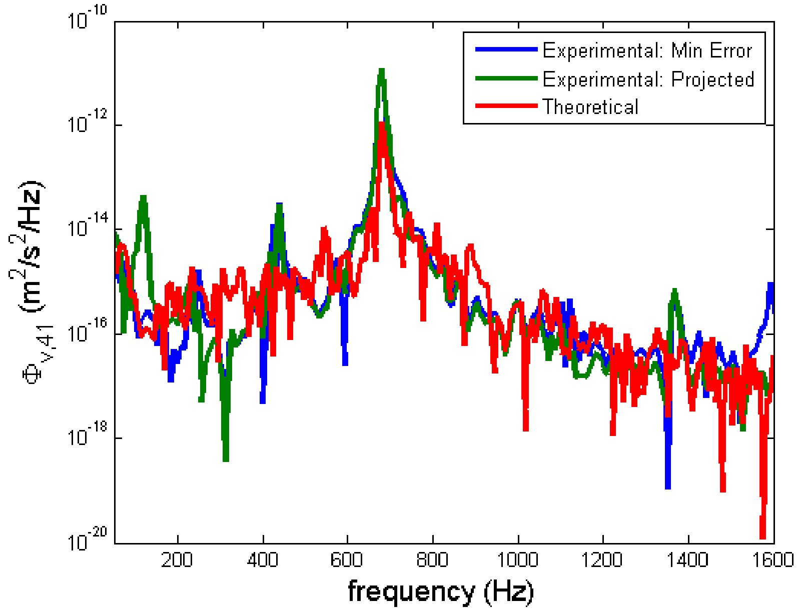

Figure 4.17. Experimentally measured and theoretical auto-spectral density of vibration for mode <4,1>. Measured spectra derived from both minimization of error and projected modal decomposition methods.

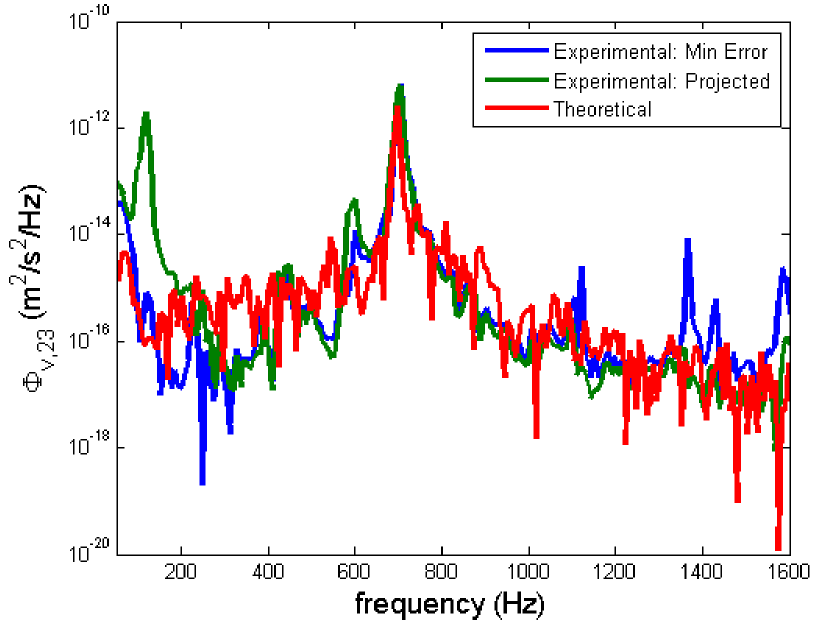

Figure 4.18. Experimentally measured and theoretical auto-spectral density of vibration for mode <2,3>. Measured spectra derived from both minimization of error and projected modal decomposition methods.

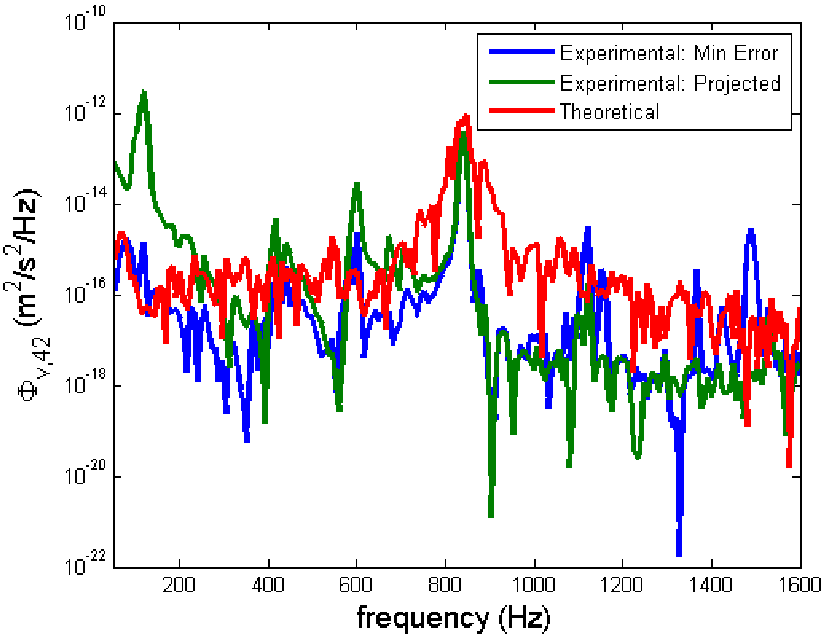

Figure 4.19. Experimentally measured and theoretical auto-spectral density of vibration for mode <4,2>. Measured spectra derived from both minimization of error and projected modal decomposition methods.

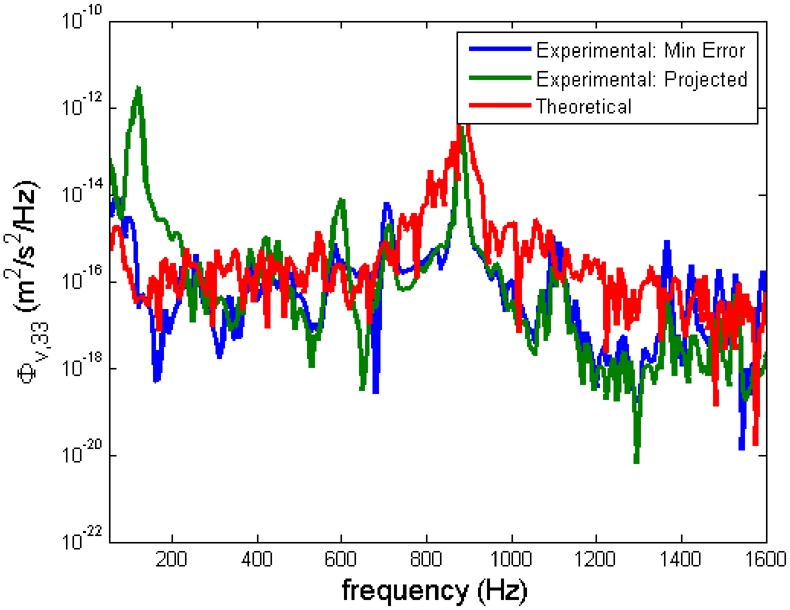

Figure 4.20. Experimentally measured and theoretical auto-spectral density of vibration for mode <3,3>. Measured spectra derived from both minimization of error and projected modal decomposition methods.

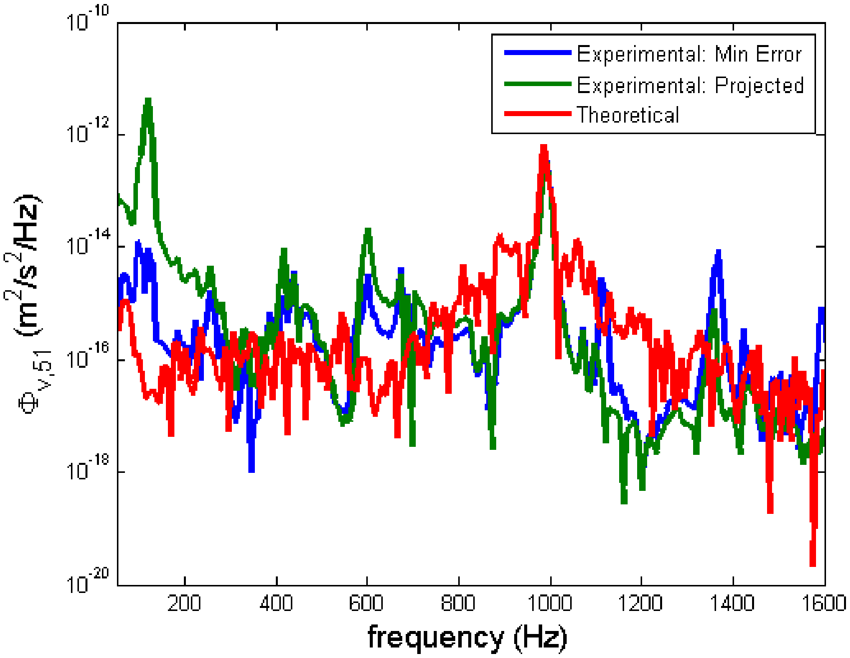

Figure 4.21. Experimentally measured and theoretical auto-spectral density of vibration for mode <5,1>. Measured spectra derived from both minimization of error and projected modal decomposition methods.

A good but imperfect agreement exists between the measured and theoretical vibrations. Because the MPI does not obtain simultaneous measurements for all points and because the excitation of the plate is stochastic in nature, convergence can be slow, which may lead to errors in the results. One should note the range of orders of magnitude present in the figures. Mode <1,1> is the largest mode of vibration for the plate. The difference in the auto-spectral density between mode <1,1>'s resonant peak and many of the measured/predicted values of the other modes is greater than six orders of magnitude, which can cause small errors in the decomposition to translate into large differences in the resulting spectra. By contrast to the orders of magnitude present, the errors in the figures are relatively small.

Figures 4.11-4.21 contrast the relative merits of the two modal decomposition methods. The projection method of modal decomposition is based on the assumption that all modes are orthogonal to one another. In theory this should be true as this is a requirement for a mode shape to be an eigenfunction. A mathematical expression of perfect orthogonality of the mode shapes can be expressed as $\Psi\Psi^T = A_{plate}I$, which is imposed by the normalization condition of Equation (4.2). In practice, the measured mode shapes will have a non-zero amount of error in comparison to the true mode shapes of the structure. This will result in at least a small degree of non-orthogonality of the measured mode shapes, which appears as non-zero off-diagonal elements of $\Psi\Psi^T$. Greater errors in the mode shapes will result in less orthogonal mode shapes which have greater values of the off-diagonal elements of $\Psi\Psi^T$. The off-diagonal elements in $\Psi\Psi^T$ will result in a modal decomposition where small portions of the true vibration of a mode will appear in the measured spectra of another mode. At a frequency coinciding with the resonant peak of one mode, a small amount of non-orthogonality can result in a noticeable peak in the other modes' spectra due to the relatively high magnitude of the resonant peak; this peak is not truly occurring in the structure, it is simply an error in the decomposition.

CHAPTER 5

VIBRATION OF FLUID-LOADED STRUCTURES DUE TO NON-HOMOGENEOUS FORCING

5.1 Chapter Outline

Section 2.1 outlined the fundamental equations of vibration for fluid-loaded structures. Fluid-loaded structures are those structures which have relatively low density per unit area compared to the surrounding fluid medium. Specifically, structures are considered to be fluid-loaded for values of $\beta >> 1$, as defined in Equation (2.15). The vibration of a fluid-loaded structure is altered by the surrounding fluid medium beyond the wall pressure generated by the flow field. In particular, fluid loading of a structure has an effect equivalent to increasing the mass and damping of the structure. As demonstrated by Equation (2.24), fluid-loaded structures can in general be solved in the same fashion as non-fluid loaded structures by altering the mass, damping, and natural frequency of the second-order differential equation of vibration for each mode.

The goal of this chapter is to be an exploratory study to show that the damping created by the fluid loading of the structure can alter the mode shapes of structures when subjected to spatially non-homogeneous forcing fields. Non-fluid-loaded structures have mode shapes which are independent of the forcing field applied to the structure. By demonstrating that the forcing field can affect the mode shapes of a structure, it is shown that fluid-loaded-structural vibration may not always be solved as a special case of non-fluid-loaded structural but using the same general solution procedure. This also questions the validity of using standard modal analysis in the solution of the structural vibration. While fluid-loaded structures may have similar mode shapes to non-fluid-loaded structures, the ability of mode shapes to be dependent on the forcing field is not consistent with premises involved in solving structural vibration though standard modal analysis.

As will be demonstrated in this chapter, the resulting mode shapes of a rectangular structure due to non-homogeneous forcing tend to be non-symmetric. This has substantial implications for the acoustic radiation of the structure. The symmetry of the mode shapes of the vibration of a rectangular structure creates significant acoustic cancellations in the far-field of the structure. With asymmetrical structural vibration, such acoustic cancellations do not occur in the far-field, resulting in a more efficient acoustic radiator.

The chapter is divided into several sections which sequentially work towards the case of analyzing the response of a fluid-loaded structure subjected to spatially non-homogeneous forcing. Chapter 4 examined the vibration of a non-fluid-loaded structure due to spatially homogeneous forcing, which could be considered the canonical case. Similar experimental and analysis techniques will be used for the cases presented in this chapter. Chapter 4 both serves as the first case involved in the analysis which will occur in Chapter 5 as well as validation of the experimental and analytical techniques which will be used in this chapter. Section 5.2 examines the vibration of a non-fluid-loaded structure due to non-homogeneous forcing. The purpose of this section is to validate the forcing field does not result in a qualitative difference in the vibrational response of a non-fluid-loaded structures other than changing the projected pressure.

Section 5.3 examines the vibration of a fluid-loaded structure due to spatially homogeneous forcing. The section will demonstrate that the structure appears to vibrate in a similar fashion to the previously presented cases, though differences in the coherence field will be presented. Section 5.4 examines the vibration of a fluid-loaded structure due to spatially non-homogeneous forcing, the primary case which this chapter leads towards. The purpose of this section is to demonstrate that only when both of these conditions are met that the structure will have an appreciable change in its mode shapes. Section 5.5 utilizes a discretized model of a string to demonstrate how high damping can result in comparable vibration fields to those observed in the previous experiments. While the model is not designed to be a prediction, it is designed to demonstrate the underlying physics of the problem. A tabular layout of these cases can be seen in Table 5.1.

TABLE 5.1

FOUR STRUCTURAL VIBRATION CASES EXAMINED

	Spatially Homogeneous Forcing	**Spatially Non-homogeneous Forcing**
Non fluid loaded	- Canonical structural vibration - Chapter 4	- Qualitatively identical to canonical case - Section 5.2
Fluid loaded	- Still composed of relatively symmetrical mode shapes - Section 5.3	- Mode shapes appear non-symmetric even on a symmetric structure - Section 5.4

Mode shapes in this chapter will be plotted as their surface shapes. Wavenumber-dependent plots of the first several modes shapes can be found in Appendix A.

5.2 Spatially Non-homogeneous Forcing of a Non Fluid Loaded Structure

This section will examine the effects of exciting a non-fluid-loaded structure with a spatially non-homogeneous forcing field. The vertical splitter outlined in Section 3.1, and shown in Figures 3.9 and 3.10, was used to create the spatial non-homogeneity in the wall pressure field. The resulting amplitude of the wall pressure appears similar to that as a step function in the spanwise direction, creating an extremely spatially non-homogeneous wall pressure field. The structure was excited with a free stream velocity of approximately 17 m/s, with this flow only exciting approximately the bottom third of the plate. This is the same excitation speed used for setup in Chapter 4, involving the non-fluid-loaded spatially homogeneous plate vibration.

The experimental mode shapes, determined in the same manner as demonstrated in Chapter 4, are shown in Figures 5.1-5.3 when excited with the vertical splitter. The mode shapes are essentially identical to those that were experimentally determined for the non-fluid-loaded plate excited by a spatially homogeneous wall pressure field. This was an anticipated occurrence based on the theoretical equations of vibration and serves to validate this assumption.

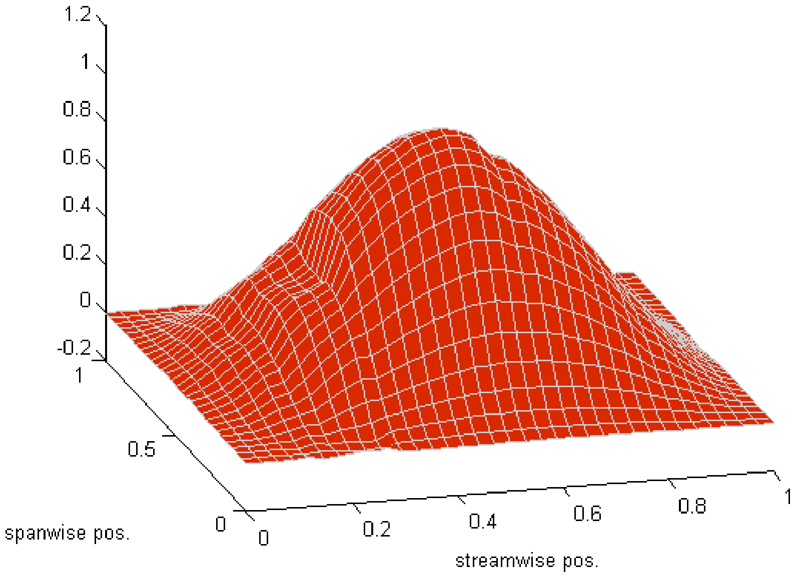

Figure 5.1. Experimentally-determined mode shape for the non-fluid-loaded plate using the vertical splitter for mode <1,1>.

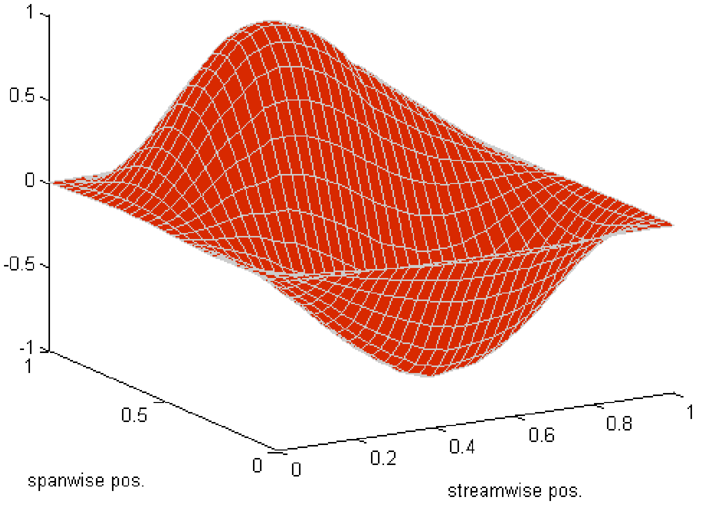

Figure 5.2. Experimentally-determined mode shape for the non-fluid-loaded plate using the vertical splitter for mode <1,2>.

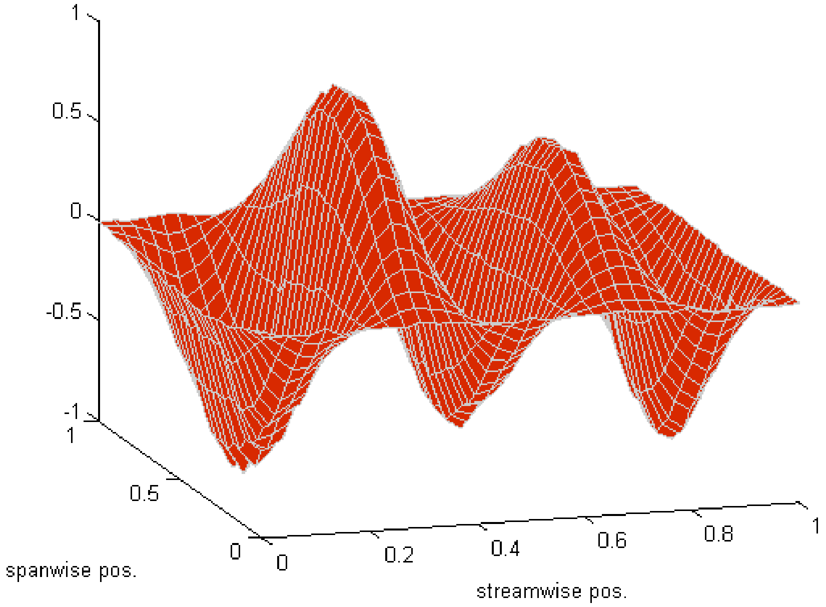

Figure 5.3. Experimentally-determined mode shape for the non-fluid-loaded plate using the vertical splitter for mode <5,1>.

The coherence for the natural frequencies corresponding to the first four modes are shown in Figures 5.4-5.7. Similar to the case of the non-fluid-loaded plate with spatially homogeneous forcing, the coherence shows little or no decay as a function of spatial position.

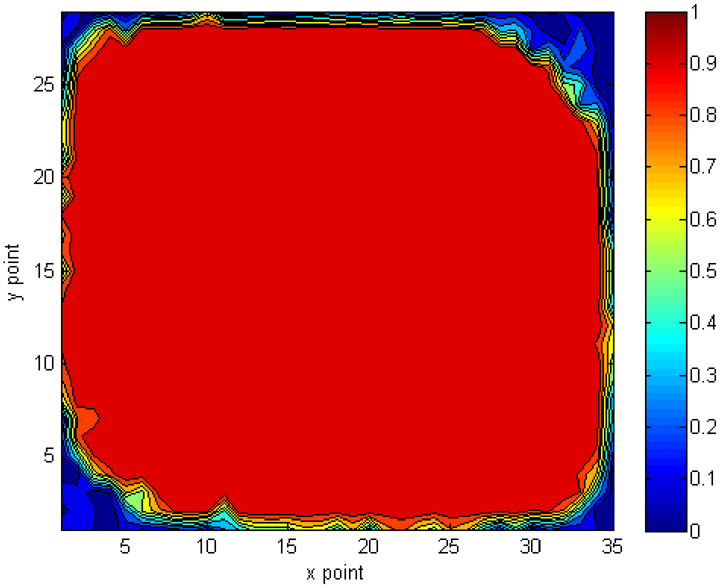

Figure 5.4. Coherence at the natural frequency for mode <1,1> for the non-fluid-loaded plate excited with the vertical splitter.

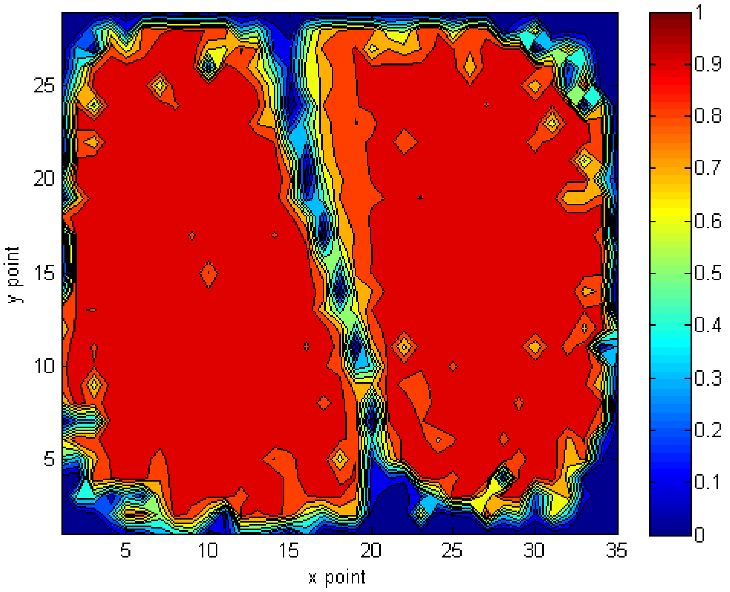

Figure 5.5. Coherence at the natural frequency for mode <2,1> for the non-fluid-loaded plate excited with the vertical splitter.

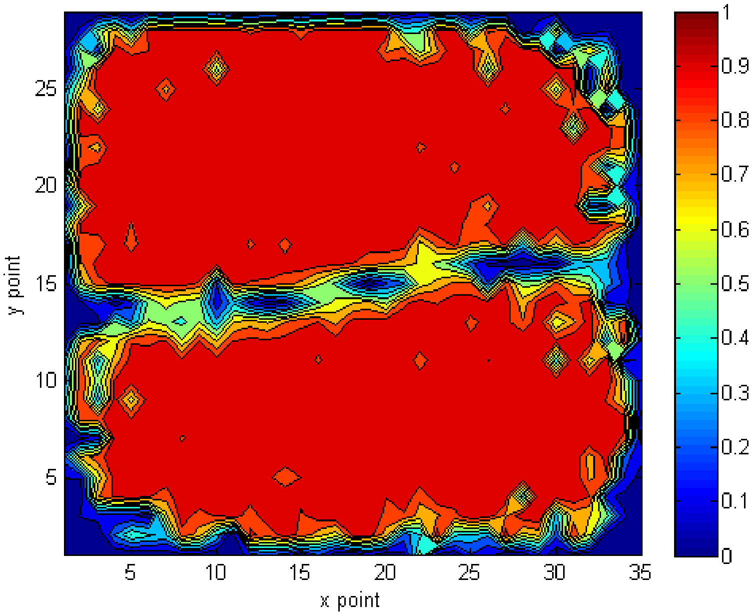

Figure 5.6. Coherence at the natural frequency for mode <1,2> for the non-fluid-loaded plate excited with the vertical splitter.

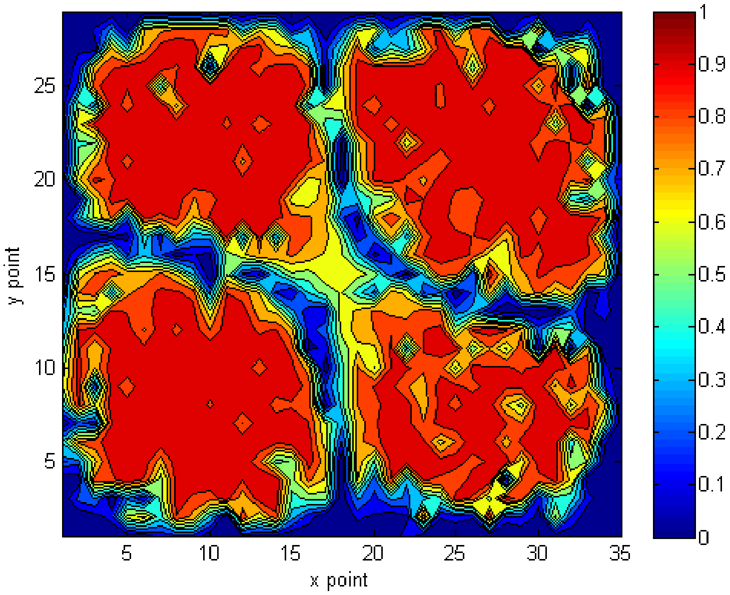

Figure 5.7. Coherence at the natural frequency for mode <2,2> for the non-fluid-loaded plate excited with the vertical splitter.

The experimental and theoretical auto-spectral density of vibration for several modes, determined in the same manner as demonstrated in Chapter 4, are shown in Figures 5.8-5.11 when excited with the vertical splitter. The resulting auto-spectral densities of vibration are roughly identical to those of the case excited in a spatially-homogeneous fashion but with a lower magnitude. This was an anticipated occurrence based on the theoretical equations of vibration. The experimental results also match the theoretical predictions relatively well, with the exception of mode <1,1>. It is suspected that this is caused by errors in measuring the wall pressure field for mode 1 in the spanwise direction due to the limited area over which the pressure field can be measured.

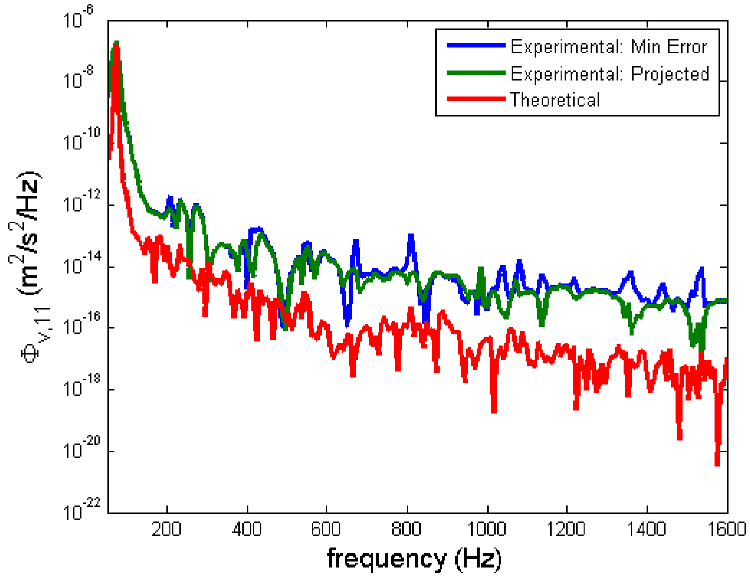

Figure 5.8. Theoretical and experimental auto-spectral density of vibration for the non-fluid-loaded plate, excited by the vertical splitter, for mode <1,1>.

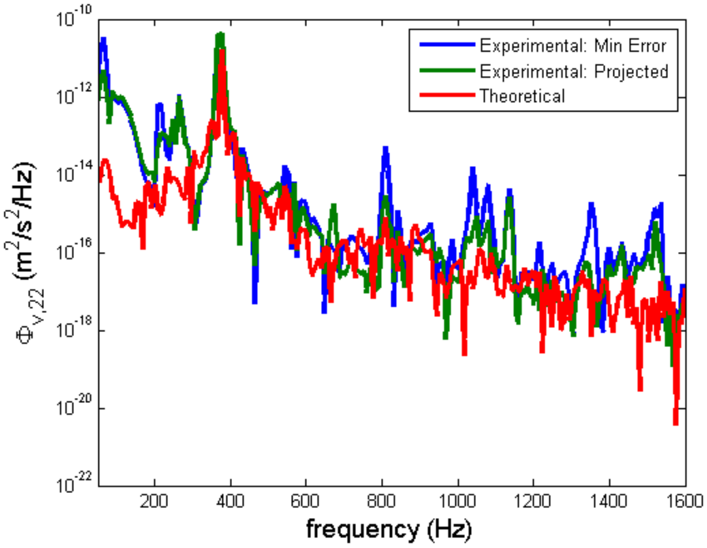

Figure 5.9. Theoretical and experimental auto-spectral density of vibration for the non-fluid-loaded plate, excited by the vertical splitter, for mode <2,2>.

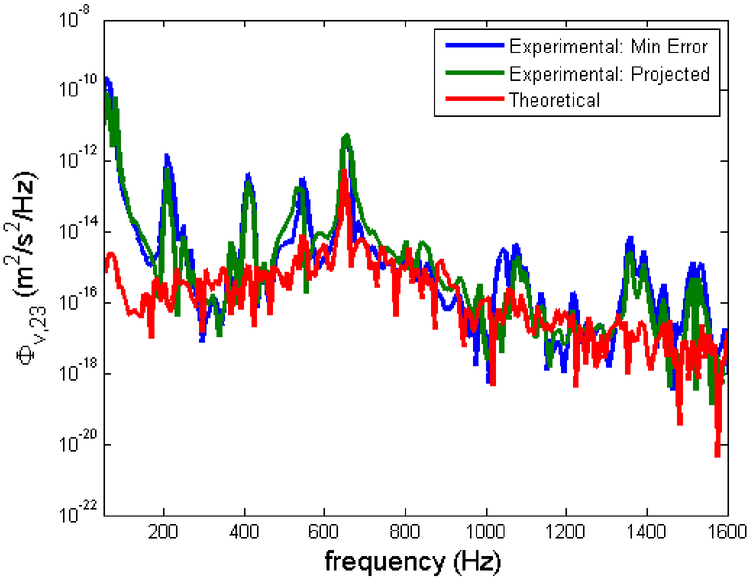

Figure 5.10. Theoretical and experimental auto-spectral density of vibration for the non-fluid-loaded plate, excited by the vertical splitter, for mode <2,3>.

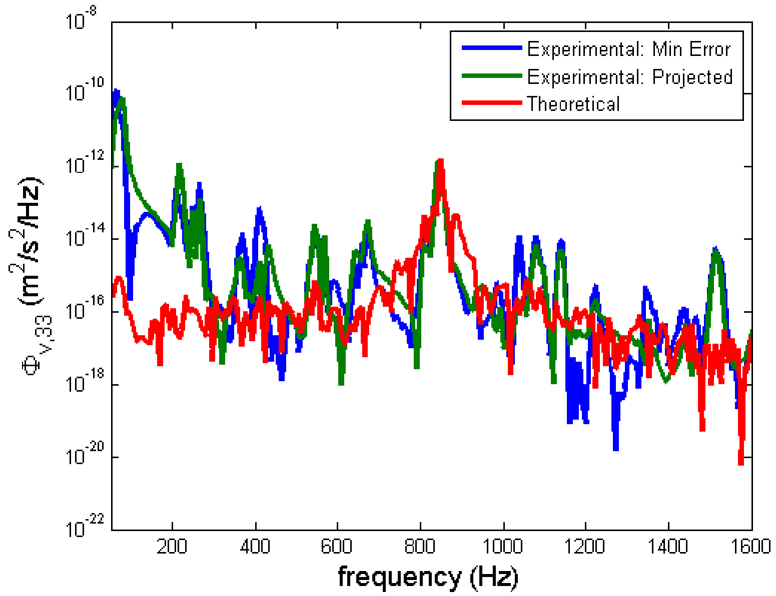

Figure 5.11. Theoretical and experimental auto-spectral density of vibration for the non-fluid-loaded plate, excited by the vertical splitter, for mode <3,3>.

The primary result to be taken from this section is that a non-fluid-loaded plate vibrates qualitatively the same independent of whether the forcing field is spatially homogeneous or non-homogeneously. This was anticipated to be true and is consistent with what the theory of structural vibration would predict.

5.3 Fluid Loaded Vibration with Spatially Homogeneous Forcing

The purpose of this section is to examine the vibration of a fluid-loaded foil under spatially-homogeneous excitation. For this section, the setup outlined in Chapter 3 was used with no use of a splitter. The plate was replaced with a 0.002 inch thick (0.0508 mm) piece of aluminum; otherwise, the physical setup was unchanged. The free stream velocity of the flow was reduced to approximately 9 m/s due to the increased response of the foil to flow excitation. The auto-spectral density of the vibration of the foil at the reference location is shown in Figure 5.12. The first natural frequency measured in the experiment occurred at approximately 60 Hz. The fluid loading factor at this frequency, as per Equation 2.15, is approximately $\beta = 7.76$, which is greater than 1, thus indicating that the foil is fluid loaded.

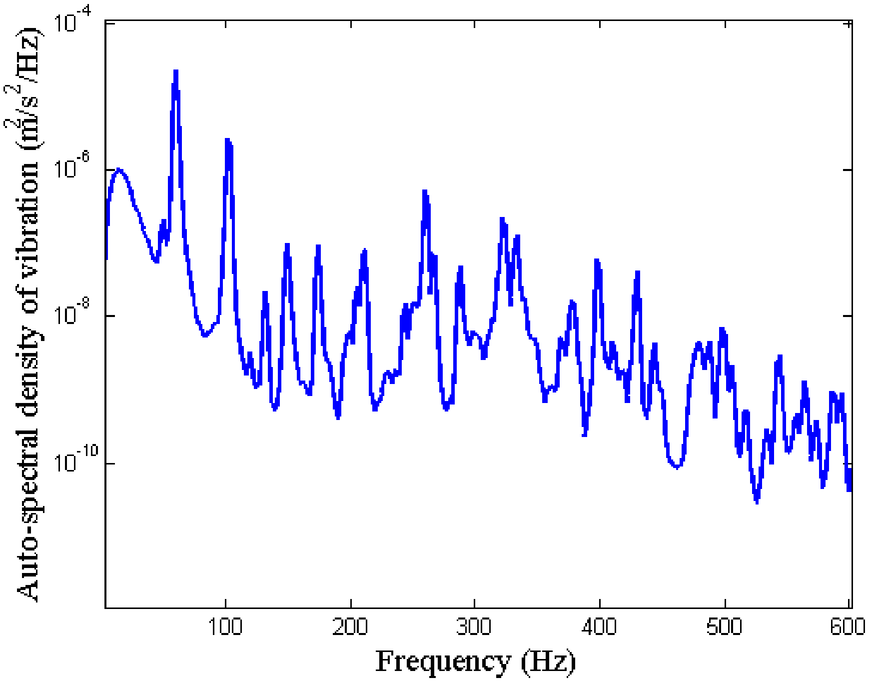

Figure 5.12. Auto-spectral density of vibration at the reference location for the fluid-loaded foil with standard, spatially-homogeneous turbulent boundary layer forcing.

The experimentally-determined mode shapes for the fluid-loaded foil under spatially homogeneous wall pressure excitation are shown in Figure 5.13. It should be noted that while the modes are similar to those of the non-fluid-loaded plate used in the previous experiments, there is a small asymmetry to the foil. This is caused by limitations in the ability to provide perfectly uniform tension in the foil, but this does not affect the underlying physics of the problem. In particular, one can note that the maximum values of the peaks of the mode shapes are nearly identical for a given mode shape; the mode shapes were plotted as contours in this case in order to make this feature more noticeable.

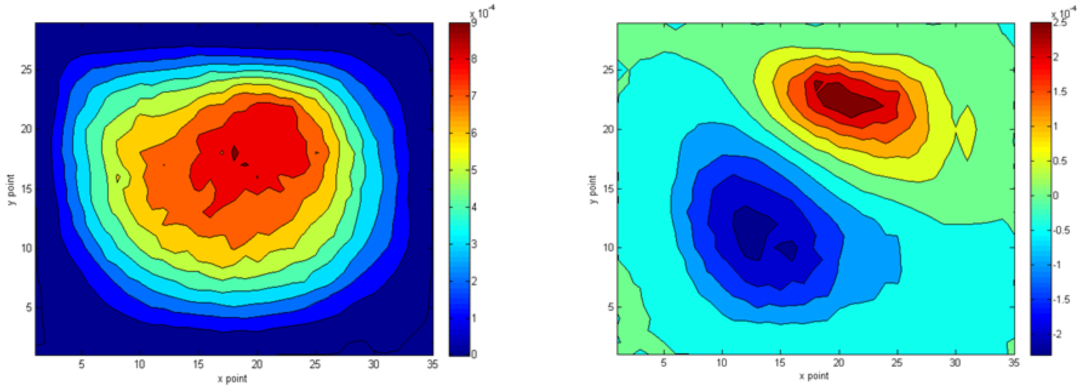

Mode 1-1 (60 Hz)

Mode 1-2 (102Hz)

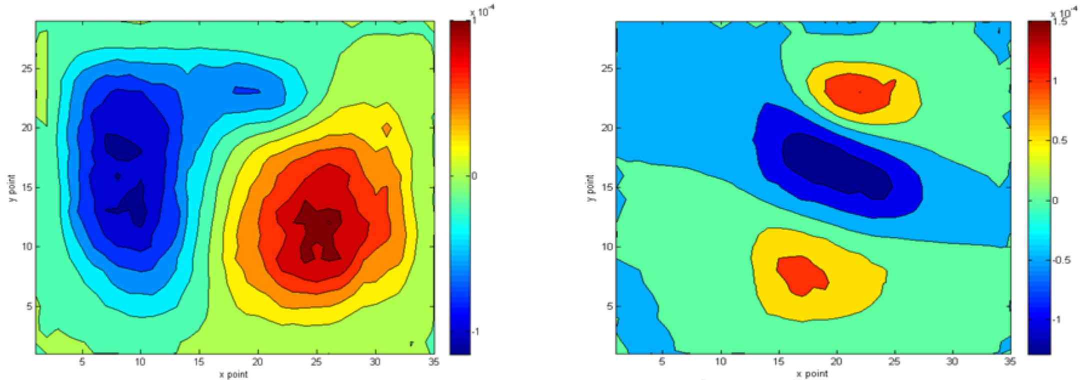

Mode 2-1 (132Hz)

Mode 1-3 (150Hz)

Figure 5.13. Measured mode shapes for the first four modes of vibration for the fluid-loaded foil under the effects of spatially homogeneous forcing. Frequency indicates the natural frequency of the mode.

Figure 5.14 shows the coherence plots for the same modes as those shown in Figure 5.13. The peaks have a high coherence like was seen in the case of the non-fluid-loaded plate. Off of the peaks, there appears to be a small decay in coherence for increasing spatial separation for increasing modes. This is different than the non-fluid-loaded plate, where the coherence did not appear to decay as a function of spatial separation from the reference location. The conclusion of this section is that a fluid-loaded structure under the effects of homogeneous forcing appears to vibrate with conventional mode shapes but does so with a lower coherence field than a non-fluid-loaded structure.

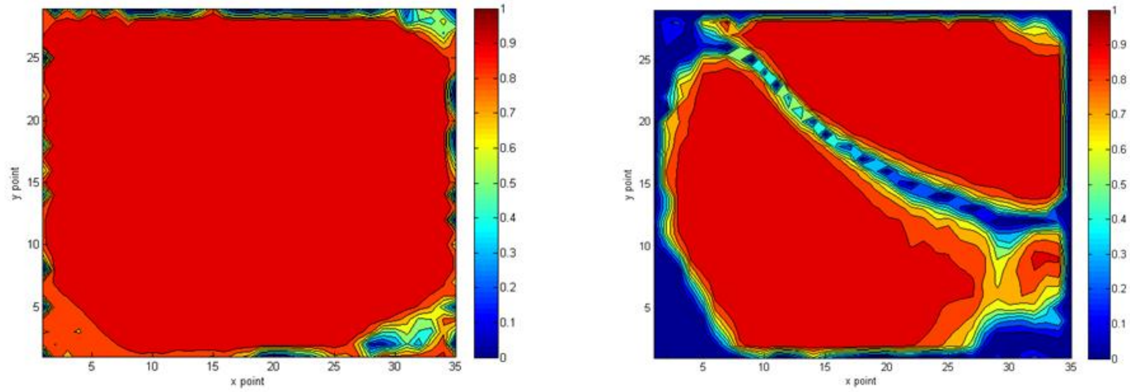

Mode 1-1 (60 Hz)

Mode 1-2 (102Hz)

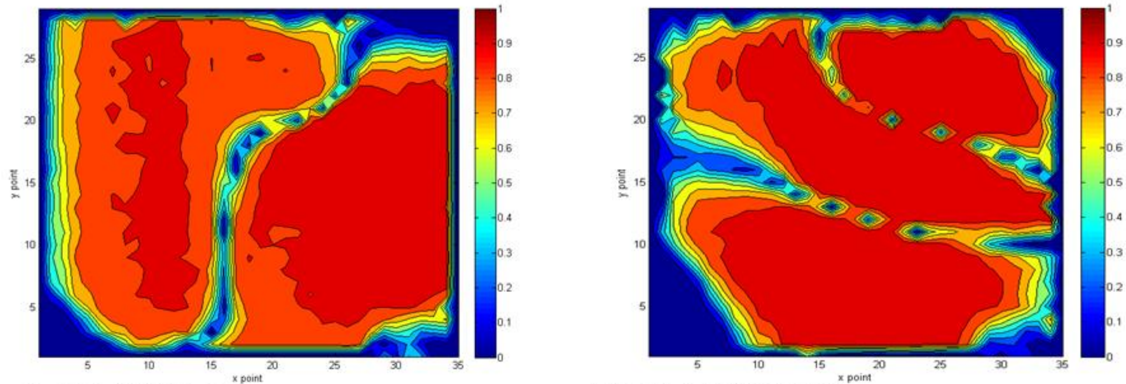

Mode 2-1 (132Hz)

Mode 1-3 (150Hz)

Figure 5.14. Measured coherence for the first four modes of vibration for the fluid-loaded foil under the effects of spatially homogeneous forcing. Frequency indicates the natural frequency of the mode.

5.4. Fluid Loaded Vibration with Spatially Non-Homogeneous Forcing

The purpose of this section is to examine the vibration of a fluid-loaded foil under the effects of a spatially non-homogeneous wall pressure field. All previous cases were examined in order to be compared to this final case. The experimental setup is the same as the one used in Section 5.3: the vibrating structure was a 0.002 inch thick (0.0508 mm) piece of aluminum excited by 9m/s flow. The flow field exciting the structure in this section was altered using a splitter. The vertical splitter and the horizontal splitter, outlined in Section 3.1, were used in separate experiments to create a spatially non-homogeneous wall pressure field, with the former creating a strong spanwise non-homogeneous wall pressure and the latter creating a strong streamwise non-homogeneous wall pressure. In either situation, the first natural frequency was measured to be 66 Hz, for which the fluid loading factor is $\beta = 7.06$, which is a comparable fluid loading factor to the case of the fluid-loaded foil with spatially homogeneous wall pressure.

For the case of the vertical splitter, the auto-spectral density of vibration at the reference location is shown in Figure 5.15. Figures 5.16 and 5.17 show the first four experimentally-determined mode shapes and the coherence at the corresponding frequencies. Note that in Figures 5.16 and 5.17 that the bottom portion of the figure corresponds to the location where the flow is blocked. Figures 5.18, 5.19, and 5.20 show the same plots when the horizontal splitter was used instead of the vertical splitter. In Figures 5.19 and 5.20, the right side of the contour plots correspond to where the flow was blocked.

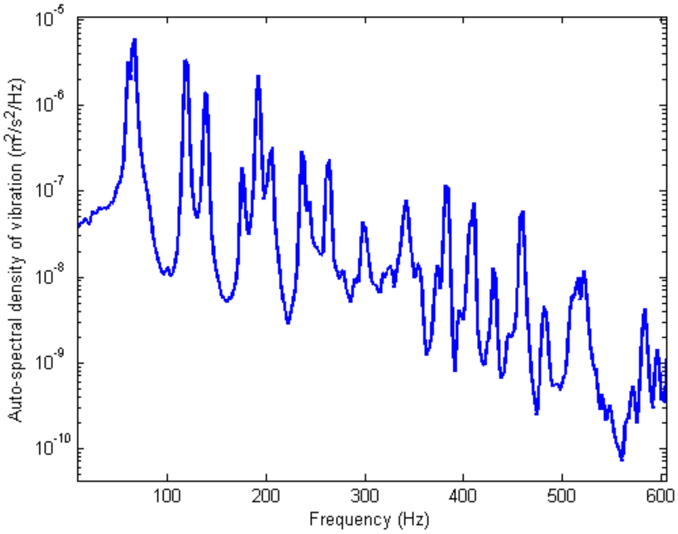

Figure 5.15. Auto-spectral density of vibration at the reference location for the fluid-loaded foil under the effects of the vertical splitter.

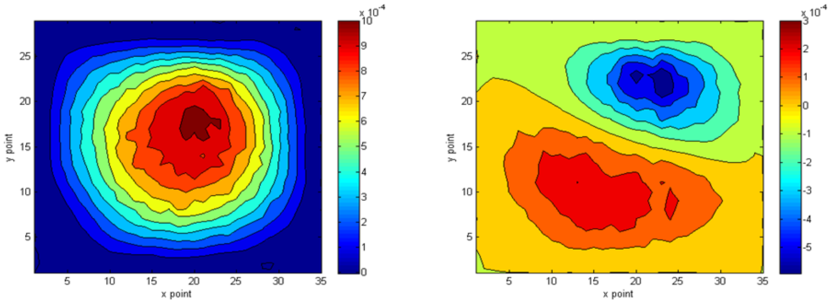

Mode 1-1 (66 Hz)

Mode 1-2 (118 Hz)

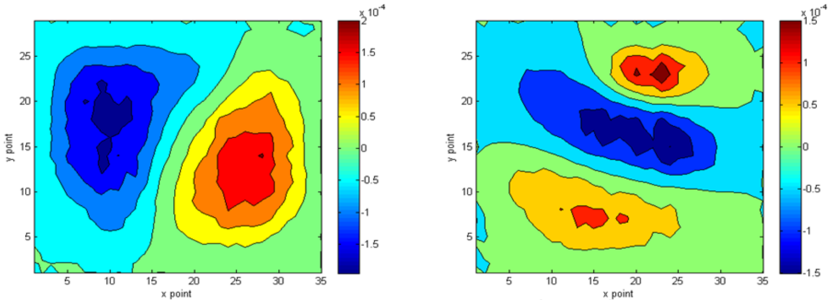

Mode 2-1 (138Hz)

Mode 1-3 (176Hz)

Figure 5.16. Measured mode shapes for the first four modes of vibration for the fluid-loaded foil under the effects of the vertical splitter. Frequency indicates the natural frequency of the mode.

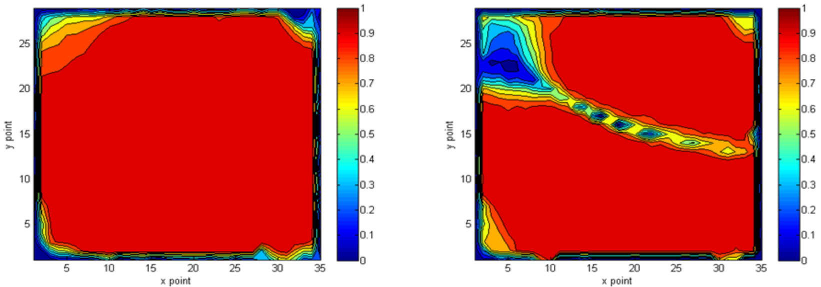

Mode 1-1 (66 Hz) Mode 1-2 (118 Hz)

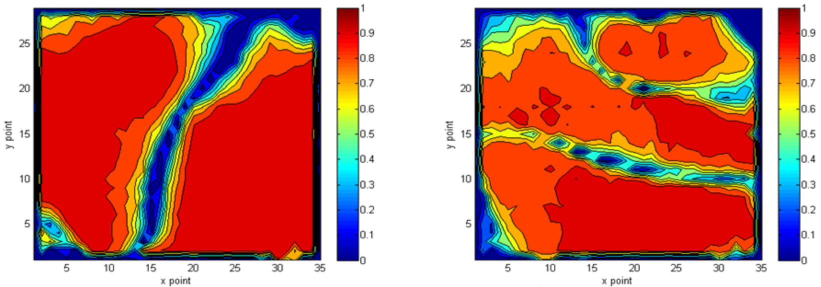

Mode 2-1 (138Hz) Mode 1-3 (176Hz)

Figure 5.17. Measured coherence for the first four modes of vibration for the fluid-loaded foil under the effects of the vertical splitter. Frequency indicates the natural frequency of the mode.

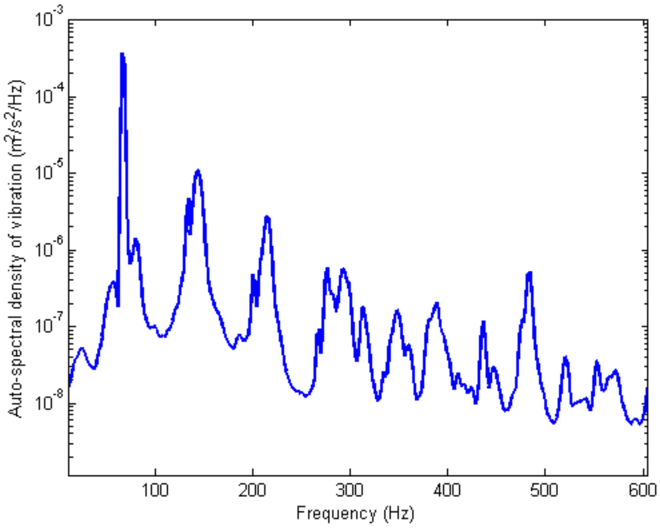

Figure 5.18. Auto-spectral density of vibration at the reference location for the fluid-loaded foil under the effects of the horizontal splitter.

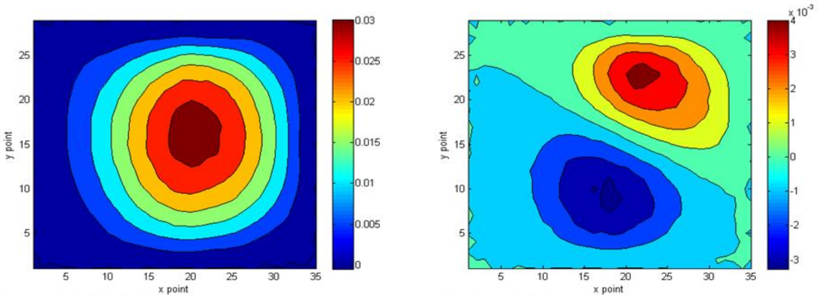

Mode 1-1 (66 Hz)   Mode 1-2 (144 Hz)

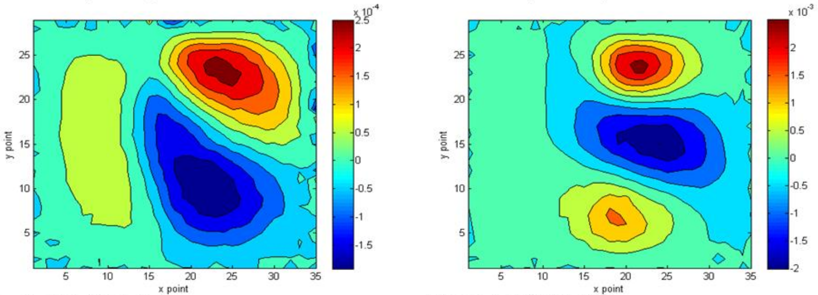

Mode 2-1 (186 Hz)   Mode 1-3 (216 Hz)

Figure 5.19. Measured mode shapes for the first four modes of vibration for the fluid-loaded foil under the effects of the horizontal splitter. Frequency indicates the natural frequency of the mode.

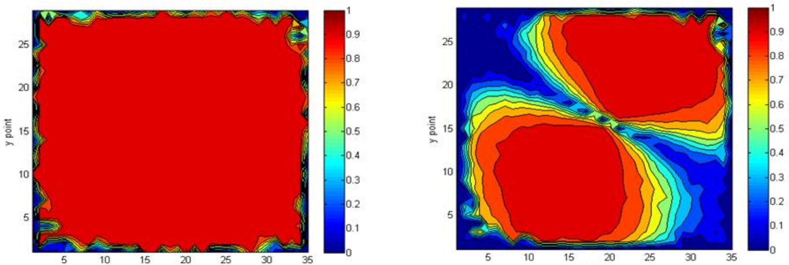

Mode 1-1 (66 Hz)   Mode 1-2 (144 Hz)

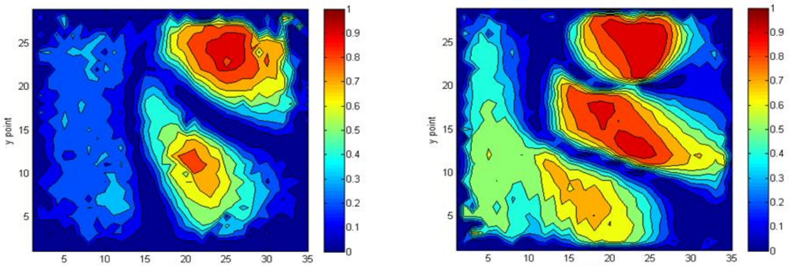

Mode 2-1 (186 Hz)   Mode 1-3 (216 Hz)

Figure 5.20. Measured coherence for the first four modes of vibration for the fluid-loaded foil under the effects of the horizontal splitter. Frequency indicates the natural frequency of the mode.

The fluid-loaded foil excited by spatially homogeneous forcing showed a decay in coherence as a function of position in Section 5.3. The cases of a fluid-loaded foil excited with a vertical or horizontal splitter show the same type of decay in coherence, though the coherence decay is far more severe when the horizontal splitter was used; such an effect was not observed for the case of the non-fluid-loaded plate excited with the vertical splitter. This shows that the spatial coherence decay is a constant aspect of the fluid loaded structure.

Comparison of Figures 5.13, 5.16, and 5.19 shows that the mode shapes of the fluid-loaded structure can be altered by the forcing field. For the case of the vertical splitter, the mode shapes for modes <1,1> and <2,1> are identical to those found when the structure was excited by a spatially homogeneous wall pressure. This is because the forcing is spatially homogeneous in the streamwise direction. However, modes <1,2> and <1,3> change when the vertical splitter is applied, with the magnitude of the peaks in the excited region being at least twice as large as the peaks in the unexcited region. This is because the wall pressure is non-homogeneous in the spanwise direction, so there is a spanwise variation in the mode shapes. In the case of the horizontal splitter, one observes a similar variation of mode shapes, except that the variation is even more severe. Such a forcing-dependent change in the mode shape was not observed to occur for the case of the non-fluid-loaded plate when excited by the vertical splitter.

The results shown here, where the mode shapes can vary depending on the forcing applied to the structure, are a potentially significant alteration to the prediction of the vibration of fluid-loaded structures. The current theories to predict such vibration assume that the mode shapes are completely dependent on the structural properties and do not account for the mode shapes being a function of the forcing applied to the structure. These experiments were an exploratory measure to determine if such an interaction existed; determination of a method to predict the vibration of a fluid loaded structure excited by spatially non-homogeneous forcing is beyond the scope of this thesis. A preliminary examination of the mode shapes presented in this section implies that it is probable that a simple model may not be able to predict the vibration of a fluid-loaded structure under the effects of non-homogeneous forcing. For example, the mode shapes under the case of streamwise and spanwise non-homogeneous forms of forcing look substantially different. Mode <1,2> when excited by a spanwise non-homogeneous forcing looks substantially different than mode <2,1> when excited by a streamwise non-homogeneous forcing.

5.5 Discussion: Explanation of the Change in Mode Shape Using a Discretized String Model

The purpose of this section is to provide an explanation of the physics which cause a fluid-loaded structure to vibrate with mode shapes that vary based on the spatial forcing characteristics. It will be shown that the underlying physics can be explained through the structure having high damping, which can be caused by fluid loading. To analytically model this, the equations of motion for a string will be discretized and solved numerically for high and low damping. Comparison of the experimental results with results from the discretized string model will show similar results, validating the underlying physics.

A string is the one-dimensional analog of a foil, as both structures lack bending stiffness. As was outlined in Section 2.1, the equation of motion for a string is

$$m_s\ddot{\xi} + C_d\dot{\xi} + L(\xi) = -p(\vec{y}, t) \quad , \qquad (5.1)$$

where

$$L(\xi) = T\frac{d^2\xi}{dx^2} \quad . \qquad (5.2)$$

The string was discretized into 100 discrete segments. The string was assumed to be homogeneous, such that mass, damping, and tension was equal for all points along the string. Mass and tension remained the same in all cases examined. Damping was changed on a case-by-case basis to examine the results of different levels of damping. The discretized string was not designed to be identical to the experiment. Instead, the damping was tuned until effects similar to what was observed in the experiment appeared in the model as well. This allows the model to show the underlying physics but not to function as an actual prediction.

In the discretized string model, forcing was assumed to be completely random with no coherence between forces spatially or temporally. While this is an extreme case (as all real systems will have temporal and spatial coherence over a small enough scale of either), it is relatively similar to that experienced by the structure in Chapter 3, where the wall pressure has a spatial correlation length scale much smaller than the size of the plate. Three different forcing models were used:

1) When **point-forcing** was utilized, it involved forcing the structure only on mass n=30. This was equivalent to random forcing of F_{30} while all other F_n=0 for n not

equal to 30. None of the experimental cases utilized point-forcing. However, point-forcing allows one to examine the response of one point to forcing at another point. This is instructive for understanding the coherence field of the structure under the effects of forcing over the full structure.

2) When **homogeneous** excitation was utilized, F_1 through F_{100} were all randomly excited with the same amplitude. This is similar to the experimental cases where a splitter was not used such that there was spatially-homogeneous excitation.

3) When "**split**" excitation was utilized, F_1 through F_{30} were excited randomly with amplitudes ten times that of F_{31} through F_{100}. This was meant to simulate the effects of what the splitter would look like while still allowing for a small amount of excitation in the "blocked" region.

Five different cases of forcing and damping were analyzed with the discretized string. These cases were in general examined because they mimic the experimental cases. Table 5.2 outlines the five cases examined. For these five cases, two primary results were examined: the mode shapes of the string and the coherence. Mode shapes of the structure were determined through the Principle of Orthogonal Decomposition. Coherence was taken relative to point 30 at a frequency corresponding to the natural frequency of mode 2. This point where coherence was taken relative to corresponds to the location where point forcing was applied or where the change in amplitude occurs for point and split forcing, respectively.

TABLE 5.2

FIVE CASES ANALYZED BY THE DISCRETIZED STRING

Case	Forcing	Damping	Purpose
1	Point	Low	Demonstrate the mode shapes of a “standard” structure. This corresponds to the experimental results of Chapter 4.
2	Split	Low	Demonstrate that any spatial characteristics of exciting a standard structure will result in standard mode shapes (as per normal modal analysis). This corresponds to the experimental results of Section 5.2.
3	Point	High	Demonstrate how high damping changes the mode shapes. There are no experimental cases to match this, but it allows one to observe why the coherence field for the fluid loaded structures has a spatial decay.
4	Homogeneous	High	Demonstrate that the homogeneous spatial excitation on a highly damped structure will result in mode shapes that appear homogeneous (symmetric) as well. This corresponds to the experimental results of Section 5.3.
5	Split	High	The true goal of the analysis; demonstrate that the non-homogeneous spatial excitation of a highly damped structure will result in the structure vibrating in altered mode-shapes. This corresponds to the experimental results of Section 5.4.

Case 1 is the discretized string with point forcing and low damping. This case corresponds to something similar to a ping-test on a non-fluid-loaded structure. The coherence for mode 2 and the first three mode shapes are shown in Figure 5.21. The coherence is equal to unity everywhere except at the node. The reason that the coherence is a nearly-constant unity is because all motion anywhere in the structure is induced by a single excitation. The exception to this is at the node. The vibration at the node is zero, so the coherence is equal to the limit of zero divided by zero (as both the auto-spectral density and cross-spectral density at this point are equal to zero), leading to an indeterminate value of coherence at the node. However, mathematically, coherence must be a value between 0 and 1, so “indeterminate” results in a more or less random number between 0 and 1. Compared to the coherence of unity everywhere else in the structure, this indeterminate value will appear as a drop-off in coherence. Lastly, the mode shapes here are the true mode shapes of the structure and are identical to the well-known mode shapes predicted by the theory of string vibration (specifically, sine functions).

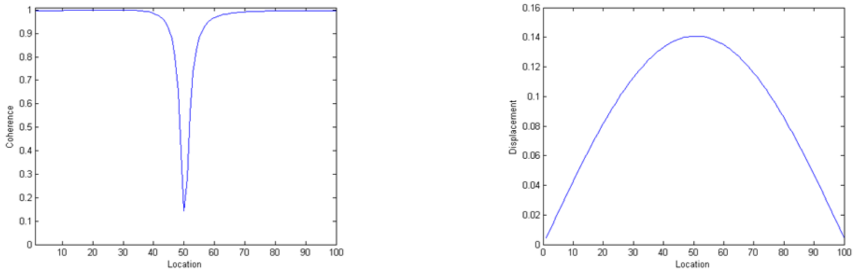

Coherence

Mode 1 Mode Shape

Mode 2 Mode Shape

Mode 3 Mode Shape

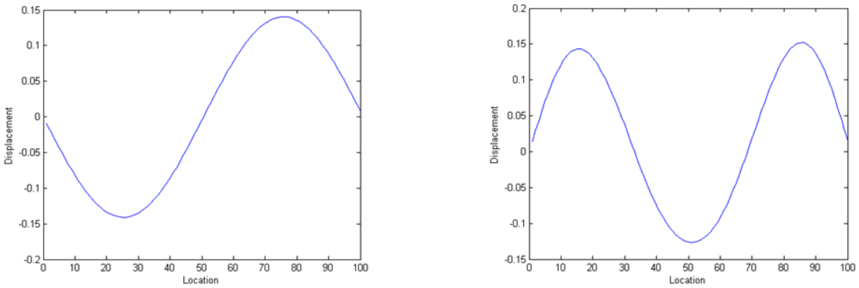

Figure 5.21. Coherence (for the frequency corresponding to mode 2) and first 3 mode shapes for discretized string case 1, a low-damped string excited by point forcing.

Case 2 is the discretized string with low damping excited by split forcing. The case of homogeneous excitation was skipped for brevity as the results of forcing a low-damped string with homogeneous or split forcing are identical. This case is the equivalent of the non-fluid-loaded plate whether it was excited with spatially homogeneous wall pressure or with spatially non-homogeneous wall pressure through use of the vertical splitter. The results for the discretized string for this case are shown in

Figure 5.22. The results look the same as in case 1, shown in Figure 5.21, but there are different implications behind these results.

The coherence field looks the same for both cases 1 and 2 but for different reasons. First, the vibration at the node location is still zero, so the coherence at this point is indeterminate. The coherence everywhere except the node is still unity. However, unlike the case of point forcing, the vibration of the structure is caused by numerous, completely uncorrelated forces rather than a single excitation, so it is no longer necessary to have unity coherence. The reason in this case for unity coherence is due to the low damping of the structure. Whenever a force is placed on the structure, a wave is generated that travels through the structure, rebounding when it reaches the boundary condition. Because of the low damping, the wave's amplitude decays slowly, such that an excitation at a single point in space and time results in a wave that travels across the length of the structure, reflecting off the boundary conditions when they are reached, a very large number of times before decaying. Because of this, a wave generated at any point in the structure will cause a response in any other point in the structure a very large number of times before the wave's amplitude decays to negligible value. The result is that no matter how the structure is excited, all points have nearly unity coherence relative to one another.

Lastly, the mode shapes for the low-damped string are the same both in the case of point forcing and split forcing. This result was expected as this is what is predicted by the well-established theories on string vibration. However, these results help to validate the model. Furthermore, this enforces the assertion that a structure at a natural frequency will vibrate with the mode shape corresponding to that frequency independent of the forcing method used.

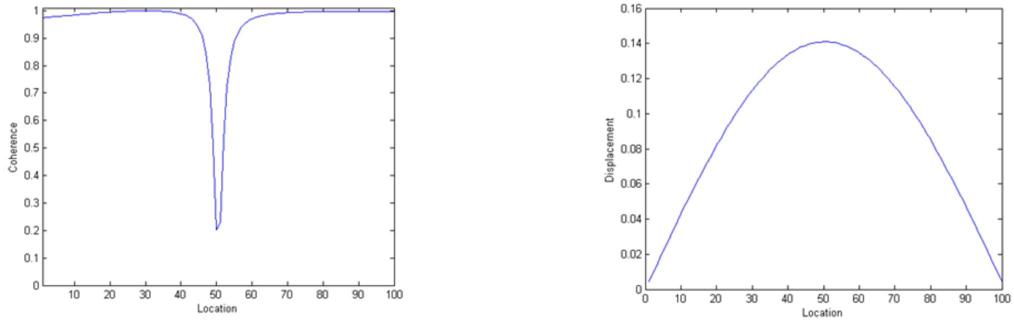

Coherence

Mode 1 Mode Shape

Mode 2 Mode Shape

Mode 3 Mode Shape

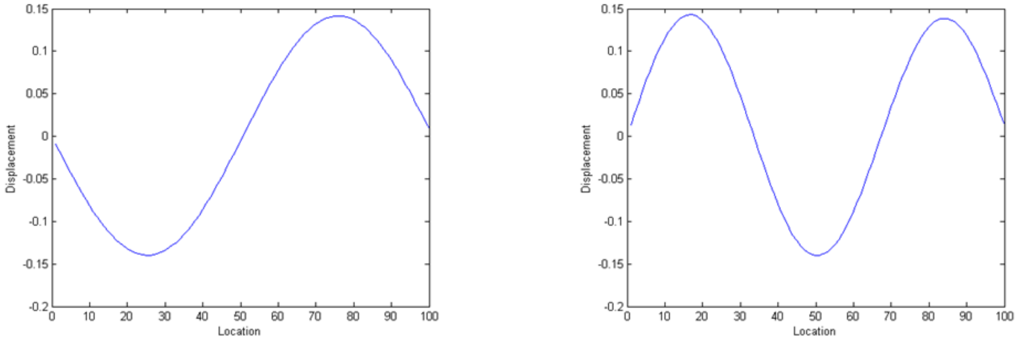

Figure 5.22. Coherence (for the frequency corresponding to mode 2) and first 3 mode shapes for discretized string case 2, a low-damped string excited by split forcing.

Case 3 is the discretized string with high damping excited by point forcing. The high-damping corresponds to the experimental case of the fluid-loaded foil, but the point forcing does not correspond to the forcing method used in any of the experiments. The coherence and first three mode shapes for this case can be seen in Figure 5.23. The damping of the structure is sufficiently high that the waves decay quickly as they travel within the structure. The result is that a wave will only interact with a limited portion of the structure before it decays substantially. This is different than the low damping case previously outlined, where a single wave interacts with each point in the structure numerous times (due to reflecting off the boundary conditions) before decaying significantly. As a result, the vibration of the highly damped structure begins to look closer to waves on an infinite string than waves on a bounded string. A wave may reflect off a boundary condition before significantly decaying, which differentiates it from an infinite string case, but the decay rate will be such that the wave's amplitude will be substantially lower before reflecting off a second boundary condition.

The effects of this decay can be seen in the modes shapes shown in Figure 5.23, where the amplitude of the mode in general decays as a function of spatial separation from the excitation point (point 30). While each mode retains some similarities to those of the low-damped system (for example, mode 2 still has 2 peaks), the mode shapes are substantially shifted. The peaks of these mode shapes have different magnitudes, as opposed to the low-damped string where the mode shapes have the same magnitude at each peak. The mode shapes are also shifted, with the highest peak of each mode occurring at point 30, the point of excitation. Because mode 3 has a node at this location for the low-damped case, this results in a substantial alteration of the mode shape for the high-damped string excited at this point. The coherence maintains a constant value of unity, but as discussed in case 1, this is due to the structure being excited by a single force.

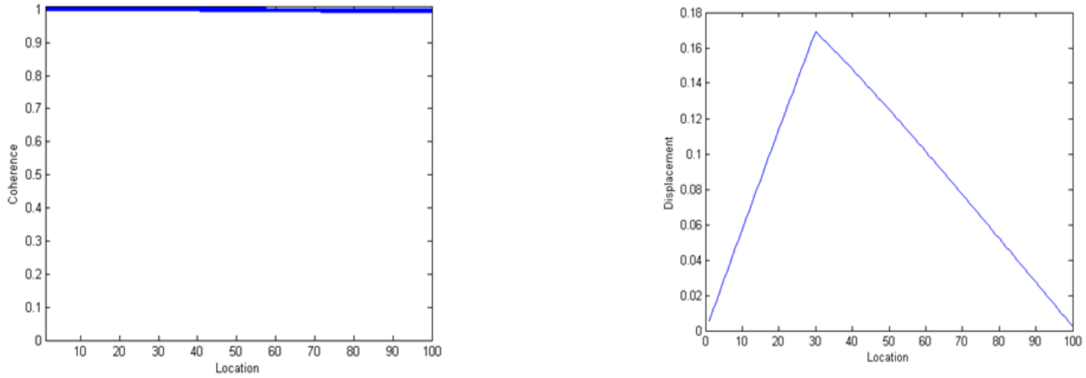

Coherence

Mode 1 Mode Shape

Mode 2 Mode Shape

Mode 3 Mode Shape

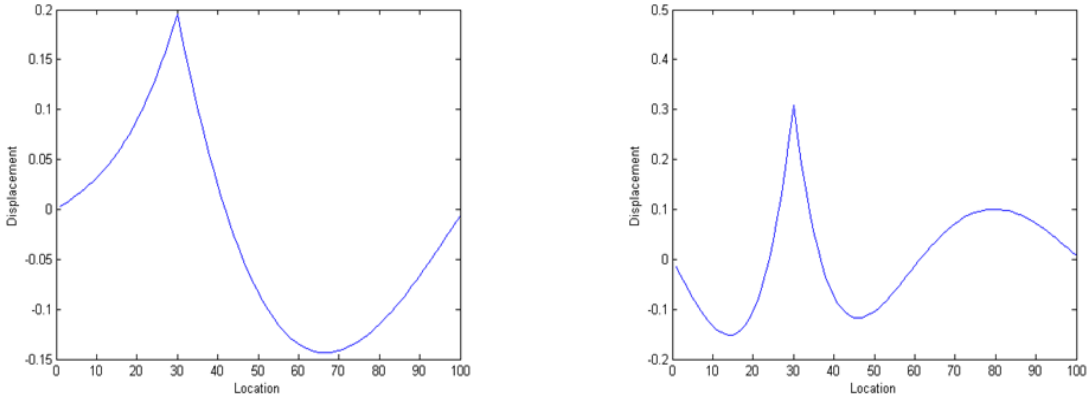

Figure 5.23. Coherence (for the frequency corresponding to mode 2) and first 3 mode shapes for discretized string case 3, a highly-damped string excited by point forcing.

Case 4 is the discretized string with high damping excited by homogeneous forcing. This corresponds to the experimental setup involving the fluid-loaded foil with spatially homogeneous forcing, which was examined in Section 5.3. The coherence and first 3 mode shapes for this case can be seen in Figure 5.24. The mode shapes appear identical to those found for all cases of the discretized string with low damping. The coherence looks substantially different, however, with a spatial-dependent decay in coherence. As noted in the previous case, the mode shape of a highly-damped string responding to point excitation is somewhat localized. When such point excitations occurs over the entire structure, as is the case with spatially homogeneous forcing, the result is that any given point is more strongly affected by forces spatially close to that point than points further away. This is different than the low-damped string, where a force at any location affects all locations similarly. This explains why there is a spatial decay in coherence.

The mode shapes are symmetric due to the spatially homogeneous forcing. Recall the mode shapes found for the case of point forcing on a highly-damped discretized string. Such mode shapes are skewed towards the point of excitation. If symmetric points on the structure are excited by statistically equal forcing, then the resulting vibration from the two excitations will be symmetric. Spatially homogeneous forcing is a series of statistically symmetrically-forced points. For this reason, while the resulting mode shapes may be the same for a highly-damped string excited by spatially homogeneous forcing and a low-damped string excited by split forcing, the underlying physics which causes these mode shapes is different for each case. The different coherence in these cases is an indication of the differences in the underlying physics for these cases.

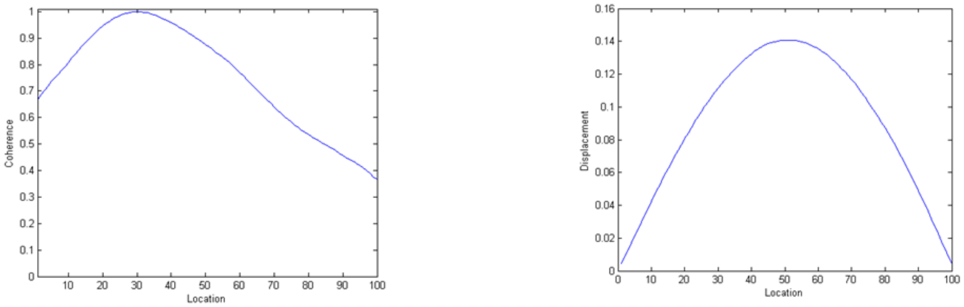

Coherence

Mode 1 Mode Shape

Mode 2 Mode Shape

Mode 3 Mode Shape

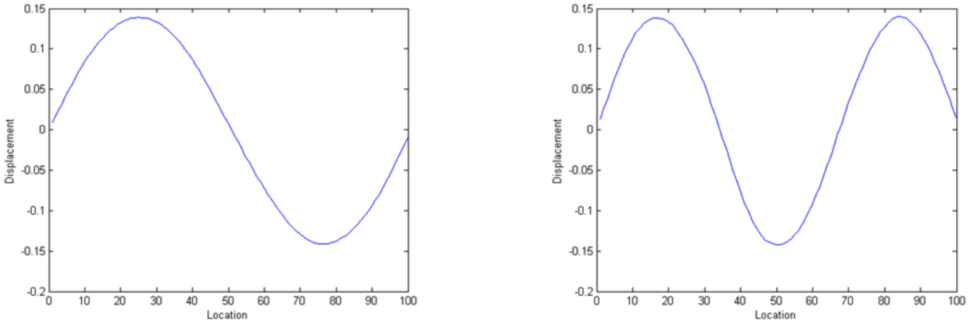

Figure 5.24. Coherence (for the frequency corresponding to mode 2) and first 3 mode shapes for discretized string case 4, a highly-damped string excited by homogeneous forcing.

Case 5 is the discretized string with high damping excited by split forcing and is the final case to be examined. Figure 5.25 shows the coherence and first 3 mode shapes for this case. The analyses of the previous cases lead into explaining these results. The coherence decays with spatial separation for the same reasons as the case of a highly-damped string excited by homogeneous forcing. Like the case of the highly-damped string with point forcing, the mode shapes are shifted towards the location with greater forcing. The explanations for these previous two cases combined explain the underlying physics which cause the shifting of the mode shapes observed under the effects of spatially non-homogeneous forcing of a fluid-loaded structure.

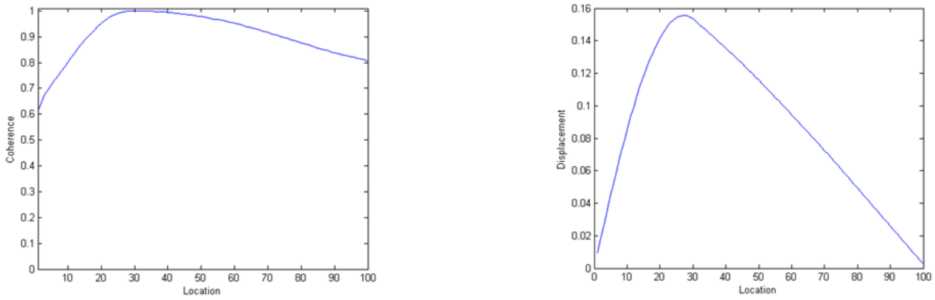

Coherence

Mode 1 Mode Shape

Mode 2 Mode Shape

Mode 3 Mode Shape

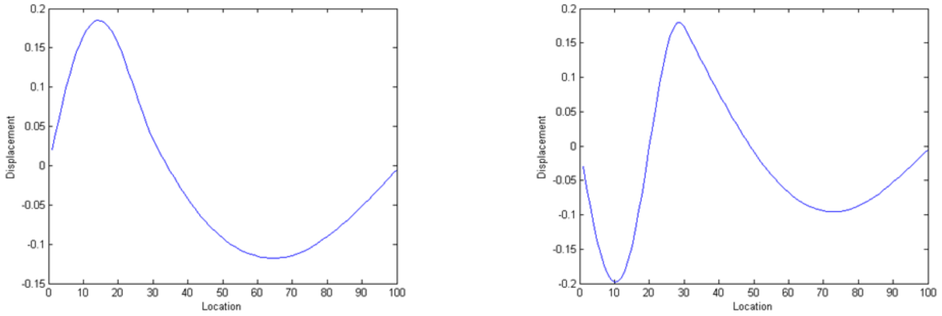

Figure 5.25. Coherence (for the frequency corresponding to mode 2) and first 3 mode shapes for discretized string case 5, a highly-damped string excited by split forcing.

The previous 5 cases mimic several of the experimental setups and lead up to explaining why the mode shapes of a fluid-loaded structure change under the influence of spatially non-homogeneous forcing. Figure 5.26 shows a comparison of the mode shape for mode 2 from two experimental cases and two of the discretized string cases. Figure 5.26 shows the mode shape of the low-damped string model under the effects of homogeneous forcing. This figure also shows a spanwise cross-section of the mode shape determined from the experiment involving the non-fluid-loaded plate under the effects of homogeneous forcing, as detailed in Chapter 4. These two mode shapes are the experimental and analytical analog of one another, and the mode shapes appear very similar to one another, with the mode shapes being symmetric.

Two other mode shapes are examined in Figure 5.26. The third mode shape in Figure 5.26 is that determined from the high-damping discretized string model under the effects of split forcing. The fourth curve in Figure 5.26 is the spanwise cross-section of the mode shape determined from the experiment involving the fluid-loaded foil under the effects of the vertical splitter forcing, as detailed in Section 5.3. These mode shapes are the analytical and experimental analog of one another, and while the mode shapes are not identical, they do appear similar to one another. In particular, there is a similar decrease in the amplitude of the mode shape in the region of the structure which is unexcited. The discretized string model is somewhat of an oversimplification of the experiment, and the parameters of the discretized string model were not tuned to be the same as those in the experiment. As a result, the discretized string model should not be considered a true prediction of the vibration of the fluid-loaded foil. The similar trends are meant to show that it can be considered an explanation of the underlying physics.

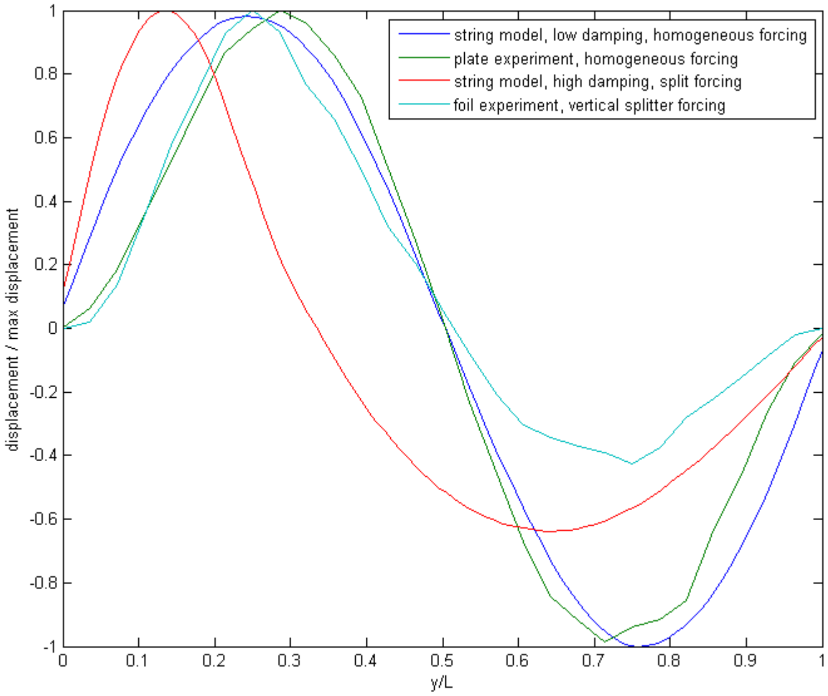

Figure 5.26. Y-trace of the mode shapes of two experimental cases and two of the discretized string cases at mode 2.

5.6 Chapter Conclusion

This chapter combined with Chapter 4 examined four unique structural cases, involving non-fluid-loaded and fluid-loaded structures excited by spatially homogeneously and spatially non-homogeneously. As expected by established theory, non-fluid-loaded structures maintain similar mode shapes regardless of the method by which they are excited. Fluid-loaded structures when excited in a spatially homogeneous method exhibit mode shapes which look similar to those of the non-fluid-loaded structures, though the change in the spatial coherence indicates the underlying physics which generate these mode shapes may be different.

When a fluid-loaded structure is excited in a spatially non-homogeneous method, the mode shapes change based on the forcing field. A discretized string model was used to show that this is likely caused by the increased damping of the structure. The work done here was an exploratory effort to determine if such a relationship existed; generation of a reliable method of solving such a system is beyond the scope of this work. However, these results have important implications for fluid-loaded structures. Modal analysis in general assumes mode shapes that are not dependent on the forcing function of the system. As these results show at least some relationship between the forcing function and the mode shapes, such modal analysis should be used with caution on fluid-loaded structures. Furthermore, because the resulting vibration is spatially asymmetric, systems under these conditions may become far more efficient acoustic radiators

CHAPTER 6

INTERNAL ACOUSTIC SPECTRA OF A ROTOR WITHIN A DUCT OF FINITE LENGTH

The internal pressure spectra of a ducted rotor can be divided into two sources: hydrodynamic and acoustic. The hydrodynamic pressure consists of those generated by the turbulent boundary layer along the duct wall. This chapter will focus solely on the acoustics generated by the rotor. Results reported in this chapter are largely the work of the author of this thesis based on prior work by Stephens and Morris [12] and Stephens et al. [13].

The complete pressure field internal to a duct due to a rotor is the summation of the acoustic and hydrodynamic pressure fields; however, pending the specific geometry of the system, the acoustics and hydrodynamics may or may not interact in a significant way. The duct acoustics are basically non-existent below a specific frequency, known as the "cut-on" frequency, whereas the hydrodynamic pressure spectra tends to decay with increasing frequency. Thus, in some cases the hydrodynamics may be relatively negligible at the frequencies for which the acoustics are cut on.

The problem at hand involves a low Mach number rotor driving an axial flow through a duct which creates an acoustic pressure field by means of the unsteady aerodynamic forces on the rotor blades. As discussed in Chapter 2, the sound is primarily generated by elongated turbulent eddies passing through the rotor; these eddies are sufficiently long that multiple rotor blades pass through the turbulent structure before it finishes convecting through the rotor. The interaction of the rotor blade with the eddy generates an unsteady force on the blade, creating a sound source which is dipole-like in nature; this is the same acoustic source assumed in the modeling of flow noise, as outlined by the work of Stephens and Morris [12] and Stephens et al [13].

6.1 Theoretical Background on the Acoustic Pressure Spectra for a Ducted Rotor

If one assumes all acoustics in the duct are harmonic, then the governing equation for the acoustics in the duct is given by the harmonic Helmholtz equation as

$$(k^2 + \nabla^2)p = 0\,. \tag{6.1}$$

For a rigid-walled infinite duct with low Mach number flow, the solution to Equation (6.1) is given by the Green's function

$$G = \frac{e^{ik\cdot|x-x_0|}}{2i\pi a^2 k} + \sum_{m=0}^{\infty}\sum_{n=1}^{\infty} \epsilon \frac{J_m\left(\mu_{mn}\frac{r}{a}\right)J_m\left(\mu_{mn}\frac{r_0}{a}\right)}{i\sigma'_{mn}\alpha_{mn}} (\cos m(\theta-\theta_0))\left(e^{i\alpha_{mn}\cdot|x-x_0|}\right)\ , \tag{6.2}$$

as given by Morse and Ingard [18]. Equation (6.2) represents the Green’s function for a monopole within an infinite duct.

The acoustic pressure at an observer location due to dipole forces distributed over the volume of the duct is given by Pierce [49] as

$$p(\vec{r}) = \iiint_V \vec{F}(\vec{r_0}) \cdot \nabla_0 g(\vec{r},\vec{r_0}) dV_0 = \iiint_V |F(\vec{r_0})|\, \hat{n} \cdot \nabla_0 g(\vec{r},\vec{r_0}) dV_0\ , \tag{6.3}$$

where $\hat{n}$ is the unit vector in the direction of the dipole force. In the present case the Mach number is assumed small and is not included in the acoustic propagation. Stephens and Morris [50] demonstrated that Equation (6.3) is an acceptable assumption for understanding the radiation of sound outside of the duct. The work of this chapter will focus on the circumferential mode amplitudes in the duct's interior.

Equation (6.3) can be converted to a form involving the integration of the product of two scalar quantities by defining the dipole transfer function as

$$T_{dipole} = \hat{n}(\overrightarrow{r_0}) \cdot \nabla_0 g(\vec{r}, \overrightarrow{r_0}) \qquad , \qquad (6.4)$$

which allows the resulting pressure to be written as

$$p(\vec{r}) = \iiint_V |F(\overrightarrow{r_0})|\, T_{dipole}(\vec{r}, \overrightarrow{r_0}) dV_0 \qquad . \qquad (6.5)$$

If one defines a coordinate system such that x-x_0 is non-negative, then the transfer function for a dipole in a rigid circular duct is given by

$$T_{dipole} \equiv \frac{dG}{dx_0} \cos\varphi + \frac{1}{r_0} \frac{dG}{d\theta_0} \sin\varphi \qquad , \qquad (6.6)$$

where

$$\frac{dG}{dx_0} = \frac{e^{ik\cdot(x-x_0)}}{2\pi a^2} + \sum_{m=0}^{\infty} \sum_{n=1}^{\infty} \varepsilon_d \frac{J_m\left(\mu_{mn}\frac{r}{a}\right) J_m\left(\mu_{mn}\frac{r_0}{a}\right)}{\sigma'_{mn}} \left(\cos\left(m \cdot (\theta - \theta_0)\right)\right)\left(e^{i\alpha_{mn}\cdot(x-x_0)}\right) \qquad (6.7)$$

and

$$\frac{dG}{d\theta_0} = \sum_{m=0}^{\infty} \sum_{n=1}^{\infty} \varepsilon_d \frac{m J_m\left(\mu_{mn}\frac{r}{a}\right) J_m\left(\mu_{mn}\frac{r_0}{a}\right)}{i\sigma'_{mn}\alpha_{mn}} \left(\sin\left(m \cdot (\theta - \theta_0)\right)\right)\left(e^{i\alpha_{mn}\cdot(x-x_0)}\right) \qquad . \qquad (6.8)$$

Here the following terminology is used:

- x, r, and θ are the axial, radial, and circumferential location (respectively) of the observer
- x_0, r_0, and θ_0 are the axial, radial, and circumferential location (respectively) of the source
- φ is the direction of the dipole, which for this particular setup is the rotor blade stagger angle
- m, while mathematically simply an index for use in the summation, is physically representative of the circumferential mode number
- n, while mathematically simply an index for use in the summation, is physically representative of the radial mode number
- ε_d is equal to ½ for m=0 and equal to 1 otherwise (this represents the fact that m technically needs to be summed from -∞ to ∞ but that Equation (6.7) and Equation (6.8) are even functions with respect to m).
- J_m is a Bessel function of the first kind.
- μ_{mn} is a zero of derivative of Bessel function, defined such that $J'_m(\mu_{mn})=0$, where n represents the n-th zero of this function for a fixed m.
- k is the wave number, defined as $k=\omega/c_0$, with c_0 being the speed of sound in the fluid medium, and in this system effectively is simply a value that represents frequency.
- a is the radius of the duct.

- α_{mn} is another way of representing the frequency in a mode-dependent way such that it is zero when the acoustics of mode <*m*,*n*> first become active and is defined as

$$\alpha_{mn} = \sqrt{\left(\frac{\omega}{c_0}\right)^2 - \left(\frac{\mu_{mn}}{a}\right)^2} \quad . \tag{6.9}$$

- σ'_{mn} is a function which determines the broadband magnitude of a given mode and is defined as

$$\sigma'_{mn} = \pi a^2 \left(1 - \frac{m^2}{{\mu_{mn}}^2}\right) {J_m}^2(\mu_{mn}) \quad . \tag{6.10}$$

Equation (6.6) is the result of taking the dot product of the Green's function for a dipole with the direction of the dipole force, while Equation (6.7) and Equation (6.8) are the axial and circumferential components of the ducted dipole transfer function, respectively. The total transfer function is a combination of these two effects, and the relative magnitudes of these factors are dependent on the direction of the dipole force. In theory one should include the radial component of the dipole in these calculations as well. However, the mechanics by which a rotor generates sound effectively guarantees that there will be no radial component for a rotor whose axis is aligned with the axis of the duct, so such calculations are neglected here. In Equation (6.7), the term outside the summation represents a plane wave, which corresponds to mode <0,0>. All terms in the summations of Equation (6.7) and Equation (6.8) contain modal components in the radial and/or circumferential directions.

With the exception of the plane wave term, α_{mn} is the only frequency-dependent value in this expression. Whenever α_{mn} is imaginary, one will find that the exponential term in Equation (6.7) and Equation (6.8) decays relatively quickly with axial location.

Thus, in the far-field, mode-frequency combinations for which α_{mn} is imaginary are referred to as being "cut off". For a given <*m*,*n*>, the frequency at which α_{mn} is equal to zero is referred to as either the "cut-on" or "cut-off" frequency. Frequencies above this will result in purely real values of α_{mn}, in which case the final exponential term in Equation (6.7) and Equation (6.8) maintains a constant magnitude and only varies in phase. For a fixed <*m*,*n*> mode, for increasing frequency the axial component of the dipole appears as a step function, jumping from zero below the cut-on frequency to a fixed magnitude above the cut-on frequency, though the phase will still vary with frequency. The magnitude of the circumferential dipole exhibits a $1/\alpha_{mn}$ response centered at the cut-on frequency, spiking to an infinitely large magnitude at the cut-on frequency and quickly decaying for increasing frequency.

Using the transfer function for a dipole within a duct, the next step is to derive a transfer function for the rotor itself. In a general sense, one would need to fill the entire volume of the duct with a distribution of dipoles to predict the response. However, as discussed in Chapter 2, the primary source of sound for a rotor within a duct is caused by the interaction of the rotor blade tip region with the casing turbulent boundary layer. If one assumes that the properties affecting the magnitude of the forces on the blade are relatively constant within this region and that the dipoles generated by these forces can be considered axially compact, then the net effect can be approximated as a ring of dipoles compact in both the axial and radial directions. Specifically, the ring was approximated as being located at $r_0=0.95a$ based on previous measurements related to the size of the turbulent boundary layer and the tip clearance of the rotor.

Because Equation (6.6) is linear, this ring of dipoles can be decomposed into a series of independent rings at the same spatial location, each of which represents a single circumferential mode oscillating at a single frequency. Because the duct is axisymmetric, the strength of each mode must be constant and independent of circumferential location, but the phase of oscillation can vary along the ring. For a particular mode and frequency, the time phase of oscillation can be expressed as

$$\psi_M(\omega) = M\theta_0 + \psi_{M0}(\omega) \quad , \qquad (6.11)$$

where ψ_{M0} is some arbitrary shift based on the where time and location is selected as the reference, and M is the circumferential mode number. Thus, for a single mode, the force concentration can be written as

$$\frac{d\mathcal{F}_{M0}(x_0,r_0,\theta_0,\omega)}{d\theta_0} = \frac{F_{M0}(\omega)}{2\pi} e^{i(M_0\theta_0+\psi_{M0}(\omega))} \quad . \qquad (6.12)$$

F_{M0} is a representation of the magnitude of the force of the ring whereas the exponential is a constant-magnitude expression that expresses the phase of each location along the ring. To gain a more physical interpretation of F_{M0}, one can examine the case of M=0, for which all forces are in phase. Integrating Equation (6.12) around the ring for this case one obtains

$$\left|\int_0^{2\pi} \frac{d\mathcal{F}_{M0}(x_0,r_0,\theta_0,\omega)}{d\theta_0} d\theta\right| = \left|\int_0^{2\pi} \frac{F_{M0}(\omega)}{2\pi} e^{i(\psi_{M0}(\omega))} d\theta\right| = F_{M0}(\omega) \quad . \quad (6.13)$$

Thus, one sees that for mode M=0, F_{M0} is the dipole force if the entire rotor were considered a compact source at the center of the rotor. While there is a value of F_{M0} for any mode M, the physical interpretation cannot be directly applied to modes above M=0;

the integration performed in Equation (6.13) will result in a value of zero for all non-zero modes.

With this in mind, the pressure generated by the dipole ring can be expressed as

$$P(\omega) =$$

$$\sum_{M_0=-\infty}^{+\infty} \int_0^{2\pi} \int_0^{a} \int_{-\infty}^{+\infty} \frac{d\mathcal{F}_{M0}(x_0,r_0,\theta_0,\omega)}{d\theta_0} T_{dipole}\delta(r_0 - r_{source})\delta(x_0 - x_{source})\, dx_0\ dr_0\, d\theta_0$$

$$= \sum_{M_0=-\infty}^{+\infty} \int_0^{2\pi} \frac{d\mathcal{F}_{M_0}(x_0,r_0,\theta_0,\omega)}{d\theta_0} T_{dipole} d\theta_0 \quad . \qquad (6.14)$$

Recognize that Equation (6.14) is effectively a triple summation due to the summation of the *m* and *n* terms contained within the expression of T_{dipole}. However, due to the orthogonality of the sine and cosine functions with respect to θ_0 found in both the force concentration and the dipole transfer function, only values of $M=m$ will result in a non-zero integral in Equation (6.14).

This simplifies the expression in several ways. First, all instances of *M* can be replaced with *m* and the summation over *M* can be removed. It also implies that a dipole ring of mode *m* excites a pressure response only of mode *m*. Because of this decoupling of the modes, the value of ψ_{m0} will have no effect on the magnitude of the response and will only change the overall phase of the response. Because in a statistically stationary system one phase is arbitrary, ψ_{m0} can be set to an arbitrary value without changing the final results; for simplicity ψ_{m0} is set to zero.

The decoupling of the modes also places a practical limitation on the number of values of *m* which must be accounted for at a given frequency. At any particular frequency, there is no need to include values of *m* for which the lowest cut-on frequency is larger than the frequency of interest. With this in mind, one can now express the radiated pressure of a single circumferential mode based on a transfer function for the rotor itself as

$$|P_m(\omega)| = F_{m_0}(\omega)\left|T_{rotor,m}(\omega)\right| \qquad , \tag{6.15}$$

where

$$T_{rotor,m}(\omega) \equiv \int_0^{2\pi} e^{i(m\theta_0)} \Bigg\{ \Bigg[\frac{e^{ik\cdot(x-x_0)}}{2\pi a^2} + \sum_{n=1}^{\infty} \epsilon \frac{J_m\left(\mu_{mn}\frac{r}{a}\right) J_m\left(\mu_{mn}\frac{r_0}{a}\right)}{\sigma'_{mn}} \left(\cos\left(m(\theta-\theta_0)\right)\right)\left(e^{i\alpha_{mn}\cdot(x-x_0)}\right) \Bigg] r_0 \cos\varphi + \Bigg[\sum_{m=0}^{\infty} \sum_{n=1}^{\infty} \epsilon \frac{m J_m\left(\mu_{mn}\frac{r}{a}\right) J_m\left(\mu_{mn}\frac{r_0}{a}\right)}{i\sigma'_{mn}\alpha_{mn}} \left(\sin\left(m(\theta-\theta_0)\right)\right)\left(e^{i\alpha_{mn}\cdot(x-x_0)}\right) \Bigg] \sin\varphi \Bigg\} d\theta_0 \quad . \tag{6.16}$$

Note that $T_{rotor,m}$ is defined as a unique rotor transfer function for each circumferential mode m. Here, the $\cos\varphi$ term corresponds to the axial contribution of the dipole while the $\sin\varphi$ term corresponds to the tangential contribution of the dipole, which can be easily verified by setting $\varphi = 0^0$ (axial alignment of the dipole) or $\varphi = 90^0$ (tangential alignment of the dipole). For a known duct geometry, the only unknown in Equation (6.15) and Equation (6.16) is the forcing value F_{m0} for each mode. Equation (6.17) can be further simplified by carrying out the integration, resulting in

$$\left|T_{rotor,m}(\omega)\right| = magnitude \Bigg\{ \Bigg[\left[\frac{e^{ik\cdot(x-x_0)}}{a^2} \right]_{if\ m=0} r_0 \cos\varphi + \sum_{m=0}^{\infty} \sum_{n=1}^{\infty} \epsilon \frac{J_m\left(\mu_{mn}\frac{r}{a}\right) J_m\left(\mu_{mn}\frac{r_0}{a}\right)}{\sigma'_{mn}} \pi(\cos(m\theta) + i\sin(m\theta))\left(e^{i\alpha_{mn}\cdot(x-x_0)}\right) \Bigg] r_0 \cos\varphi + \Bigg[\sum_{m=1}^{\infty} \sum_{n=1}^{\infty} \epsilon \frac{m J_m\left(\mu_{mn}\frac{r}{a}\right) J_m\left(\mu_{mn}\frac{r_0}{a}\right)}{i\sigma'_{mn}\alpha_{mn}} \pi(\sin(m\theta) - i\cos(m\theta))\left(e^{i\alpha_{mn}\cdot(x-x_0)}\right) \Bigg] \sin\varphi \Bigg\} \quad . \tag{6.17}$$

When the complex terms inside the magnitude function are simplified, this becomes

$$\left|T_{rotor,m}(\omega)\right| = magnitude\left\{\left[\frac{e^{ik\cdot(x-x_0)}}{a^2}\right]_{if\ m=0} r_0\cos\varphi + \sum_{m=0}^{\infty}\sum_{n=1}^{\infty}\epsilon\frac{J_m\left(\mu_{mn}\frac{r}{a}\right)J_m\left(\mu_{mn}\frac{r_0}{a}\right)}{\sigma'_{mn}}\pi\left(e^{i\alpha_{mn}\cdot(x-x_0)}\right)\left[(\cos(m\theta)+i\sin(m\theta))r_0\cos\varphi + \frac{m}{i\alpha_{mn}}(\sin(m\theta)-i\cos(m\theta))\sin\varphi\right]\right\} \quad . \tag{6.18}$$

Because the system is statistically stationary, one phase per mode is arbitrary (as the modes are decoupled). However, the phase is unchanged for varying radial modes, and as such, the entire phase of each circumferential mode is arbitrary. Thus, in a practical sense it is the magnitude of Equation (6.18) that is desired. Because the duct is axisymmetric, the response will have the same magnitude at all angles. The magnitude can be more easily expressed by examining Equation (6.18) for θ=0, which yields

$$\left|T_{rotor,m}(\omega)\right| = magnitude\left\{\left[\frac{e^{ik\cdot(x-x_0)}}{a^2}\right]_{if\ m=0} r_0\cos\varphi + \sum_{m=0}^{\infty}\sum_{n=1}^{\infty}\epsilon\frac{J_m\left(\mu_{mn}\frac{r}{a}\right)J_m\left(\mu_{mn}\frac{r_0}{a}\right)}{\sigma'_{mn}}\pi\left(e^{i\alpha_{mn}\cdot(x-x_0)}\right)\left(r_0\cos\varphi - \frac{m}{\alpha_{mn}}\sin\varphi\right)\right\} \quad . \tag{6.19}$$

Equation (6.19) is the final form of the rotor transfer function utilized in Equation (6.15). Varying the blade stagger angle will affect the relative magnitudes of the axial and circumferential components of the dipole transfer function, with Equation (6.19) being a summation of these two effects. Also note for a mode that is cut on that the magnitude of the rotor transfer function will not change with axial location, though the phase will.

Figure 6.1 shows the axial and tangential rotor transfer functions for circumferential mode 1 (m=1) for a duct with the same characteristics as the experiment but of infinite length. The only frequency dependence occurs in the α_{mn} term, which is also a function of the <*m*,*n*> mode and the radius of the duct, which is a fixed quantity. When α_{mn} is imaginary (which will occur for low frequencies), then the <*m*,*n*> mode is cut off and acoustics do not propagate through the duct at this mode. When α_{mn} is real, then the <*m*,*n*> mode is cut on. These are the same characteristics that are present in the response for a single dipole.

In Figure 6.1, three radial cut-ons can be seen at 989 Hz, 2865 Hz, and 4587 Hz, corresponding to radial modes n=1, n=2, and n=3. As a function of frequency, axial dipoles for a single <*m*,*n*> mode cut on like a step function, changing from effectively a value of zero below the cut-on to some constant, non-zero, finite value above the cut-on. For tangential dipoles at a single <*m*,*n*> mode the transfer function still has a value of zero below cut on, but at the cut-on frequency the acoustic signal becomes infinitely large, then very quickly rolls off as $1/\ \alpha_{mn}$. The net result of this is that for a rotor with both axial and tangential components, the tangential dipole will tend to dominate the response near a cut-on frequency and the axial dipole will tend to determine the value that the <*m*,*n*> mode approaches as frequency increases. These cut-on characteristics for a single <*m*,*n*> mode can be seen in Figure 6.1 between 989 Hz and 2865 Hz, during which only the <1,1> mode has cut on.

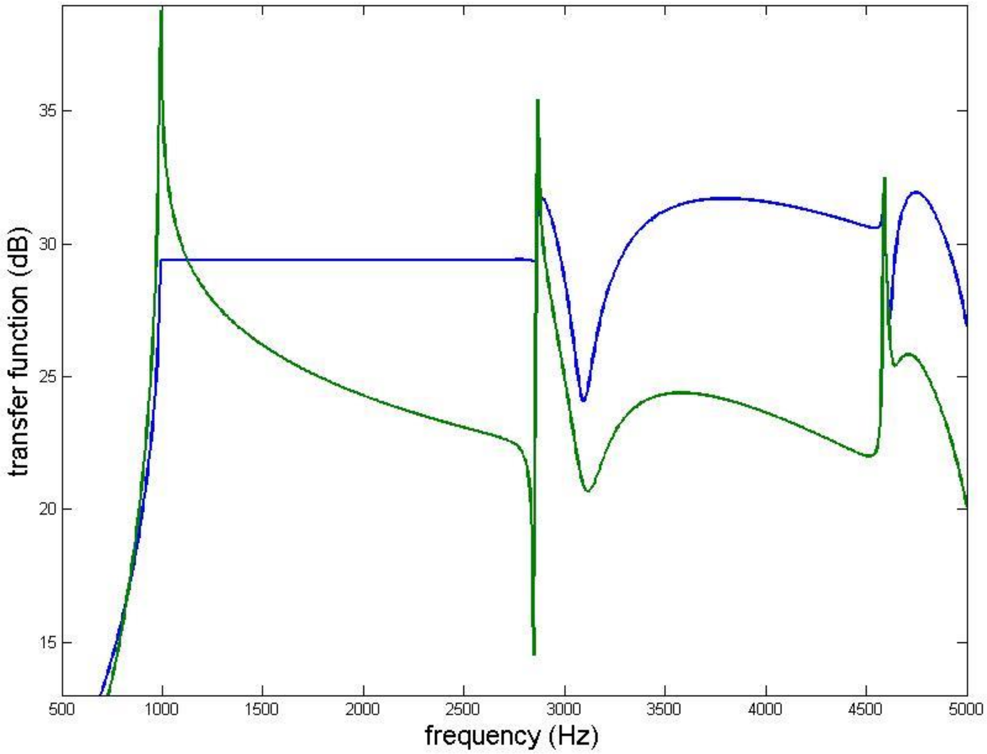

Figure 6.1. Transfer function for an axially-aligned dipole (blue) and a tangentially-aligned dipole (green) for the duct seen in the experiment but of infinite length.

Above 2865 Hz, Figure 6.1 does not at first appear to obey the rules stated for axial and tangential dipoles; this is due to interference between multiple radial modes. First, recall that circumferential modes cannot interact with one another, so these interference patterns cannot occur for a single rotor in an infinite duct until at least two radial modes are present. Independently, each radial mode still follows the rules previously outlined. However, the phase of each of the radial modes is dependent on $\alpha_{mn}\bullet(x-x_0)$. For a fixed location and circumferential mode in the duct, the phase of the pressure spectra is only dependent on α_{mn}, but both α_{mn} and $d\alpha_{mn}/df$ vary with n and f. Thus, both the phase and the rate of change of the phase with respect to frequency will vary differently for each radial mode. This means that the rings of pressure spectra generated by different radial mode will move in and out of phase with one another as frequency is varied. This is why the Figure 6.1 shows fluctuations with frequency after the second and third cut-ons even though individually each mode has a fairly smooth dependence on frequency. After the third cut-on, the fluctuations become even more severe as there are active more modes to move in and out of phase of one another.

Because the phase is dependent on the product $\alpha_{mn} \bullet (x-x_0)$, the specific axial location in the duct will also determine how quickly the phase changes, though these interference patterns will exist in some fashion regardless of location. Furthermore, if one examines the equation for α_{mn}, one will observe that $d\alpha_{mn}/df$ is extremely large near the $<m,n>$ cut-on, meaning that the fluctuations will occur over much smaller frequency scales near cut-on and then occur over large frequency scales away from the cut-on; this can also be seen in Figure 6.1.

Up to this point, all analytics were derived for an infinitely long duct. Both the inlet and exit of the duct will appear as some combination of a pressure release and rigid wall boundary condition. This boundary condition can be enforced in the model through use of a method of images by creating one image rotor for the inlet and one image rotor for the exit. The image rotor created by the reflection across the exit then must be reflected across the inlet, while the image created by the reflection across the inlet must be reflected across the exit. This process repeats for each new set of image rotors, creating an infinite string of image rotors required to simulate the boundary condition. Recall that the magnitude of the response of a rotor is not dependent on distance; thus, one cannot neglect a certain tier of image rotors simply due to being a large distance from the observer location. However, if the reflection coefficient has a magnitude less than one, which is a practical assumption for the inlet/exit of a duct, then each additional tier of image rotors will have decreasing strengths. The number of tiers of image rotors required to be modeled is dependent on when the strength of the image rotor is small enough to be negligible due to the decrease in strength caused by the reflection coefficient. For reflection coefficients only moderately less than one, this can potentially be a slowly converging process.

Figure 6.2 shows the transfer function for circumferential mode 1 for an infinite duct, a finite duct with 1 tier of image rotors, and a finite duct with 3 tiers of image rotors. For the finite duct cases, one can observe fluctuations in the transfer functions over relatively small changes in frequencies. These are interference patterns caused by a mechanism that is similar to how two radial modes of a single rotor cause interference patterns. Recall that the phase of a particular mode for a single rotor is given by $\alpha_{mn} \bullet (x-x_0)$. α_{mn} does not vary between each of the rotors (including both the real rotor and the image rotors). However, even for only a single radial mode, each rotor will have a different value of $x-x_0$ due to being located at different axial locations, which results in the same interference pattern mechanism found in the case of a single rotor with multiple radial modes. Unlike the case of a single rotor, these fluctuations occur even with only one radial mode cut on, as can be seen from 950 Hz to 2850 Hz in Figure 6.2, which corresponds to the first radial mode of circumferential mode 1. Furthermore, by comparing the cases of 1 tier of image rotors and 3 tiers of image rotors, one observes that adding more tiers adds additional fluctuations that are smaller in magnitude and occur over smaller frequency scales. The smaller magnitudes are due to the reflection coefficient reducing the strength of the image rotors on these additional tiers. The smaller frequency scales are due to the increase value of x-x_0 associated with each tier of rotor; this results in a more rapidly changing phase, and thus the signals move in and out of phase over smaller changes in frequency.

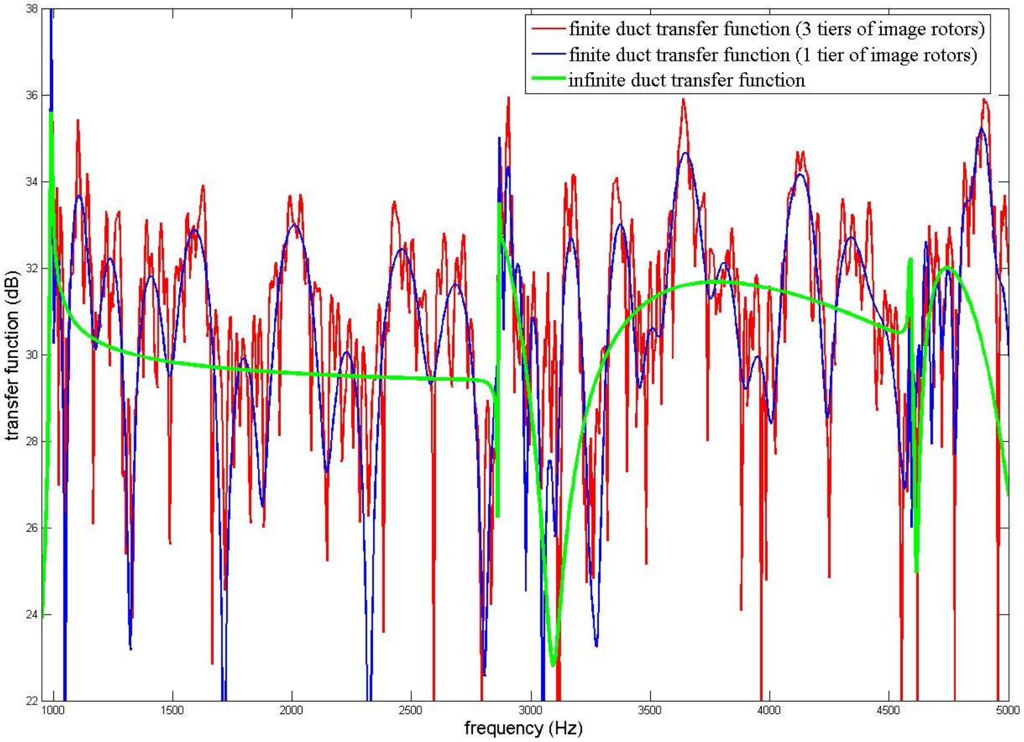

Figure 6.2. Transfer function for mode 1 for infinite duct, finite duct with 1 tier of image rotors, and 3 tiers of image rotors assuming the conditions found in the experiment.

A second effect of the interference patterns created by the image sources is that the transfer function becomes much more sensitive to changes in the axial location of the observer as shown in Figure 6.3. The basic pattern of the transfer function is relatively unaffected by the shift in the observer, but the exact locations of the peaks and troughs of the interference patterns can shift. At any specific frequency, the strength of the transfer function can be changed dramatically due to small changes in the axial location of either the source or the observer. Similarly, changes in the length of the duct can elicit similar changes as this will change the location of the image rotors. The shifts become more severe as the frequency increases higher above the cut-on frequency; this effect is visible in Figure 6.3.

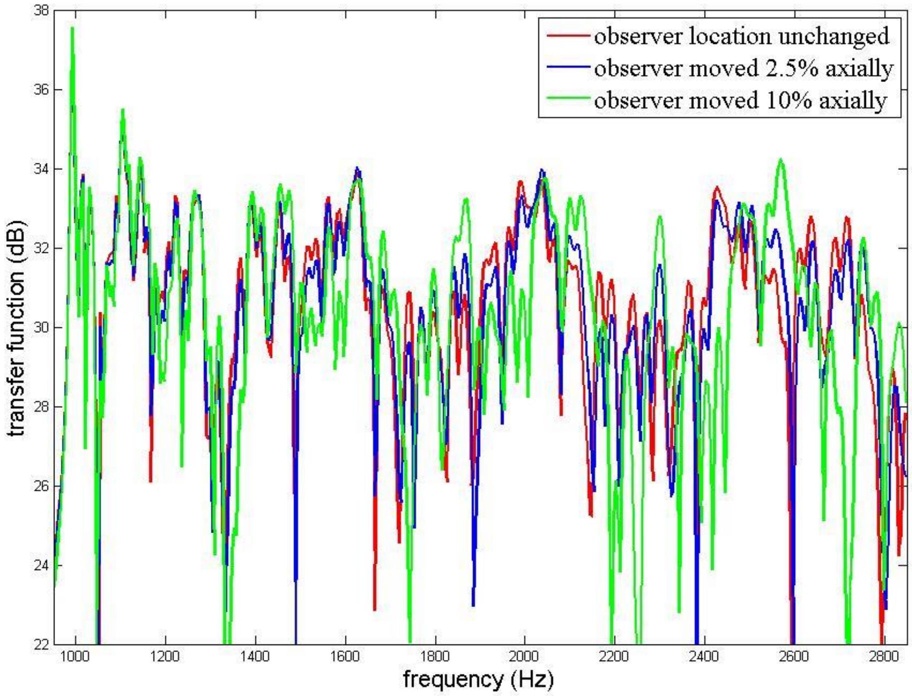

Figure 6.3. Transfer function for mode <1,1> as the observer is moved 2.5% and 10% assuming the conditions found in the experiment.

To this point, examples have been primarily examined for circumferential mode 1. The reason for this is simply because circumferential mode 1 is active at lower frequencies than higher modes, and as such, it is easier to view the effects of multiple radial modes by looking at circumferential mode 1. However, the effects demonstrated for circumferential mode 1 applies to all circumferential modes.

6.2 Wall Pressure Measurements

Far-field acoustic measurements were obtained by placing a using Bruel & Kjaer 6.35mm capacitance based microphone on-axis outside of the duct. Figure 6.4 shows the measurements obtained from the far-field measurement at a rotor speed of 4000 rpm.

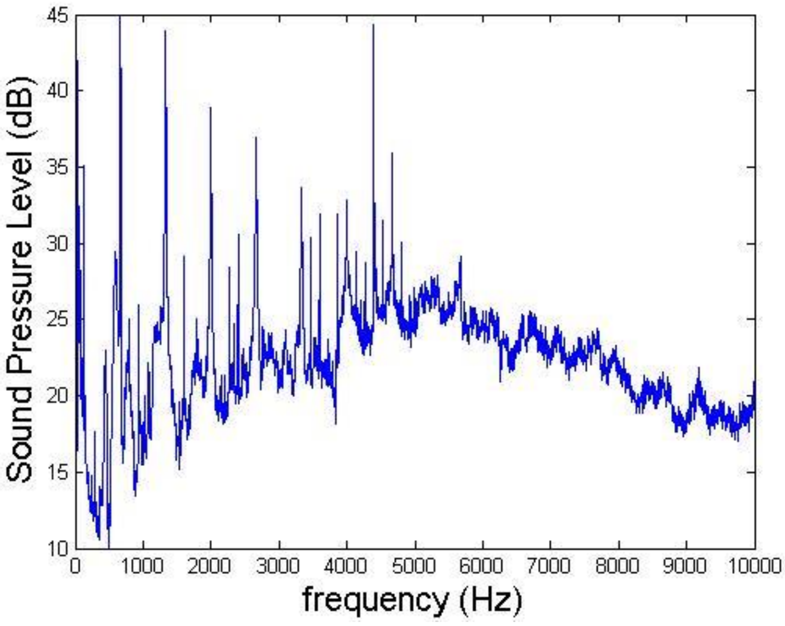

Figure 6.4. Far-field pressure from ducted rotor running at 4000 rpm.

Wall pressure data were obtained simultaneously at 32 circumferentially spaced locations for 51 different rotor speeds for the experimental setup detailed in Section 3.2. The data were initially processed by computing the spatial (circumferential) discrete Fourier transform of the instantaneous wall pressure. The auto-spectral density of the modal amplitudes, $\Phi_{pp,m}(f)$, were then computed, effectively giving the amplitude of pressure as a function of rotor speed, circumferential mode number, and frequency. Finally, these results were non-dimensionalized as

$$G^*_{pp,m}(f) = \frac{[\Phi_{pp,m}(f)]}{(U_{tip}/D)\left(\frac{1}{2}\rho_0 U_{tip}^2\right)^2} \quad , \qquad (6.20)$$

where ρ_0 is the density of the fluid medium, U_{tip} is the tangential velocity at the rotor tip, and D is the duct diameter.

Figure 6.5 shows $G^*_{pp,m}$ at a rotor speed of 4000 rpm as a function of circumferential mode number m and frequency. The results show a distinctive "V" shape that is a result of the acoustic cut-ons. Values along the V correspond to cut-on thresholds where the duct is resonating, values outside the V correspond to areas where the acoustics are not yet cut on, and values inside the V correspond to areas where the acoustics are cut on.

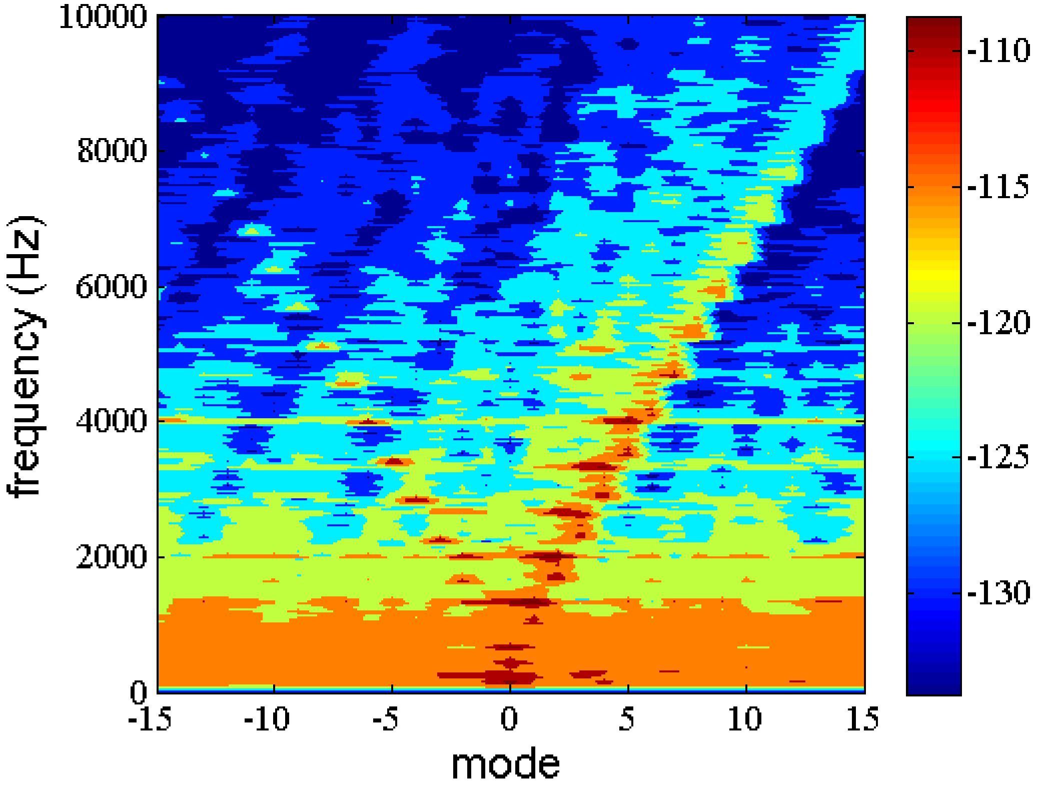

Figure 6.5. Auto-spectral density of wall pressure for a rotor speed of 4000 rpm as a function of frequency and circumferential mode number. Color axis equals $10\log_{10}(G^*_{pp,m})$.

There are notably high amplitudes of the unsteady surface pressure in Figure 6.5 at frequencies lower than the cut-on frequencies. These amplitudes are a result of the turbulent rotor wake and duct boundary layer. These pressure values are predominantly below 1000 Hz and appear to have little dependence on the mode number, *m*.

Analysis of the acoustic pressure requires removal of the hydrodynamic contribution to the pressure. Here we assume that the pressure is a summation of the acoustic and hydrodynamic contributions. The hydrodynamic pressure was found from the data presented in Figure 6.5 by assuming that the pressure for a given circumferential mode is entirely hydrodynamic for $f < f_{cut\text{-}on}$. The auto-spectral densities of the hydrodynamic pressure of several of the higher modes are shown in Figure 6.6. These results show little dependence on the circumferential mode, as noted above. Furthermore, the results were found to scale well with rotor speed using Equation (6.20). Due to these factors, the dimensionless hydrodynamic pressure spectra was estimated as a function of frequency by averaging the dimensionless spectra for all mode, frequency, and rotor combinations where acoustics were cut off. This hydrodynamic wall pressure spectra was subtracted from the measured wall pressure at a given rotor speed (when redimensionalized and scaled for the appropriate rotor speed) to obtain the acoustic wall pressure spectra. Note that all further references to wall pressure in this chapter will be referring solely to the acoustic wall pressure derived from this method.

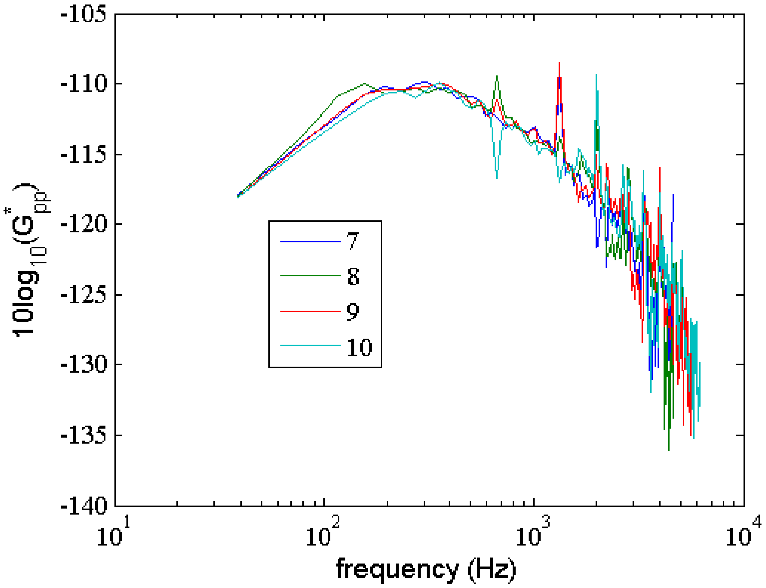

Figure 6.6. Hydrodynamic wall pressure for various circumferential modes.

6.3 F-T Separation

The acoustic wall pressure is the result of both the rotor's transfer function and forcing function. When analyzing the acoustic wall pressure induced by a single rotor speed, one cannot determine whether features of the response are due to the transfer function, the forcing function, or both. For this reason, when determining the accuracy of the acoustic wall pressure model, it is advantageous to individually examine the transfer function and forcing function rather than solely the acoustic wall pressure.

Through use of a force – transfer function separation (i.e. F-T separation) algorithm, experimental wall pressure data taken at various speeds can be used to determine the transfer function and the forcing function which generated the aforementioned wall pressures. It is beyond the scope of this thesis to provide a detailed explanation of the operation of an F-T separation algorithm. A brief summary will be supplied for the benefit of the reader. The algorithm used in this chapter is based on the algorithm used by Stephens and Morris [12].

The F-T separation algorithm operates under the assumption that, at each frequency, the pressure is equal to the product of the transfer function and forcing function. The transfer function is assumed to have no dependence on rotor speed, while the magnitude and frequency of features of the forcing function are assumed to scale with an unknown power of the rotor speed. As a result, as the rotor speed is increased, features of the pressure spectra which increase in frequency are attributed to the forcing function, while stationary features are attributed to the transfer function. The F-T separation algorithm provides a mathematical method by which pressure data at a series of rotor speeds are used to quantify this transfer function and forcing function. The transfer and forcing functions derived through this method were known as the experimental transfer function and experimental forcing function, respectively.

The F-T separation algorithm is only capable of identifying features in the transfer and forcing function, but it is not capable of independently determining the broadband magnitude of either function. To account for this, the experimental transfer function was given a broadband magnitude equal to that predicted by Equation (6.19). This allows the broadband magnitude of the experimental forcing function to be determined but has no effect on the features of the spectra for either function.

6.4 Experimentally Derived Forcing Function

The experimental forcing functions for modes -3 through 3 are plotted versus frequency normalized by blade passing frequency in Figure 6.7. Figure 6.7 also shows the theoretically-derived forcing function predicted through the approach noise model derived by Stephens and Morris [12,50]. Figure 6.7 is plotted as a function of the normalized forcing function, defined as

$$\mathcal{F}^* = \frac{[\Phi_{ff}(f)]_{rotor}}{8{\rho_0}^2{U_{tip}}^3{r_{tip}}^5} \qquad , \tag{6.21}$$

where $[\Phi_{ff}(f)]_{rotor}$ is the auto-spectral density of the force and r_{tip} is the radius of the rotor. Because of the normalization, each curve in Figure 6.7 is an aggregation of the data of multiple rotor speeds.

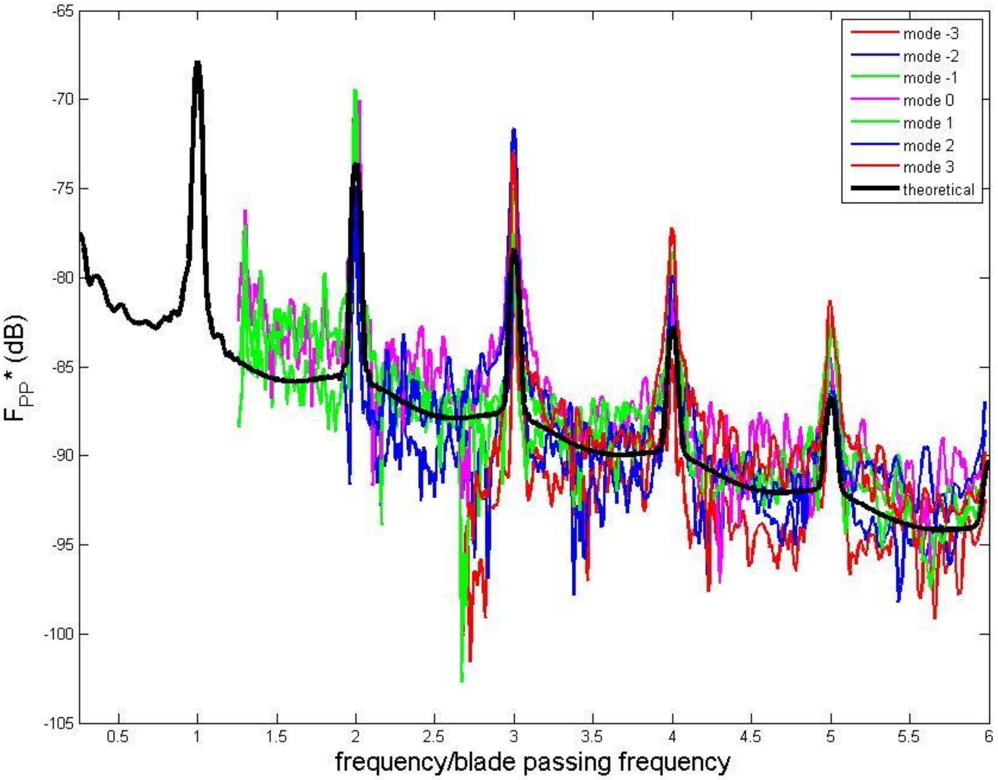

Figure 6.7. Normalized forcing predicted by experimental data as a function of frequency.

The approach noise model derived by Stephens and Morris [12,50] assumes that the acoustics generated by a ducted rotor can be approximated by a single, axially-aligned dipole located at the center of the rotor. For an observer in the far-field, the *m*=0 dipole ring will appear as a single dipole due to the entire ring being in phase for this mode. Thus, one would expect the approach noise model and the dipole ring model for m=0 to have a similar normalized forcing function, and Figure 6.7 shows relatively good agreement between these models.

For a cut off mode, the acoustic pressure has a constant value of zero with no spectral features, so the F-T separation algorithm cannot be applied to this region. This results in Figure 6.7 having little information for higher modes at lower frequencies. The force spectral density appears to be relatively independent of mode. The force spectral density is significantly larger at multiples of the blade passing frequency, which is consistent with the findings of several authors outlined in Chapter 2.

6.5 Experimentally Derived Transfer Function

The experimental transfer function derived from the F-T separation is shown in Figure 6.8, which shows the same overall V shape as the pressure spectra. In order to better see the details of the transfer function better, Figures 6.9 and 6.10 show the experimental transfer functions for circumferential modes 1 and 2, respectively, as a function of frequency. These are plotted alongside the theoretical transfer function for an infinite duct and the predicted transfer function for a finite duct with 3 tiers of image rotors. The overall trend of the experimental transfer function matches the overall trend in the infinite duct transfer function, including the fluctuations that were predicted by the interference of multiple radial modes interacting.

The experimental transfer function also qualitatively matches the finite duct transfer functions, showing the same types of interference patterns predicted from the interactions of the image rotors. While the scales over which these fluctuations occur are fairly similar in the experimental and theoretical cases, the exact locations and magnitudes of the small-frequency-scale peaks do not match. This is attributed to uncertainties in the exact parameters of the duct, as small changes in any dimension can cause fairly significant shifts in the exact locations of these peaks; this can include uncertainties in the reflection coefficient of the duct as well as the effective length of the duct for acoustic reflections. Furthermore, the changes in axial location which can cause large changes to the transfer function are small enough that it is possible that it challenges the assumption of being able to approximate the rotor as being formed of dipoles which are compact in the axial direction.

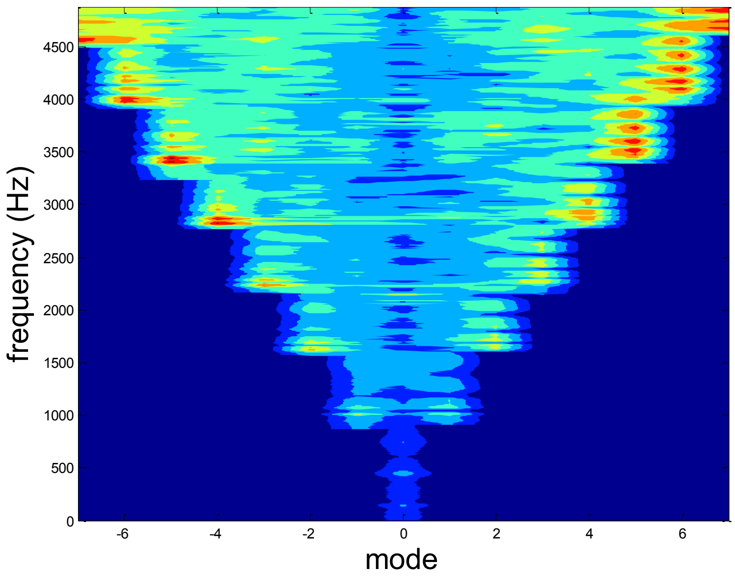

Figure 6.8. Experimental transfer function results within the duct as a function of mode (below cut-on, values are set to a low value as the values are undefined). Color values indicate 20 $\log_{10}$ of the transfer function in Pa/N.

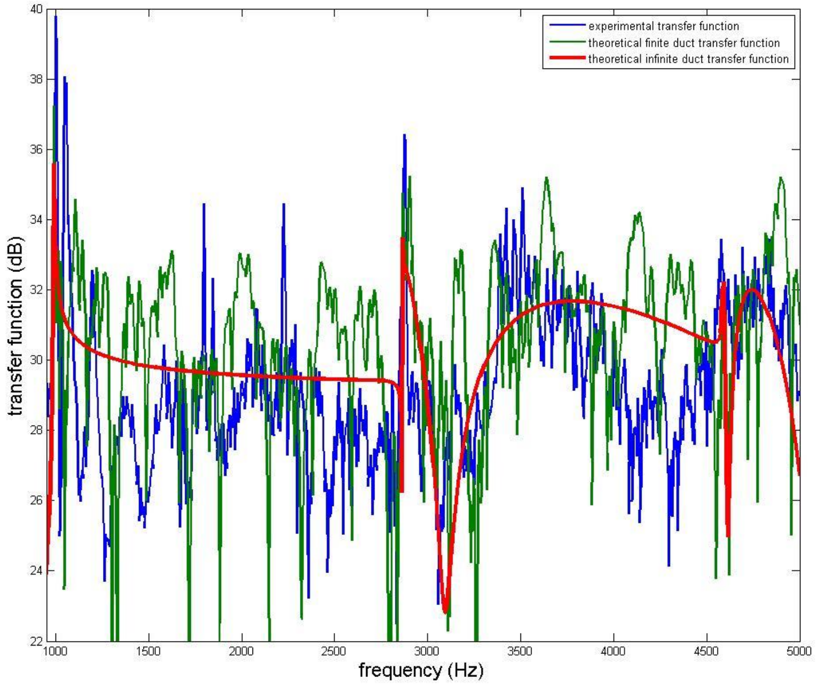

Figure 6.9. Experimental transfer function and predicted transfer functions for circumferential mode 1.

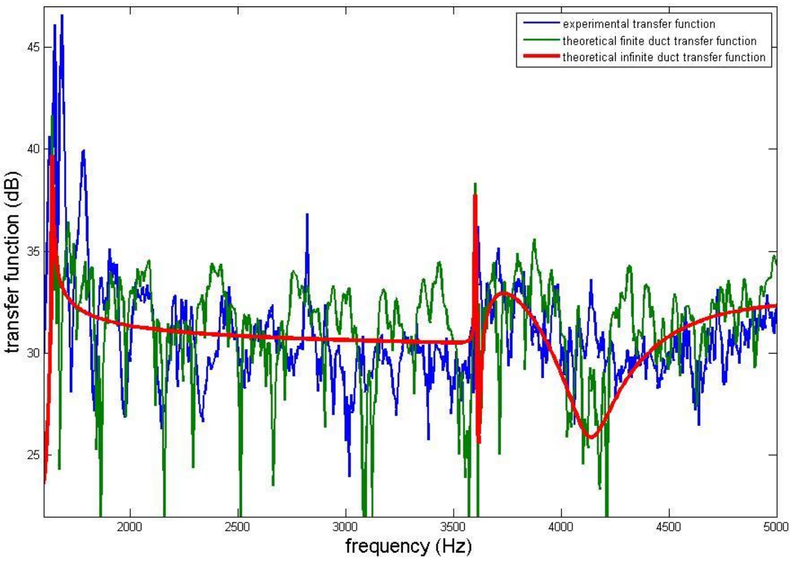

Figure 6.10. Experimental transfer function and predicted transfer functions for circumferential mode 2.

Further justification that the small-frequency fluctuations are generated by interference patterns as previously outlined can be obtained by viewing the experimental transfer function in the α_{mn} domain. For a frequency range over which a given circumferential mode has only one active radial mode, the phase of each rotor (both real and image) has a phase of $\alpha_{m1}(x-x_0)$, where x_0 varies with each rotor but α_{m1} does not. Thus, the overall signal should appear as a harmonic signal (with the amplitude possibly changing with α_{m1}) when plotted in the α_{m1} domain. Figure 6.11 shows circumferential mode 1 plotted in the α_{11} domain from 995 Hz to 2000 Hz, a range which only contains a single radial mode. This plot shows a strongly harmonic pattern, further validating the theoretical model. Note that this method only works for a single radial cut-on; with two radial cut-ons, a portion of the signal will scale with α_{m1} and a portion of the signal will scale with α_{m2}, making it irrelevant to plot the transfer function versus α_{m1} or α_{m2}.

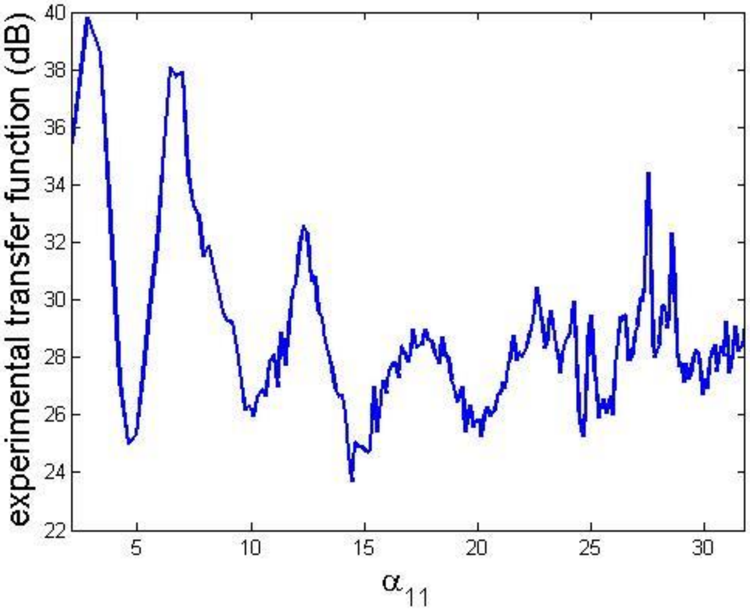

Figure 6.11. Experimental transfer function for circumferential mode 1 with for a single radial cut-on in the α_{11} domain.

CHAPTER 7

STRUCTURAL VIBRATION OF A FLUID-LOADED DUCT EXCITED BY AN INTERNAL ROTOR

This chapter involves measurement of the vibration of the fluid-loaded duct outlined in Chapter 3 when excited by an internal flow induced by the rotor. Knowledge of the vibration of the duct wall is important to the prediction of the acoustics radiated from the duct. The duct is lightly fluid loaded with a fluid loading factor of approximately one, placing it between the fluid loading factors of the two cases rectangular structural vibration cases examined in Chapters 4 and 5.

The work of this chapter is a final case combining the work of the previous chapters. Chapter 4 developed the MPI, which will be necessary for the duct vibration measurements of this chapter. Chapter 5 examined the effects of fluid loading, which will assist in explaining aspects of the results demonstrated in this chapter. The internal pressure field which excites the duct was examined in Chapter 6.

Duct vibration follows similar basic principles to that of a flat, bounded structure, but the cyclical boundary condition results in a much more complicated transfer function. A full examination of the vibration of a fluid loaded duct would be too much subject matter for the scope of this document. However, this chapter will examine duct vibration in the context of the fluid loaded vibration examined in Chapter 5. This is an exploratory measure towards identifying important aspects of fluid loaded duct vibration.

7.1. Vibration of a Single Point

For the duct setup detailed in Section 3.2, the reference laser was stationed at an arbitrary point located slightly off-center from the center of the duct in the axial direction. Due to the lack of bounds in the circumferential direction, there are no fixed nodal points in the circumferential direction; combined with the duct being axisymmetric, points are arbitrary in the circumferential direction. Figure 7.1 shows the auto-spectral density of vibration of the reference location, while Figure 7.2 shows the auto-spectral density of the reference location over a smaller range of frequencies. The lowest natural frequency occurs at 267 Hz. Above this frequency, local maxima in the auto-spectral density of vibration occur over increasingly small differences in frequency due to the high modal density of the structure.

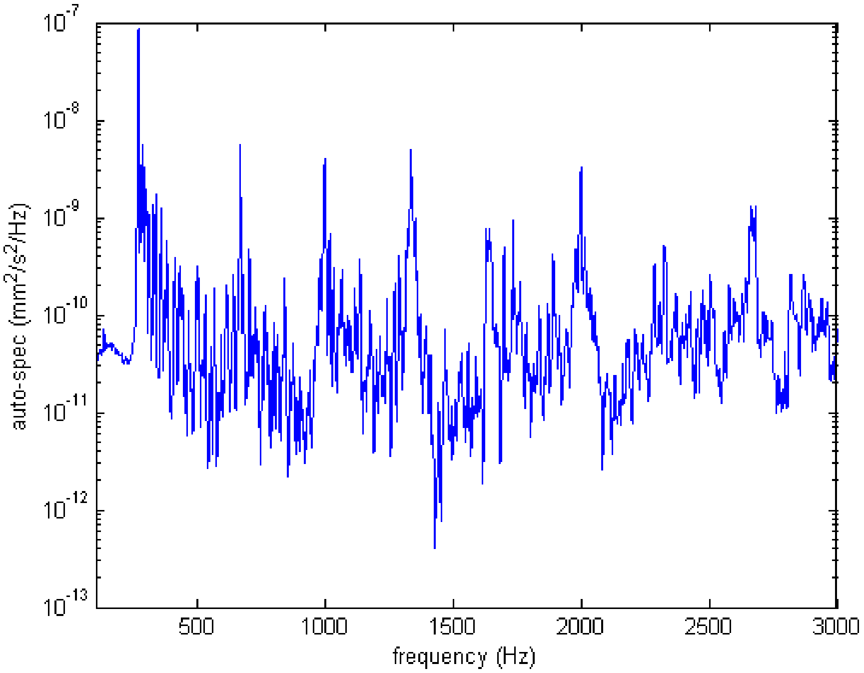

Figure 7.1. Auto-spectral density of vibration for the reference location at 4000 rpm.

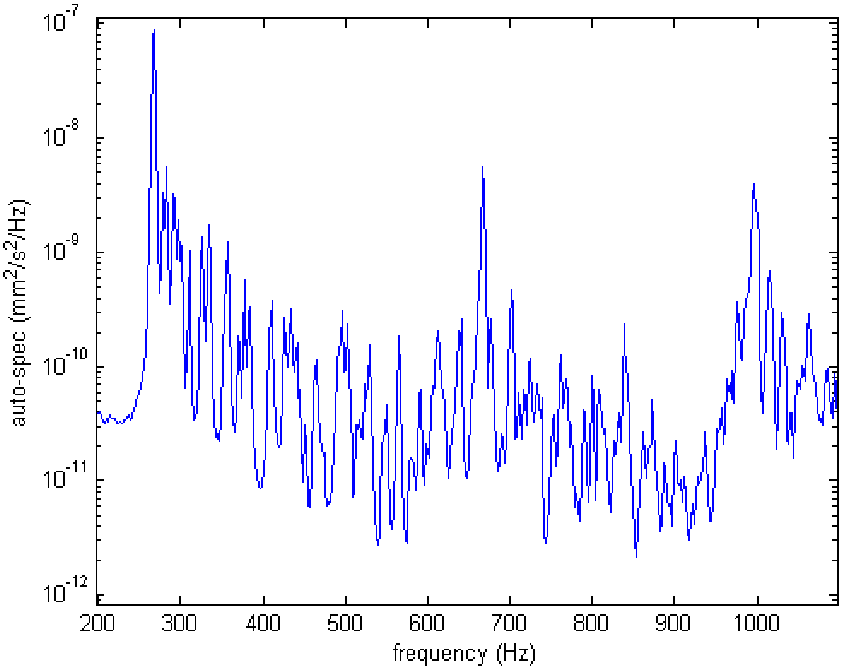

Figure 7.2. Auto-spectral density of vibration for the reference location at 4000 rpm (zoomed).

The reference location was scanned for approximately 16 seconds at rotor speeds from 0 rpm to 5000 rpm at 10 rpm increments. The auto-spectral density as a function of frequency and rotor speed from these scans is shown in Figure 7.3. Figure 7.4 shows the vibration of the reference laser over a more limited subset of speeds and frequencies.

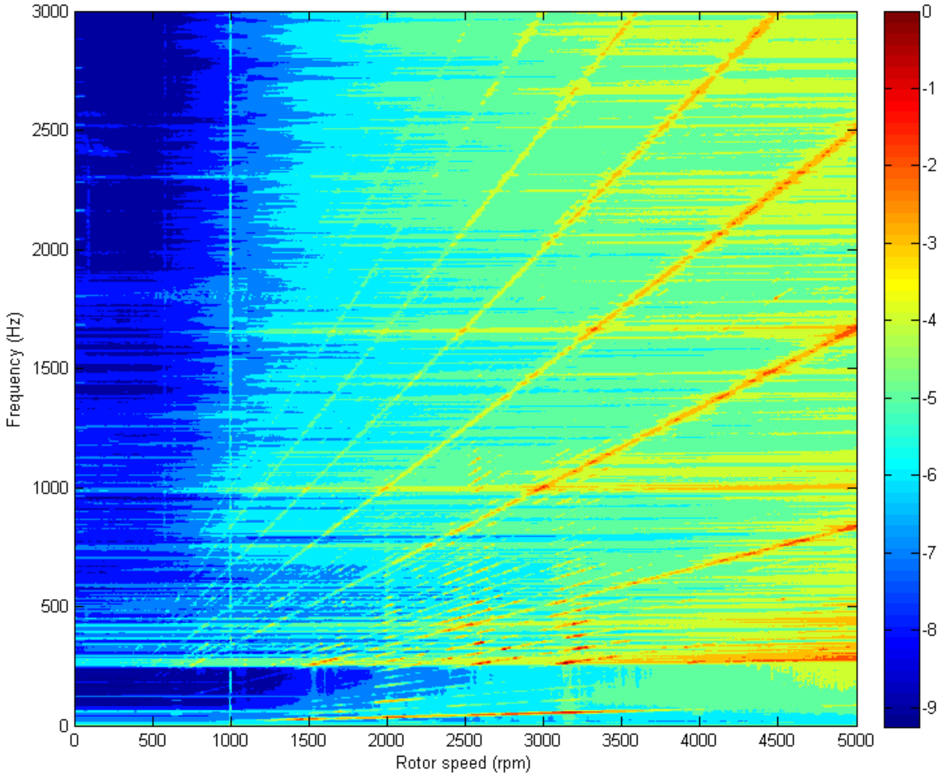

Figure 7.3. Auto-spectral density of duct vibration as a function of frequency and rotor speed. Color axis refers to $\log_{10}$ of the auto-spectral density of vibration divided by 1 $mm^2/s^2/Hz$.

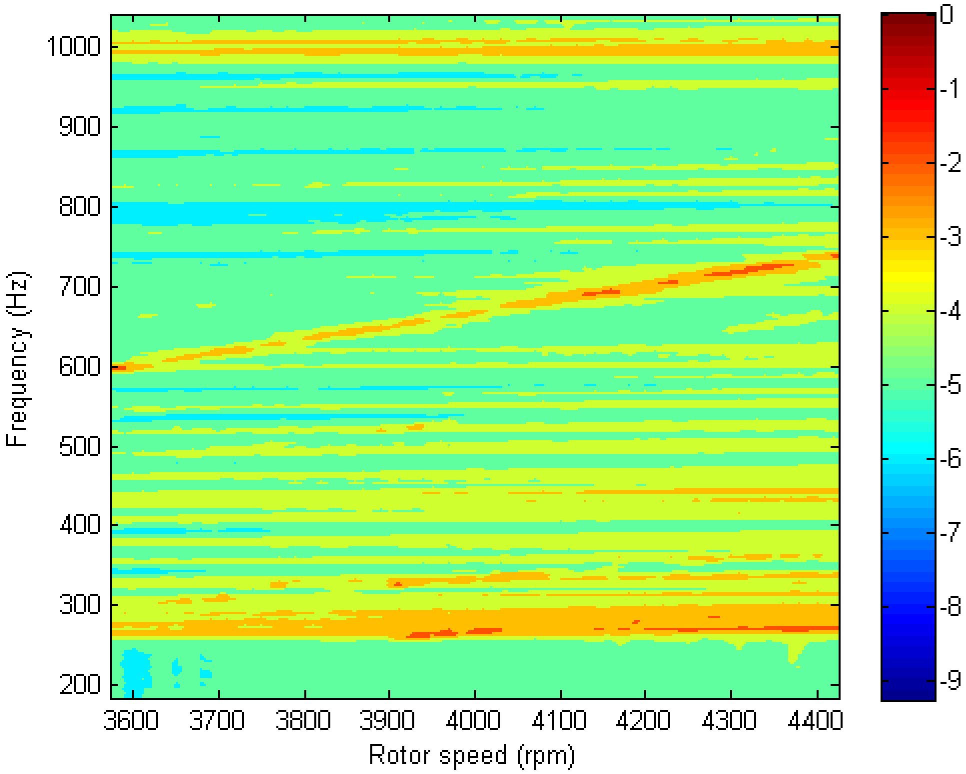

Figure 7.4. Auto-spectral density of duct vibration as a function of frequency and rotor speed over a limited set of rotor speeds and frequencies. Color axis refers to $\log_{10}$ of the auto-spectral density divided by 1 $mm^2/s^2/Hz$.

Several characteristics can be identified in Figure 7.3. The first duct natural frequency occurs at 267 Hz, as can be seen by the high-intensity region across all rotor speeds (i.e. horizontal line) at this frequency. For this frequency, all acoustic modes are cut off, as discussed in Chapter 6, since the lowest acoustic cut-on is at approximately 1000 Hz. Thus, the earliest duct modes are excited almost entirely by hydrodynamic effects.

At the lowest frequencies, the modal density is low enough that individual frequencies may not have a resonating mode. At these frequencies, local peaks in the vibration may be due to a modal resonance at that frequency. The modal density increases quickly for increasing frequency, such that above the first few natural frequencies every frequency will have multiple resonating modes.

High-intensity regions for all rotor speeds (i.e. horizontal lines) can be identified at approximately 1000 Hz and 1600 Hz. As was noted in Chapter 6, these frequencies correspond to the first two circumferential acoustic modes cutting on. These frequencies are substantially greater than the first natural frequency of the duct but result in noticeable peaks in the duct vibration. This indicates that that the acoustic cut-ons induce a large enough forcing field to result in significant duct vibration even though the acoustics are inactive until a much higher frequency than the first natural frequency of the duct.

The high intensity regions which have a frequency that scales with rotor speed (i.e. the diagonal lines in Figure 7.3) correspond to the blade rate of the rotor. For example, at 5000 rpm, such blade passing rates occur at 833 Hz, 1667 Hz, etc., corresponding to the first, second, etc. blade passing frequency of the rotor at that speed. Intersection of these blade passing frequencies with acoustic cut-ons provides for exceptionally large structural vibration.

7.2 Spatial Characteristics of Vibration

Vibration scans along a circumferential and axial line were taken at a rotor speed of 4000 rpm. Each point was scanned for 131 seconds at a sampling rate of 32 kHz.

Utilizing a mirror, a greater arc of the duct was acquired during the circumferential scan than the laser had direct line of sight with.

Figures 7.5 and 7.6 show the MPI for the circumferential and axial scans at 267 Hz, the first natural frequency and highest-amplitude mode of the structure. Figures 7.7 and 7.8 show the coherence of the circumferential and axial scans at this same frequency. In the circumferential plots, the reference laser is located at 0 degrees.

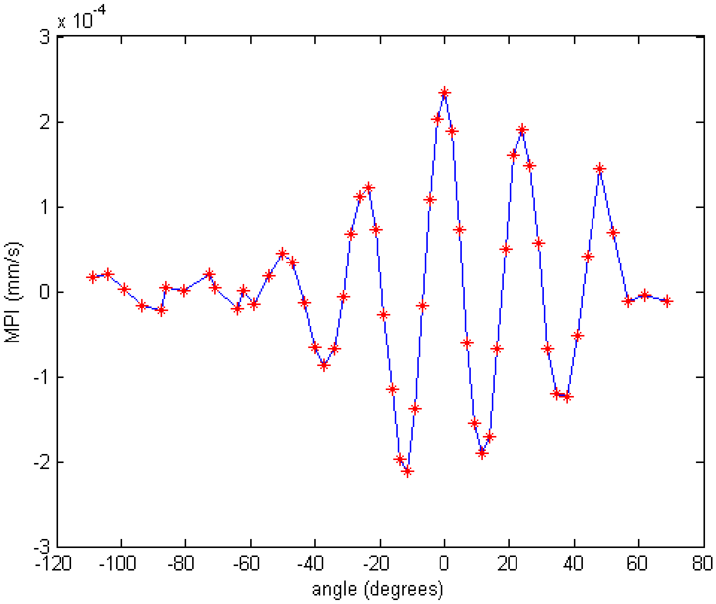

Figure 7.5. Circumferential duct MPI at 267 Hz for a rotor speed of 4000 rpm.

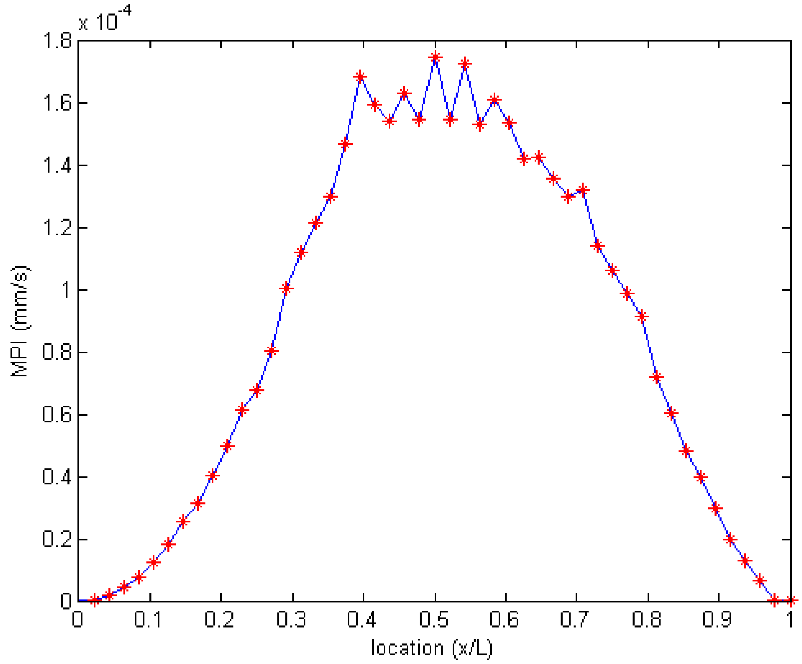

Figure 7.6. Axial duct MPI at 267 Hz for a rotor speed of 4000 rpm.

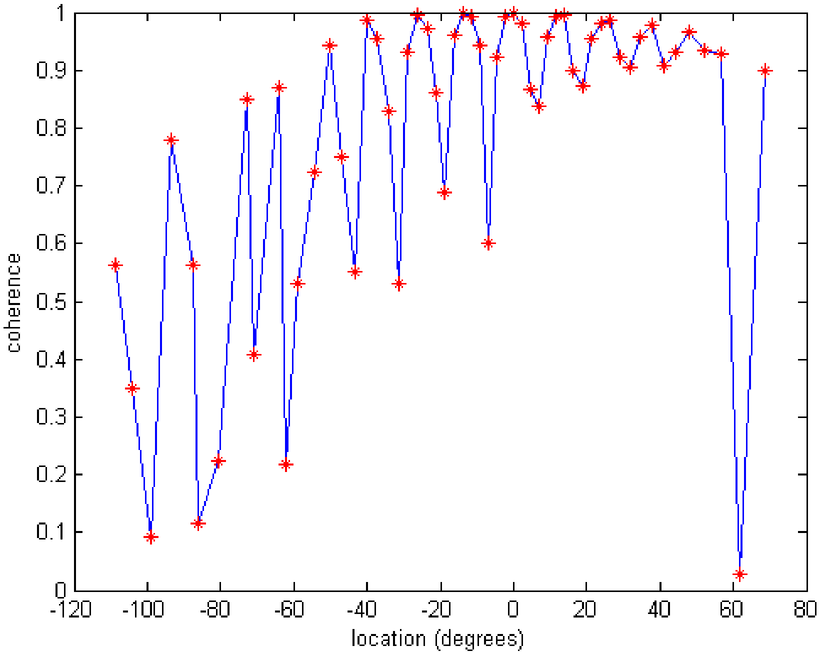

Figure 7.7. Circumferential duct coherence at 267 Hz for a rotor speed of 4000 rpm.

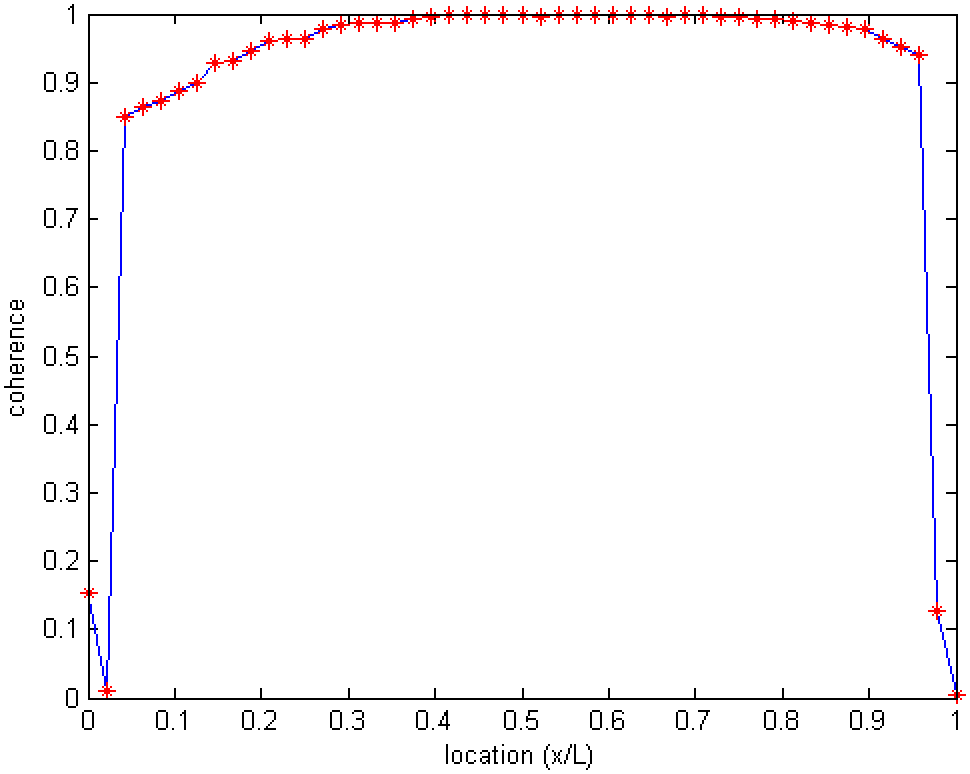

Figure 7.8. Axial duct coherence at 267 Hz for a rotor speed of 4000 rpm.

Somewhat similar results are seen for the fluid-loaded duct cases shown above as were seen for the case of the fluid-loaded rectangular foil. Both plots show fluctuating values over a relatively consistent length scale, which is indicative of a sine wave mode shape, as would be predicted for the circumferential direction of a duct. Both the circumferential MPI and coherence show decay in magnitude for increasing spatial separation from the reference location, which can be explained by the results demonstrated in Chapter 5. In particular, the high damping associated with the fluid loading of the duct causes the mode shapes to be localized within the structure. This is distinct from what would be predicted for the vibration of a non-fluid-loaded duct in the circumferential direction, where theoretically the mode shape should have a constant magnitude for all peaks in the structure, appearing as a sine wave.

It should be noted that there is one substantial difference between the MPI of the duct and the fluid-loaded foil. In the case of the foil, due to the structure being bounded, nodes occur at fixed locations in the structure. These nodal locations may change based on the forcing field, but for statistically stationary forcing, the nodes will remain at fixed locations. For the case of the duct, there are no bounds in the circumferential direction, so nodal locations do not remain fixed; rather, they have a tendency to spin around the structure. As such, nodal locations can only be defined either at a fixed instance in time or relative to other points in the structure. In the case of MPI and coherence, the nodal locations are defined relative to the location of the reference signal, with a point being defined as a node at a given frequency if the reference location is at a maximum while the node location has a value of zero; by contrast, the nodes of a bounded plate will have zero vibration at a given frequency regardless of the reference location chosen.

This effect may explain the "smearing" seen in the circumferential coherence plot. In the coherence plots for the bounded structures in Chapters 4 and 5, the coherence tends to be relatively constant as a function of spatial location (though this constant value was not necessarily unity in the fluid-loaded cases), dropping quickly towards a value of zero only close to the node locations. In the duct case, for increasing circumferential separation, the coherence hits a local maximum over very small amounts of circumferential difference and seems to be constantly changing as a function of spatial separation (i.e. the coherence does not plateau to a constant value off of the nodal locations). However, the coherence at the nodal locations in general does not go to zero.

Both of these factors are distinct from coherence seen in the cases of the bounded, rectangular plates and foils. This can potentially be explained by the node locations not being fixed in space. Essentially, the node locations "spin" around the structure, with even the reference location functioning as a node at times. Points that are not vibrating at an instant in time will be incoherent with all other points in that instant in time. Excluding the spatial decay in coherence induced by fluid loading, two points will be coherent when neither is near a node and incoherent when one is exactly on a node at one instant in time. The overall coherence between the two points would then be a function of the percentage of time when one is located near a node and another is not. Because the modes spin in the structure, this would never go truly to zero, but would cause the roughly step-function like coherence field observed in a bounded structure to "smear" into the coherence profile seen in Figure 7.7.

The axial MPI of the duct shows a relatively similar mode shape to the one-dimensional eigenfunction predicted by Leissa for mode 1, as shown in Figure 4.1. There is a small spatial coherence decay along the axial scan, as shown in Figure 7.8. It is unclear if this is due to the coherence decay associated with fluid-loading or if this decay in coherence is poor signal-to-noise due to the relatively low vibration near the end points, as can be observed in Figure 7.6.

A single frequency was chosen for this analysis, but the results were found to be similar for all frequencies, with the exception of a different mode number at different frequencies. The coherence and MPI at several other frequencies are shown in Figures 7.9-7.12. These frequencies correspond to frequencies where the auto-spectral density of vibration had a localized peak, but due to the high modal density of the duct, these the vibration at these frequencies may be the result of multiple resonating modes.

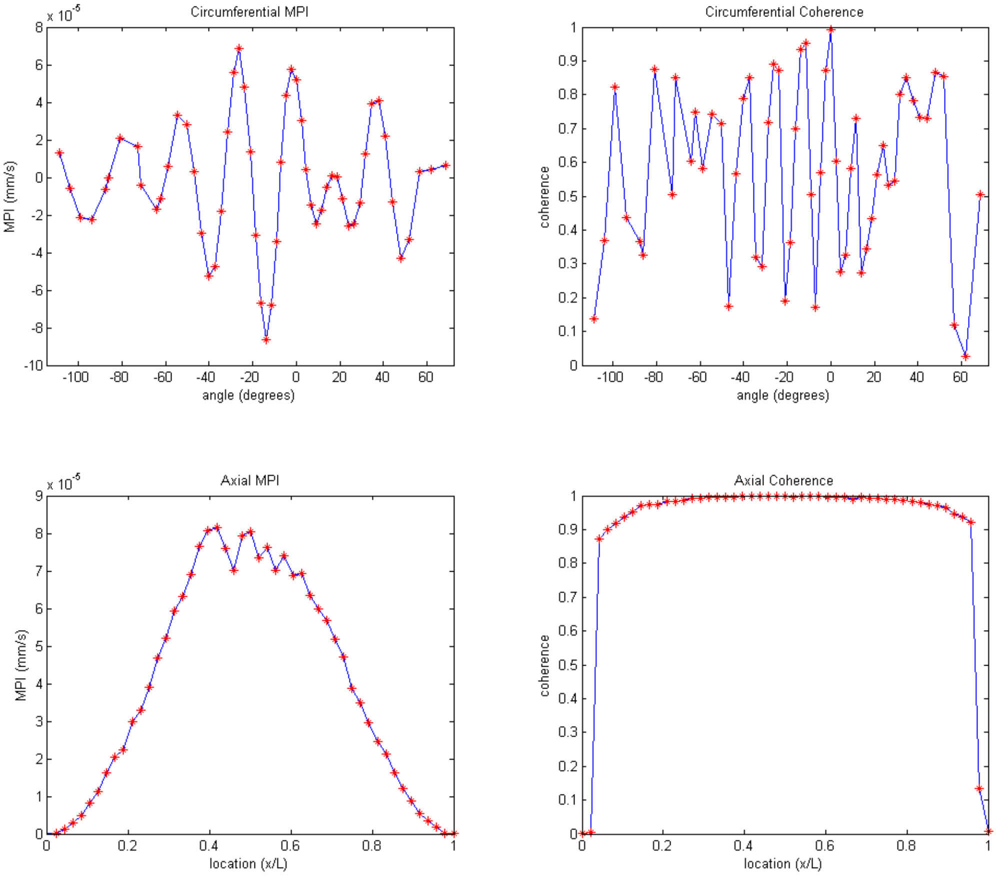

Figure 7.9. Duct MPI and coherence for 277 Hz.

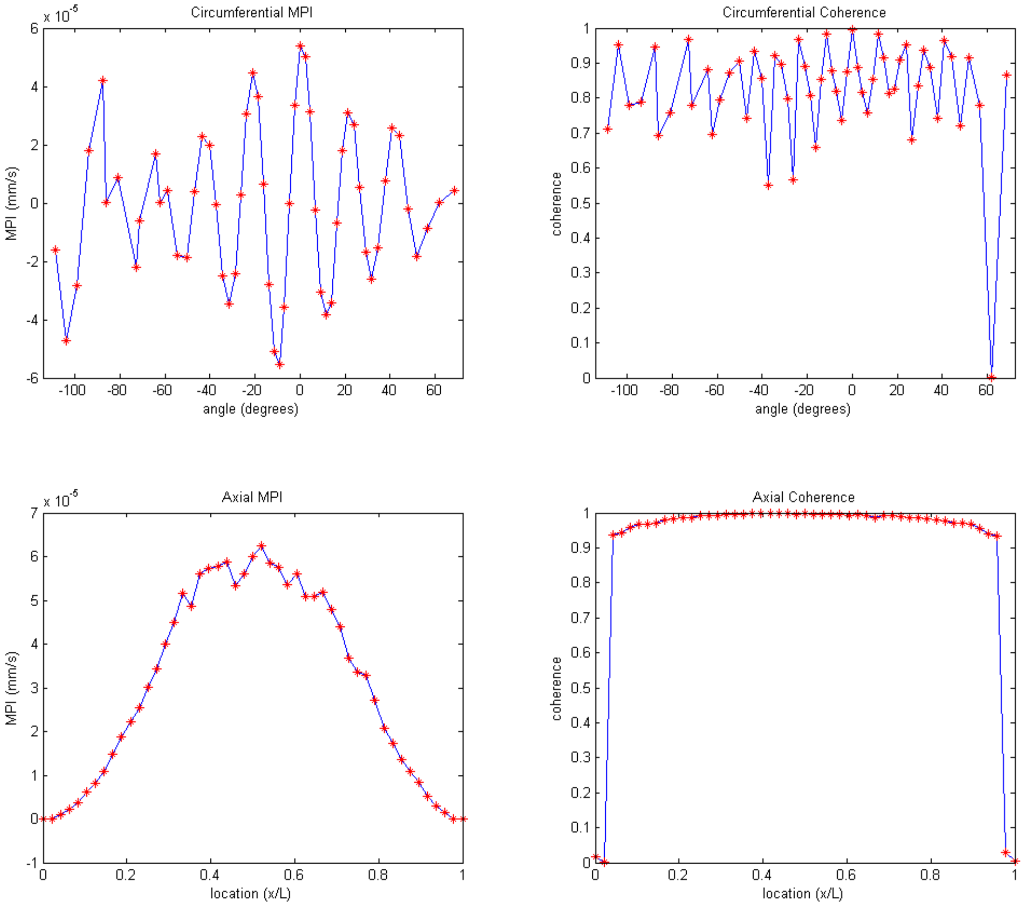

Figure 7.10. Duct MPI and coherence for 291 Hz.

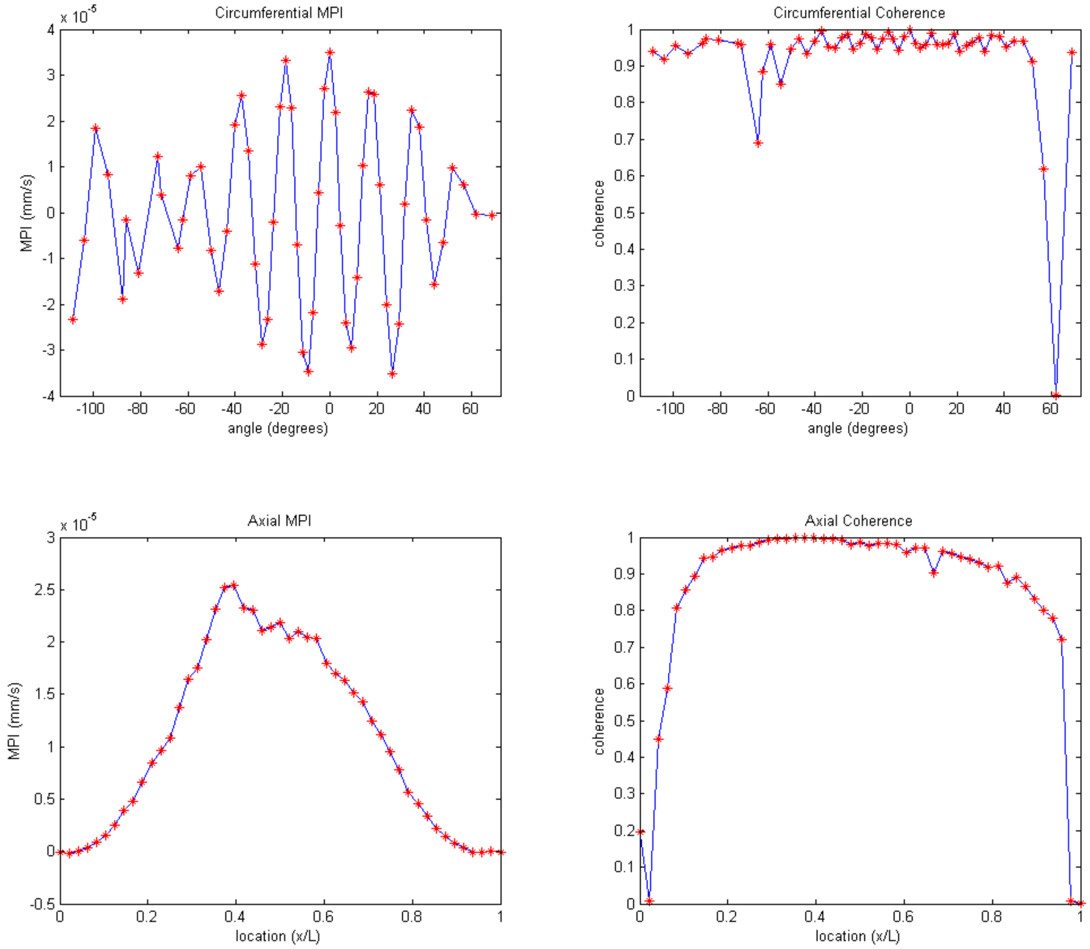

Figure 7.11. Duct MPI and coherence for 357 Hz.

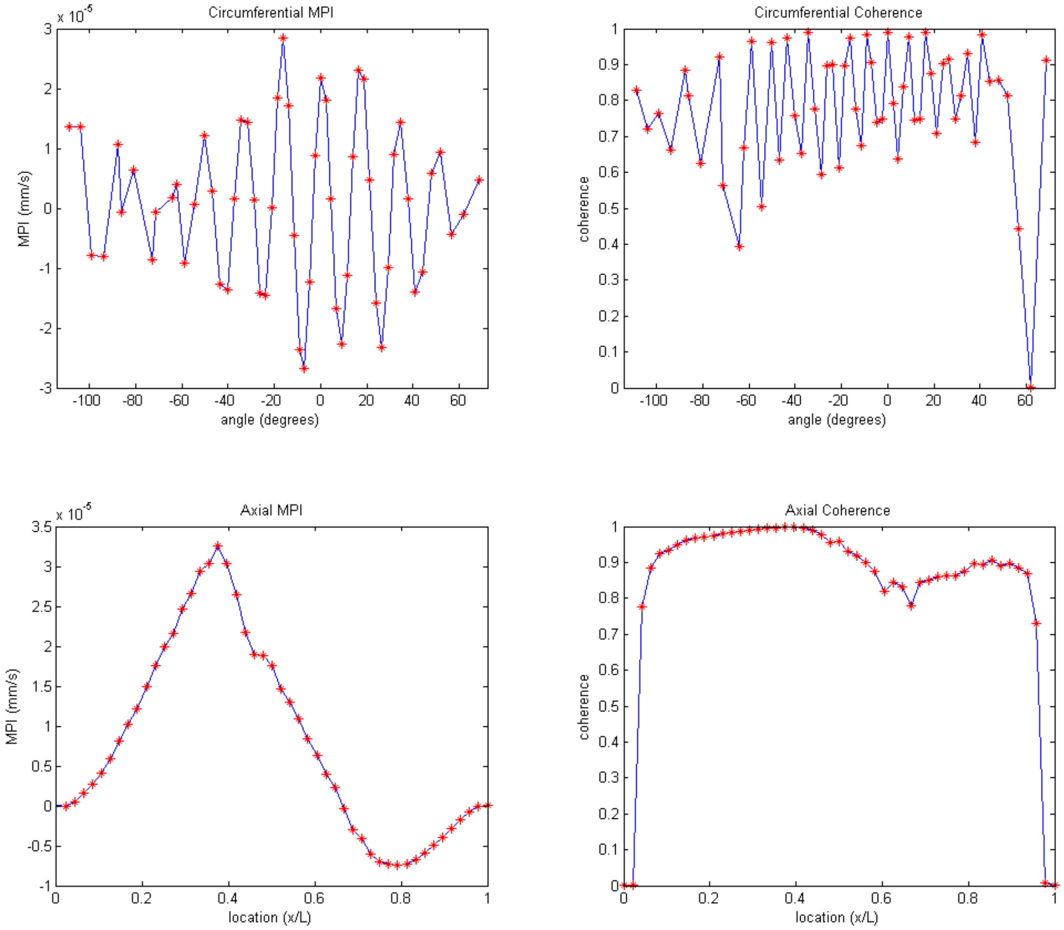

Figure 7.12. Duct MPI and coherence for 410 Hz.

7.3 Dispersion Curve

In general, each mode of vibration for a structure has a unique natural frequency. For rectangular structures, mode <*m*,*n*> has lower natural frequencies for decreasing *m* and *n*. For a duct, vibration for low circumferential mode number *m* is dominated by tension-induced stiffness, like a membrane, while vibration for high circumferential mode number *m* is dominated by bending stiffness, like a plate. Moderate mode numbers are a combination of these two effects. The natural frequency in the membrane regime decreases with increasing mode number, while the natural frequency in the bending stiffness regime increases with increasing mode number. As a result, unlike rectangular structures, the lowest natural frequency does not occur for a minimum of *m* for a duct, but rather, occurs for when the addition of these two effects are at a minimum.

The plot of the natural frequency as a function of circumferential mode number *m* and axial mode number *n* is known as the dispersion curve. Ivanyuta and Finkelshtein [51] used the Galerkin method to derive the natural frequencies for a duct as

$$\Omega^2 = \frac{(1-\nu^2){\lambda_n}^4}{{\lambda_n}^4+m^4+1.110m^2{\lambda_n}^2} + \frac{1}{12}\left(\frac{h}{R}\right)^2 {\lambda_n}^4 + m^4 + 1.110m^2{\lambda_n}^2 \quad , \tag{7.1}$$

where

$$\lambda_n = \frac{(2n+1)\pi R}{2L}; \qquad m=1,2,\ldots \tag{7.2}$$

and Ω is the non-dimensional frequency parameter defined as

$${\omega_n}^2 = \frac{\Omega^2 E}{\rho R^2(1-\nu^2)} \quad . \tag{7.3}$$

Here, ν is Poisson’s ratio, *m* is the circumferential mode number, *n* is the axial mode number, *h* is the duct thickness, and *L* is the axial length of the duct.

Figure 7.13 shows the theoretical dispersion curve for a duct with the characteristics outlined in Section 3.2 for the first three axial modes. Note the dispersion curve is only valid at integer mode number values; Figure 7.13 is drawn as solid lines only to make it more easily readable. In Figure 7.13, one can readily observe that the modal density (defined as the number of resonating modes per change in frequency) increases very quickly for increasing frequency. Even when only one axial mode is active, both the left side (tension-induced) and the right side (bending stiffness) sides of the curve contribute contain new resonating modes for small changes in frequency, leading to relatively high modal density. Once more axial modes becomes active, the modal density becomes substantially higher.

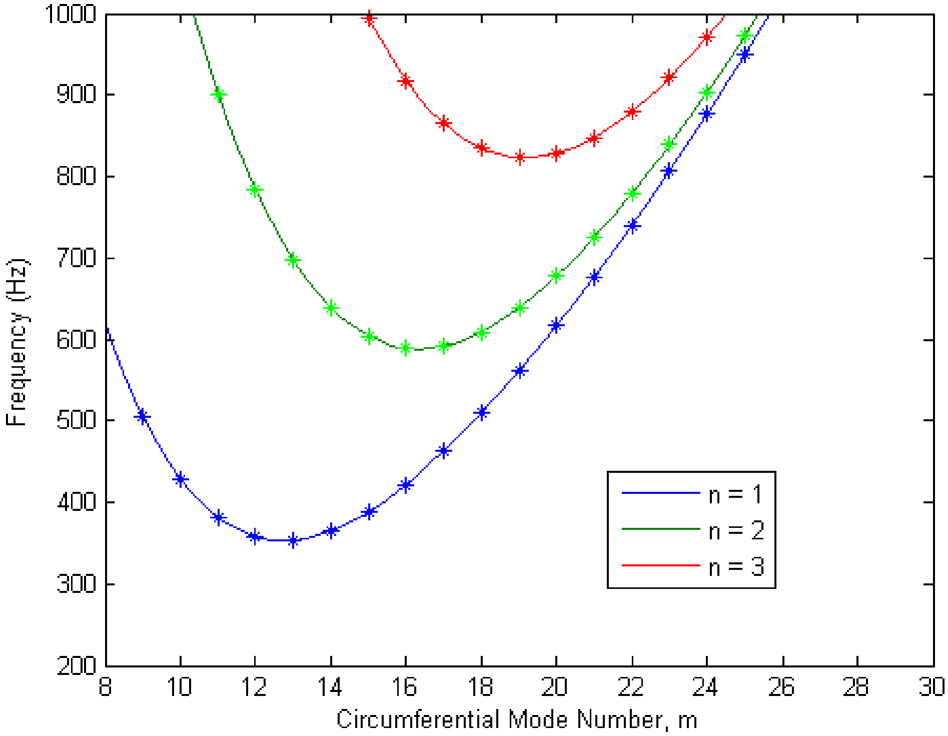

Figure 7.13. Theoretical dispersion curve for nickel duct. Legend refers to axial mode number.

Circumferential vibration data were taken at a rotor speed of 4000 rpm. At the lowest resonating frequencies, a circumferential surface shape was generated using MPI, as detailed in Chapter 4. The mode number of the vibration was identified from the surface shape, and plotted on a dispersion curve, as shown in Figure 7.14. Figure 7.14 contains three plots. The base dispersion curve corresponds to the theoretical dispersion curve for axial mode n=1, as shown in Figure 7.13. The measured values in Figure 7.14 are those determined experimentally through MPI. Lastly, the fluid-loaded dispersion curve corresponds to the dispersion curve for n=1 resulting from a changing the density and effective length of the duct in order to roughly fit the data.

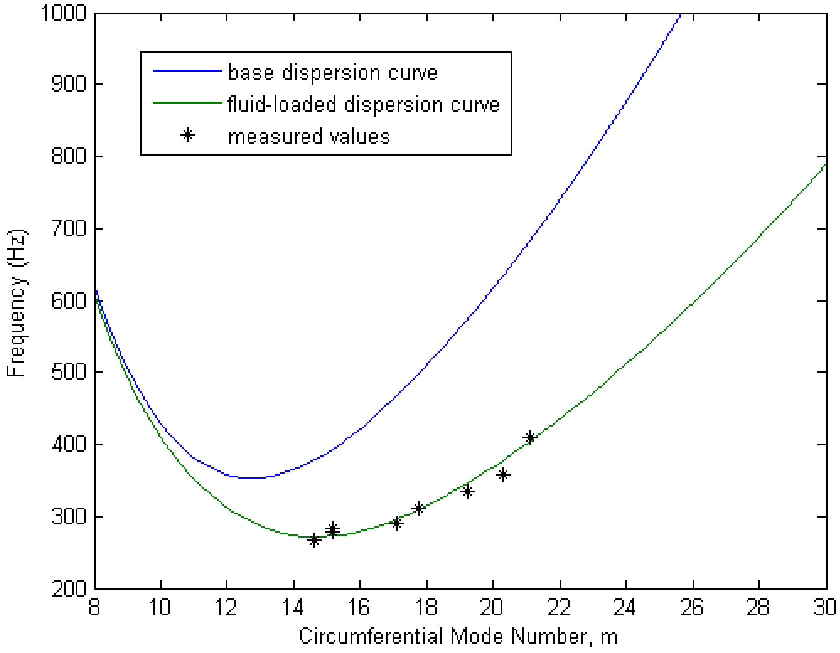

Figure 7.14. Dispersion curve for axial mode 1 of the duct. Contains the theoretical dispersion curve, the dispersion curve for modified duct properties, and the experimentally-determined dispersion curve through use of MPI.

The fluid-loaded dispersion curve in Figure 7.14, which causes the dispersion curve to match the data, was generated analytically by tripling the density of the duct and reducing the effective length of the duct by 25%. It is not immediately clear why these parameters change in this fashion, but the result does create a relatively strong fit between the data and the theoretical dispersion curve. Fluid-loading has an effect similar to increasing the mass of a structure, which could explain the increase in density, though a tripling of density is substantially higher than what would be predicted for a fluid loading factor of approximately 1.

7.4 Discretized Ring Model

To examine the underlying physics creating the vibration field of the nickel duct, a discretized ring model was created. A schematic of this ring model is shown in Figure 7.15. This model is the nickel duct analog to the string model examined in Section 5.5. The model consists of a ring discretized into a series of point masses. The ring is attached to rigid walls on either side. This is similar to a single circumferential slice of the duct, where the rigid wall is meant to be a simple simulation of the effects of a parallel circumferential circular slice. Without this, the ring has an insufficient number of boundary conditions, and any force will cause the entire ring to move through space. 200 discrete masses were used in the simulation.

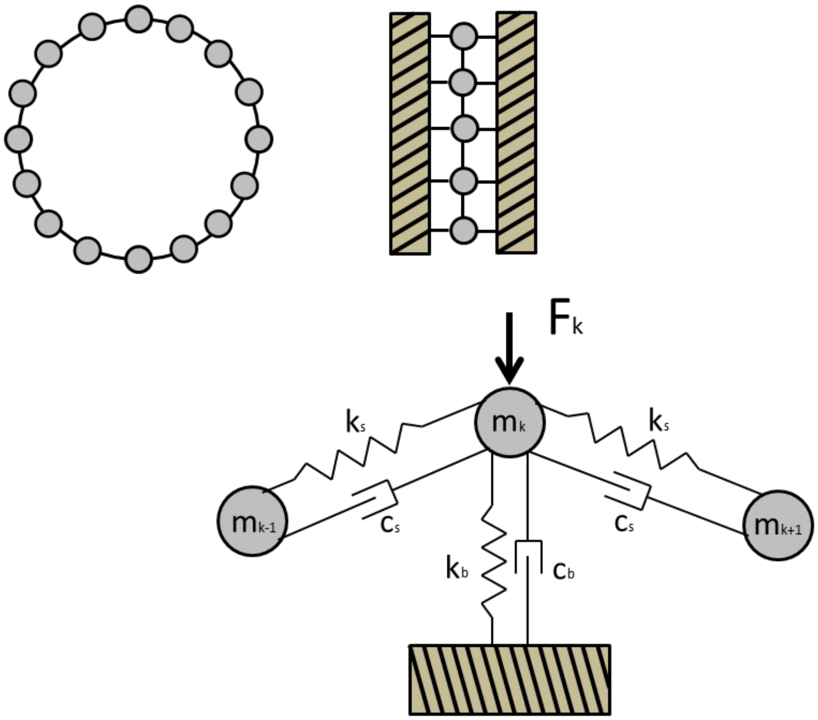

Figure 7.15. Schematic of discretized ring model.

High damping was applied to the ring model with random but statistically homogeneous forcing at all points. The simulation was allowed to run to a steady state. MPI and coherence (reference point: 106 degrees) of the first active mode taken from the steady state of the simulation is shown in Figures 7.16 and 7.17. This simulation was not designed to provide exact predictions of the vibration. Figures 7.16 and 7.17, determined under the effects of high damping, appear relatively similar to the MPI and coherence of the first mode, as displayed in Section 7.2.

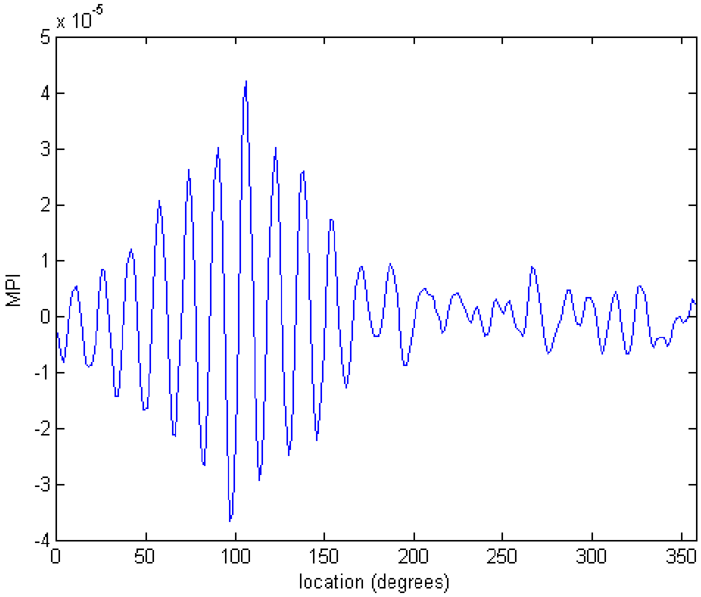

Figure 7.16. MPI of first mode of ring model.

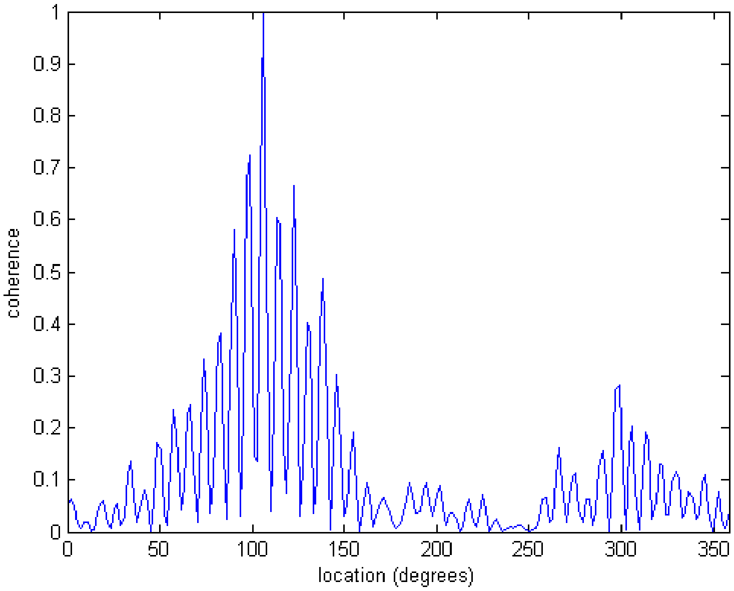

Figure 7.17. Coherence of first mode of ring model.

7.5 Conclusions

The results here are an exploratory examination into the vibration of a fluid-loaded duct due to an internal rotor. Due to the complexity of the system, it is beyond the scope of this document to undergo a more in depth analysis. It was found that the theoretical dispersion curve appears to match the measured dispersion curve of the lowest frequencies if the theoretical dispersion curve is given a higher density and lower effective length. The fluid-loading effects detailed in Chapter 5 can be observed in the circumferential MPI of the fluid-loaded duct, with a spatial decay in the coherence field and mode shape, which would not normally be predicted by modal analysis theory. A discretized ring model with high damping was found to have a similar MPI and coherence at its first mode compared to those measured experimentally, though this model was not meant to allow for exact predictions of the duct's vibration. These form only the beginnings of an examination of the vibration of a fluid-loaded duct but appear to explain the underlying physics associated with the problem.

CHAPTER 8

CONCLUSIONS

This document has covered multiple topics both experimentally and analytically related to flow-induced structural vibration.

Chapter 4 developed a method known as Magnitude-Phase Identification (MPI) to experimentally determine modal characteristics of a structure while only using two-point measurements. This chapter also detailed two methods of decomposing the vibration of a structure into its mode shapes: minimization of error and modal projection. Using two laser Doppler velocimeters (LDV), measurements were taken of a non-fluid-loaded, clamped, rectangular plate excited by a spatially homogeneous turbulent boundary layer flow. Through use of MPI, the auto-spectral density of vibration for each mode was found. For either decomposition method, the results were found to agree relatively well with the theoretical modal vibration spectra.

Chapter 5 examined the simultaneous effects of fluid-loading and spatially non-homogeneous forcing on a bounded rectangular structure. The same experimental setup as Chapter 4 was used, but in some cases the non-fluid-loaded plate was replaced with a heavily fluid loaded foil, and in some places a substantial spatial non-homogeneity was placed into the wall pressure field. Experimental results showed that individually, neither fluid-loading nor the spatial non-homogeneity in the wall pressure resulted in a significant change in the measured mode shapes of the structure. When both effects were combined, the mode shapes of the structure became significantly skewed towards the points of higher forcing, demonstrating that the mode shapes of a fluid-loaded structure can be dependent on the forcing field applied, a characteristic not accounted for in modal analysis theory. Furthermore, these mode shapes are potentially substantially asymmetric, which can lead to significantly increased acoustic radiation in the far-field. Using a string model, it was shown that these characteristic changes can occur for a highly damped system. Fluid-loading is known to have the effect of increasing the damping of a system.

Chapter 6 examined the internal acoustic wall pressure field due to a ducted rotor. The analysis assumes that the rotor's acoustics can be approximated by replacing the rotor with a continuous ring of dipoles located at the rotor blade tip, and then applying the theoretical transfer function for a dipole within a duct to the dipole ring. The resulting transfer function is known as the rotor transfer function, and is mathematically equal to the magnitude of the acoustics for a given circumferential mode number generated by a dipole ring of unitary magnitude for that same circumferential mode number. The finite length of the duct is accounted for by using a method of images at the duct inlet and exit. Both the interaction of multiple radial modes and the interaction of the image rotors each create significant frequency-dependent interference patterns, which experimentally might be discounted as noise but actually appears in the resulting theoretical function. Using forcing – transfer function separation, experimental wall pressure data was separated into forcing components and transfer function components.

The forcing components resulting from this analysis were found to agree well with previously predicted forcing functions. The measured transfer function was found to agree relatively well with the theoretical transfer function predicted through this analysis.

Chapter 7 examined the vibration of a fluid-loaded duct excited by the rotor outlined in Chapter 6. Two-point laser measurements were used to obtain circumferential vibration data of the duct, using the MPI technique developed in Chapter 4. The resulting dispersion curve was found to agree well at low frequencies with the theoretical dispersion curve for significantly increased wall density and a reduced effective axial duct length. Circumferential MPI had similar results to the case of the fluid-loaded rectangular foil, with a reduction in the magnitude of the MPI and coherence with increasing separation distance from the reference location. A discretized ring model with high damping was found to have a similar MPI and coherence at its first mode compared to those measured experimentally.

APPENDIX A

EXPERIMENTAL WAVE NUMBER TRANSFORMS FOR RECTANGULAR STRUCTURES

Figures A.1-A.3 show the wave number transforms for the first three measured mode shapes for four cases:

1) The non-fluid-loaded (thick), steel plate excited by spatially homogeneous forcing, as outlined in Chapter 4.
2) The fluid-loaded (thin), aluminum foil excited by spatially homogeneous forcing, as outlined in Section 5.3.
3) The fluid-loaded (thin), aluminum foil excited by the vertical splitter such that the wall pressure was non-homogeneous in the spanwise direction, as outlined in Section 5.4.
4) The fluid-loaded (thin), aluminum foil excited by the horizontal splitter such that the wall pressure was non-homogeneous in the streamwise direction, as outlined in Section 5.4.

In these figures, forcing methods which cause a skewing of the mode shape are highlighted in red.

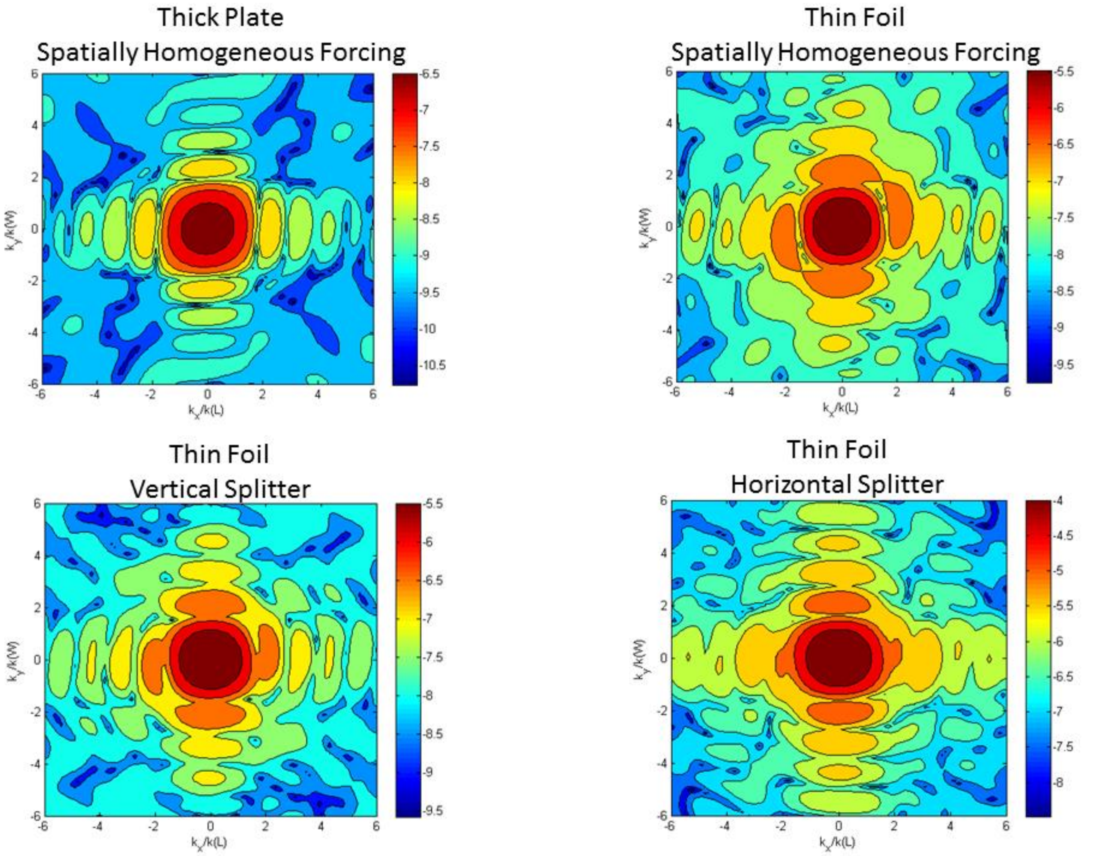

Thick Plate
Spatially Homogeneous Forcing

Thin Foil
Spatially Homogeneous Forcing

Thin Foil
Vertical Splitter

Thin Foil
Horizontal Splitter

Figure A.1. Wavenumber transform for mode <1,1> excited by various methods. Color axis corresponds to $\log_{10}$ of the surface shape at the natural frequency divided by (m/s).

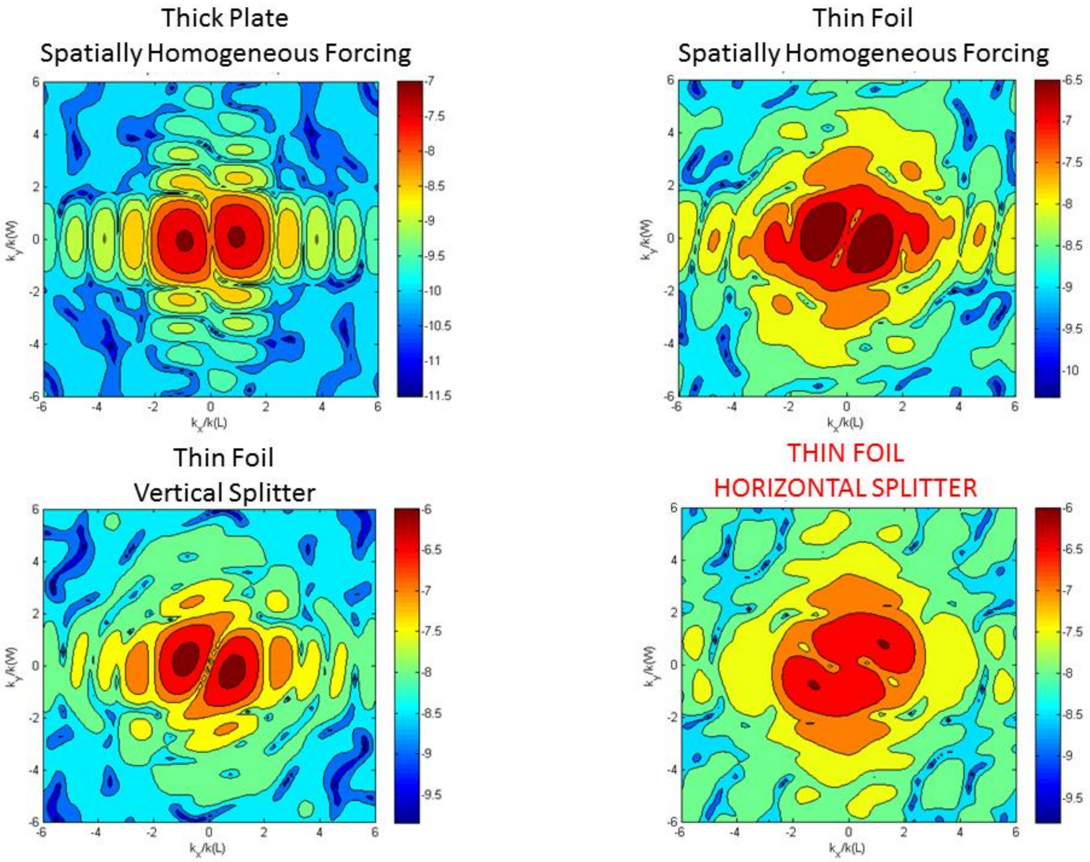
Thick Plate
Spatially Homogeneous Forcing

Thin Foil
Spatially Homogeneous Forcing

Thin Foil
Vertical Splitter

THIN FOIL
HORIZONTAL SPLITTER

Figure A.2. Wavenumber transform for mode <2,1> excited by various methods. Color axis corresponds to $\log_{10}$ of the surface shape at the natural frequency divided by (m/s).

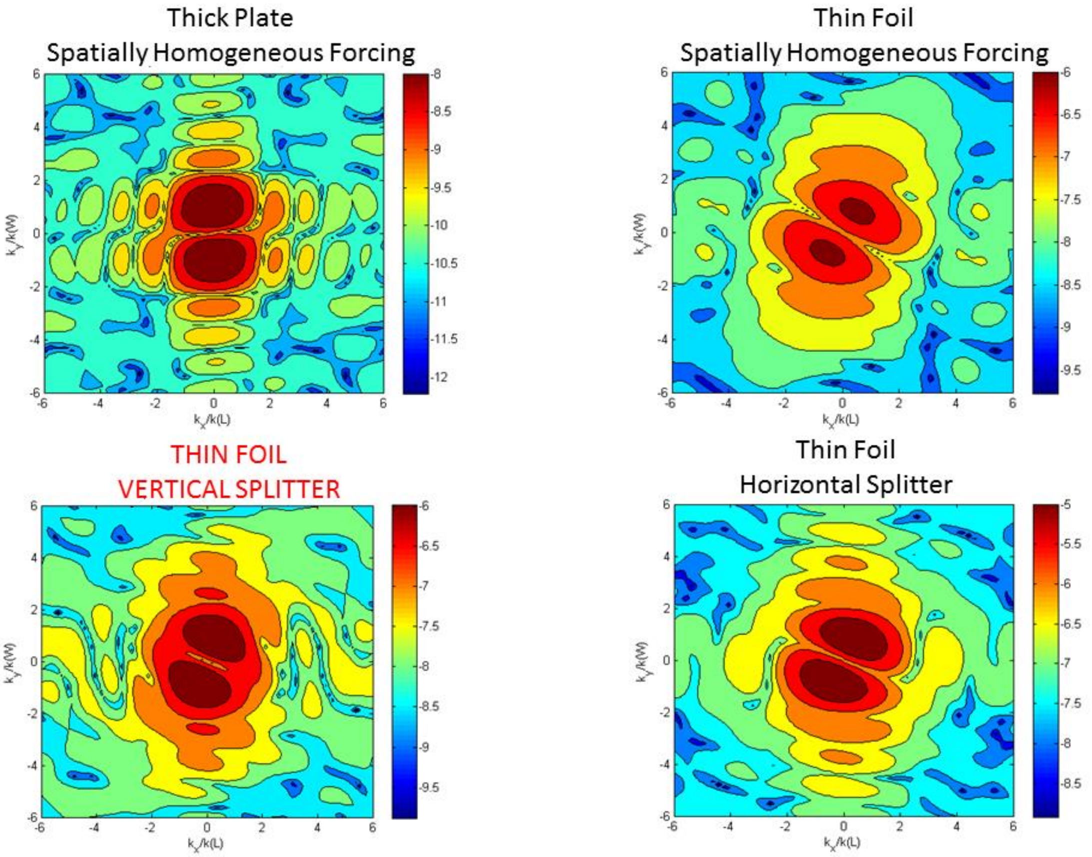

Thick Plate
Spatially Homogeneous Forcing

Thin Foil
Spatially Homogeneous Forcing

THIN FOIL
VERTICAL SPLITTER

Thin Foil
Horizontal Splitter

Figure A.3. Wavenumber transform for mode <1,2> excited by various methods. Color axis corresponds to $\log_{10}$ of the surface shape at the natural frequency divided by (m/s).

The shape functions for the non-fluid-loaded plate excited by a spatially homogeneous wall pressure field in Figures A.1-A.3 are similar to the theoretical shape function. This is anticipated because the mode shapes closely match the theoretical mode shapes. The fluid-loaded foil excited by spatially homogeneous forcing is similar to this but appears rotated slightly. This is because the mode shapes under these conditions are shifted slightly due to slightly non-uniform tension.

When non-homogeneous forcing does not induce a shift in the mode shape in the fluid-loaded foil, there is no significant change in the mode shape. This includes all cases for mode <1,1>, the vertical splitter for mode <2,1>, and the horizontal splitter for mode

<1,2>. For these cases, the wall pressure was spatially homogeneous in the direction where the mode shape has multiple lobes. As outlined in Chapter 5, these cases have no significant alteration of the mode shape, and as such, the shape function remains unchanged.

In Figure A.2, the horizontal splitter corresponds to a case where there was a significant change in the mode shape due to non-homogeneous forcing. In Figure A.3, the vertical splitter corresponds to a case where there was a significant change in the mode-shape due to non-homogeneous forcing. Both of these cases were examined in Chapter 5. For these cases, the shape functions becomes more circular, centered around $k_x=0$, $k_y=0$. While distinct lobes are noticeable, the peaks merge together somewhat. In other cases, the shape function had large valleys between the lobes, whereas in these two cases, when the mode shape becomes asymmetric, the valleys disappear somewhat.

BIBLIOGRAPHY

[1] W.K. Blake. *Mechanics of Flow-induced Sound and Vibration (two volumes)*. Academic Press Inc. New York., 1986.

[2] G.M. Corcos. Resolution of pressure in turbulence. *Journal of the Acoustical Society of America*, 35:192-199. 1963.

[3] G.M. Corcos. The resolution of turbulent pressures at the wall of the boundary layer. *Journal of Sound and Vibration*, 6:59-70. 1967.

[4] D.M. Chase. Modeling the wavevector-frequency spectra of turbulent boundary layer wall pressure. *Journal of Sound and Vibration*, 70:29-67. 1980.

[5] D.M. Chase. The character of the turbulent wall pressure spectra at subconvective wave numbers and a suggested comprehensive model. *Journal of Sound and Vibration*, 112:125-147. 1987.

[6] A.V. Smol'yakov and V.K. Tkachenko. Model of a field of pseudosonic turbulent wall pressures and experimental data. *Soviet Physics-Acoustics*, 37:627-631. 1992.

[7] H.H. Schloemer. Effects of Pressure Gradients on Turbulent-Boundary-Layer Wall-Pressure Fluctuations. *Journal of the Acoustical Society of America*. 42(1):93-113. 1967.

[8] F.R. Fricke. Pressure Fluctuations in Separated Flows. *Journal of Sound and Vibration*, 17(1):113-123. 1970.

[9] T.M. Farabee and M.J. Casarella. Effects of surface irregularity on turbulent boundary layer wall pressure fluctuations. *Journal of Vibration, Acoustics, Stress, and Reliability in Design*, 106:343-350. 1984.

[10] T.M. Farabee and M.J. Casarella. Measurements of fluctuating wall pressure for separated reattached boundary layer flows. *Journal of Vibration, Acoustics, Stress, and Reliability in Design*, 108:301-307. 1984.

[11] D.B. Stephens. *Sound Sources in a Low Speed Ducted Rotor.* Graduate Program in Aerospace and Mechanical Engineering, Notre Dame, IN. June 2008.

[12] D.B. Stephens and S.C. Morris. A method for quantifying the acoustic transfer function of a ducted rotor. *Journal of Sound and Vibration*, 313:97-112, 2008.

[13] D.B. Stephens, S.C. Morris, and W.K. Blake. Sound generation by a rotor ingesting a casing turbulent boundary layer. *14th AIAA/CEAS Aeroacoustics Conference*, 2008.

[14] Morris, S.C., Tomko, J. Analysis of sound measurements inside a finite length ducted rotor. ASME Noice Control and Engineering, Baltimore. April 19-21, 2010.

[15] E.A. Skelton and J.H. James. *Theoretical Acoustics of Underwater Structures*. Imperial College Press. London. 1997.

[16] A. Leissa. *Vibrations of Shells*. Ohio State University. Columbus. 1993.

[17] A. Leissa. *Vibrations of Plates*. Ohio State University. Columbus. 1993.

[18] P.M. Morse and K.U. Ingard. *Theoretical Acoustics*. Princeton University Press. Princeton, New Jersey. 1968.

[19] P.J.T. Filippi. *Vibrations and Acoustic Radiation of Thin Structures*. John Wiley & Sons, Inc. 2008.

[20] I. Dyer. Response of plates to a decaying and convecting random pressure field. *The journal of the acoustical society of America*, 31(7):922-928. 1959.

[21] L. Maestrello. Use of turbulent model to calculate the vibration and radiation responses of a panel, with practical suggestions for reducing sound level. *J. Sound Vib.*, 5(3):407-448. 1967.

[22] R.C. Leibowitz. Thin rectangular finite plates in heavy and light fluid media. *Journal of Sound and Vibration*, 40(4):441-495. 1974.

[23] H.G. Davies. *Acoustic Radiation from Fluid Loaded Rectangular Plates*. Massachusetts Institute of Technology, Camibrdge. 1969.

[24] F. Han, R.J. Bernhard, and L.G. Mongeau. Prediction of flow-induced structural vibration and sound radiation using energy flow analysis. *Journal of Sound and Vibration*, 227(4):685-709. 1999.

[25] F. Han, L.G. Mongeau, and R.J. Bernhard. A model for the vibro-acoustic response of plates excited by complex flows. *Journal of Sound and Vibration*, 246(5):901-926. 2001.

[26] J. Park, L. Mongeau, and T. Siegmund. An investigation of the flow-induced sound and vibration of viscoelastically supported rectangular plates: experiments and model verification. *Journal of Sound and Vibration*, 275:249-265. 2004.

[27] C. Maury, P. Gardonio, and S.J. Elliott. A wavenumber approach to modeling the response of a randomly excited panel, part 1: general theory. *Journal of Sound and Vibration*, 252(1):83-113. 2002.

[28] C. Maury, P. Gardonio, and S.J. Elliott. A wavenumber approach to modeling the response of a randomly excited panel, part 1: application to aircraft panels excited by a turbulent boundary layer. *Journal of Sound and Vibration*, 252(1):115-139. 2002.

[29] E. Ciappi, F. Magionesi, S. De Rosa, and F. Franco. Hydrodynamic and hydroelastic analyses of a plate excited by the turbulent boundary layer. *Journal of Fluids and Structures*, 25:321-342. 2009.

[30] P.J.T. Filippi, D. Habault, P.-O. Mattei, and C. Maury. The role of the resonance mode in the response of a fluid-loaded structure. *Journal of Sound and Vibration*, 239(4):639-663. 2001.

[31] O. Collery and J.L. Guyader. Solving the vibroacoustic equations of plates by minimization of error on a sample of observation points. *Journal of the Acoustical Society of America*, 127(3):1347-1356. 2010.

[32] D. Mazzoni. An efficient approximation for the vibro-acoustic response of a turbulent boundary layer excited panel. *Journal of Sound and Vibration*, 264:951-971. 2003.

[33] S. Finnveden, F. Birgersson, U. Ross, and T. Kremer. A model of wall pressure correlation for prediction of turbulence-induced vibration. *Journal of Fluids and Structures*, 20:1127-1143. 2005.

[34] A.D. Grant and J.B. Lawrie. Propagation of fluid-loaded structural waves along a duct with smoothly varying bending characteristics. *The Quarterly Journal of Mechanics and Applied Mathematics*, 53(2):299-321. 2000.

[35] W.R. Graham. A comparison of models for the wavenumber-frequency spectra of turbulent boundary layer pressures. *Journal of Sound and Vibration*, 206:541-565. 1997.

[36] F. Han, R.J. Bernhard, and L.G. Mongeau. Prediction of flow-induced structural vibration and sound radiation using energy flow analysis. *Journal of Sound and Vibration*, 227(4), 685-709. 1998.

[37] A.O. Borisyuk and A.V. Grinchenko. Vibration and noise generation by elastic elements excited by a turbulent flow. *Journal of Sound and Vibration*, 204:213-237. 1997.

[38] B.M. Efimtsov. Characteristics of the field of turbulent wall pressure fluctuations at large Reynolds numbers. *Soviet Physics – Acoustics*, 28(4):289-292. 1982.

[39] J.E. Ffowcs Williams. Boundary-layer pressures and the Corcos model: a model to incorporate low-wavenumber constraints. *Journal of Fluid Mechanics*, 125:9-25. 1982.

[40] N.C. Martin and P. Leehey. Low wavenumber wall pressure measurements using a rectangular membrane as a spatial filter. *Journal of Sound and Vibration*, 52:95-120. 1977.

[41] D.B. Hanson. Spectra of rotor noise caused by atmospheric turbulence. *Journal of the Acoustical Society of America*, 56(1):110-126. 1974.

[42] N. Moiseev, B. Lakshminarayana, and D.E. Thompson. Noise due to interaction of boundary-layer turbulence with a compressor rotor. *Journal of Aircraft*, 15(1):53-61. 1978.

[43] U.W. Ganz, P.D. Joppa, T.J. Patten, and D.F. Sharpf. Boeing 18-inch fan rig broadband noise test. *NASA CR-1998-208704*. 1998.

[44] S. Glegg and N. Walker. Fan noise from blades moving through boundary layer turbulence. *5th AIAA/CEAS Aeroacoustics Conferece, Bellevue (Greater Seattle), Washington, May 10-12, 1999*. 1999.

[45] P. Joseph and A. Parry. Rotor/wall boundary layer interaction broadband noise in turbofan engines". *7th AIAA/CEAS Aeroacoustics Conference, Masstricht, Netherlands, May 28-30,* 2001.

[46] R. Martinez. Broadband sources of structure-borne noise for propulsors in "haystacked" turbulence. *Computers & Structures*, 65(3):475-490. 1997.

[47] Atassi, H.M. and Logue, M.M. Fan broadband noise in anisotropic turbulence. *15th AIAA/CEAS Aeroacoustics Conference, Miami, Florida, USA, May 11-13, 2009*. 2008.

[48] M. Sevik. Sound radiation from a subsonic rotor subjected to turbulence. *NASA SP*, 304(11):493-511. 1974.

[49] A. Pierce, Acoustics: An Introduction to its Physical Principles and Applications, McGraw-Hill, New York, 1981.

[50] D.B. Stephens and S.C. Morris. Sound generation by a rotor interacting with a casing turbulent boundary layer. *AIAA Journal*, 47(11):2698-2708. 2009.

[51] Ivanyuta, E.I. and Finkelsthein, R.M. On a Variational Method for the Solution of Certain Dynamic Problems of the Theory of Shells. Prikl. Mekh., Vol. 9, No. 1, 1963. (in Ukranian)